Physicochemical Hydrodynamics and Machine Learning Characterization of Isothermal Nucleic Acid Amplification Nucleation Site Analysis

Coleman D. Martin

A dissertation
submitted in partial fulfillment of the
requirements for the degree of

Doctor of Philosophy

University of Washington

2025

Reading Committee:
Jonathan D. Posner, Chair

David A.C. Beck

Cole A. DeForest

Program Authorized to Offer Degree

Chemical Engineering

University of Washington

Abstract

Physicochemical Hydrodynamics and Machine Learning Characterization of Isothermal Nucleic Acid Amplification Nucleation Site Analysis

Coleman D. Martin

Chair of Supervisory Committee:
Jonathan D. Posner
Department of Chemical Engineering

Nucleic acid diagnostics have advanced since PCR's first use in sickle cell and HIV diagnosis in the 1980s. PCR remains the gold standard for detecting SARS-CoV-2 and monitoring HIV viral load but is limited by resource-intensive requirements, making it impractical for low-resource or home settings. My research aims to adapt PCR's strengths using isothermal nucleic acid amplification for rapid, low-cost diagnostics to support global health.

I first present a novel assay combining RPA-based amplification with lateral flow detection, offering PCR-level sensitivity with LFA-like ease. It meets WHO SARS-CoV-2 detection standards, demonstrates high specificity, variant resilience, and uses a simple lysis method suitable for minimal devices.

For HIV viral load monitoring, I developed a buffer-modified recombinase polymerase amplification assay on microfluidic chips using amplification nucleation site analysis (ANSA), where nucleation site counts correlate with nucleic acid input, enabling precise, mobile phone-compatible measurements.

Finally, I describe a machine learning approach using a ResNet-18 model to analyze temporal ANSA data and predict DNA concentrations. Two models classify DNA by clinical groups or log-fold changes. This work supports robust, POC-suitable HIV diagnostics and establishes a platform for broader quantitative nucleic acid testing across global health settings.

Acknowledgements

No journey worth taking is walked alone. This one was shaped by the steady presence of a community that carried me through its many highs and lows.

To those who shared in the unfiltered conversations, the quiet frustrations, and the moments of discovery, thank you. Your companionship turned challenge into growth and made the journey feel less solitary.

To the mentors who pushed me to think more deeply, to question more boldly, and to keep reaching, thank you for shaping not only my work, but the way I see the world.

To the friends who offered laughter, distraction, and perspective, thank you for reminding me there is life beyond the lab.

And to my parents and brother whose love, patience, and belief have been my foundation, your quiet strength made all this possible.

Thank you, all of you, for taking this journey with me.

Table of Contents

List of Figures

List of Tables

List of Abbreviations

AIDS	Acquired Immunodeficiency Syndrome
ANSA	Amplification Nucleation Site Analysis
ART	Antiretroviral Therapy
CDC	Centers for Disease and Control and Prevention
ddPCR	Digital Droplet Polymerase Chain Reaction
DNA	Deoxyribonucleic Acid
dsDNA	Double Stranded Deoxyribonucleic Acid
EACS	European AIDS Clinical Society
ELISA	Enzyme-Linked Immunosorbent Assay
Exo	Exonuclease
HIV	Human Immunodeficiency Virus
LAMP	Loop-mediated isothermal amplification
LoD	Limit of Detection
NA	Nucleic Acid(s)
NAAT	Nucleic Acid Amplification Test
NTC	Non-Template Control
PCR	Polymerase Chain Reaction
PEG	Polyethylene Glycol
PLHIV	People Living with HIV
POC	Point-of-Care
PVP	Polyvinylpyrrolidone
qPCR	Quantitative Polymerase Chain Reaction
RDT	Rapid Diagnostic Test
RNA	Ribonucleic Acid
RPA	Recombinase Polymerase Amplification
RT-PCR	Reverse Transcriptase Polymerase Chain Reaction
RT-RPA	Reverse Transcriptase Recombinase Polymerase Amplification
ssDNA	Single Stranded Deoxyribonucleic Acid
TPP	Target Product Profile
WHO	World Health Organization

1 Infectious Diseases Require Diagnostics

1.1 In Vitro Diagnostics for Infectious Diseases

In vitro diagnostics for disease are conducted on blood, urine, saliva, or tissue samples collected from the human body. The term “in vitro” translates to “in glass”, denoting that these tests are performed in test tubes outside of the body compared to “in vivo” tests which are conducted within the body itself. In vitro diagnostics are used for the initial diagnosis of disease, to monitor disease progression and to monitor health to help cure, treat, or prevent diseases. These tests can be conducted in well-resourced laboratories using complex reactions for precise quantification, at the point of care (POC) in a doctor’s or other medical practitioners’ office, and even at home. These diagnostics play a crucial role in patient care, enabling effective diagnosis and treatment planning.

1.1.1 Immunoassays

Immunoassays are biochemical tests that measure the presence or concentration of a specific molecule, the analyte, in a solution through the use of an antibody or an antigen. The analyte can be a variety of molecules, as long as the appropriate antibody, antigen, or aptamers have been developed to bind to the analyte. Immunoassays are frequently used in clinical diagnostics, drug discovery, drug monitoring, and food testing. Immunoassays produce a measurable signal in response to the binding of an antibody to its antigen.

ELISA

Enzyme-Linked Immunosorbent Assay (ELISA) is a fundamental tool for in vitro diagnostics and widely used for the initial screening, treatment monitoring, and prognosis evaluation of various diseases.[1] It has been a gold standard testing mechanism for invitro diagnostics for the last five decades, contributing to the analysis of biomarkers and important analytes in healthcare and diversified analytical settings.[2] ELISA offers significant advantages due to its simplicity, utility, low cost, high sensitivity, and specificity. However, traditional ELISA technology can be tedious requiring multiple washing steps, lacks simultaneous target detection capabilities as it reads out in optical density, and is not easily implemented in point-of-care (POC) settings.[1] As a common first line assay ELISA assays have been produced for multiple viruses: Lassa fever, Dengue fever, Ebola hemorrhagic fever, Zika fever, West Nile fever, Measles, SARS, and Influenza.[3]

In an ELISA, the antibody or antigen is nonspecifically adsorbed or bounded to the surface of a solid phase (microtiter well, magnetic particle, or plastic bead). This attachment allows the separation of bound and free-labeled reactants during washing phases. Typically, an aliquot of sample or calibrator containing the

antigen (Ag) to be detected is added to the solid phase antibody (Ab) and allowed to bind. Then an enzyme-labeled antibody is added and forms a "sandwich complex" of solid-phase Ab-Ag-Ab enzyme, this is demonstrated in Figure 1. A subsequent washing step removes unbound antibody and enzyme substrate is added for detection. The amount of product generated is proportional to the quantity of antigen in the sample.[4]

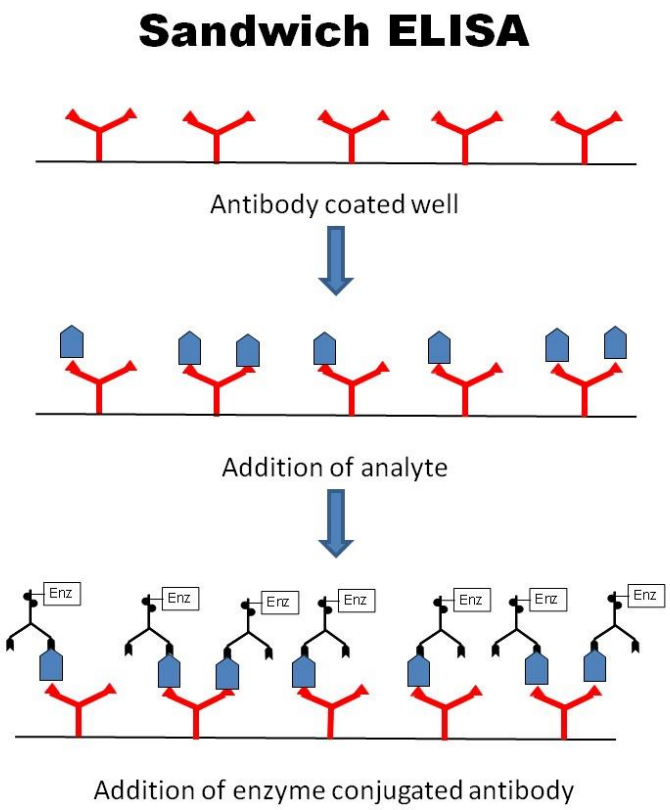

Figure 1. Diagram of a sandwich ELISA.[5]

While ELISA assays are common first line assays and can be produced once an antibody or antigen has been produced, they have notable limitations. ELISA assays are also hindered by the latent period where viral production is high but antibody production lags behind, in the first generation of HIV tests the lag time was 35-45 days,[6] newer assays have cut this lag time significantly to 10-15 days post infection.[7] Further, the assay is limited to the binding affinity and specificity of the antibody or antigen as they are required to bind structural motifs of the target. For some target viruses like Dengue and Zika, the structural motifs are similar thus ELSIA assays lose specificity. In the case of Zika and Dengue, the ELISA assays are cross reactive as both viruses are simultaneously detected.[8] ELISA assays also have long rung times due to the

process of requiring multiple incubation and washing steps, these assay times are often longer than that of run times of nucleic acid amplification tests all while having a worse sensitivity early in infection.[3]

Rapid Antigen

The SARS-CoV-2 pandemic made rapid antigen tests (Figure 2) a household product. Previously likened to pregnancy tests, these rapid have a broad scope of utility. They can analyze a variety of testing media including urine, saliva, sweat, serum, plasma, and whole blood, supporting their application across a diverse range of fields.[9–15] Not only are they well documented in human and veterinary medicine, but their use extends to quality control and product safety in food production, as well as environmental health and safety. In these domains, rapid tests serve the crucial function of screening for animal diseases, pathogens, chemicals, toxins, and water pollutants, showcasing their versatility and wide-ranging impact.[16]

Figure 2. Rapid lateral flow diagnostic for SARS-CoV-2. Image from Shutterstock

The appeal of rapid lateral flow antigen tests lies in their fast sample-to-answer time and cost efficiency, attributes that stem from their simple construction, which often includes an injection-molded case and nitrocellulose pads. The testing mechanism for LFA's involves binding and immobilizing the analyte ligand (virus) on a test line, which is then conjugated and visualized with gold nanoparticles. The detection mechanism has similar mechanics to that of the sandwich assay see in Figure 1 where instead of an enzyme linked antibody the antibody typically is labeled with a colloidal gold nanoparticle for visualization. This process does not amplify the analyte unlike nucleic acid-based tests and relies on high concentrations of the ligand to be present and bound to the test line for visual readout. Sensitivity of these assays can be improved using fluorescent nanoparticles, quantum dots, electrophoretic focusing, reporter reactions, and photodiode/CCD imaging.[17–21] This characteristic makes rapid tests particularly suitable for use in clinical

settings, at home, or in the field, where quick and straightforward diagnostic procedures are valued with the tradeoff in reduced sensitivity when compared to nucleic acid amplification tests or ELISA assays.

The procedure for utilizing rapid lateral flow antigen tests is straightforward and comprises three main steps: collection, preparation, and detection. Collection can either be self-administered or require trained staff, depending on the context and specific test design. During the preparation stage, the specimen (which could be blood, saliva, sputum, or urine) is suspended in a running buffer. This step is critical for preserving the analytes, diluting inhibitors, and reducing viscosity, thereby preparing the sample for analysis. Finally, detection is carried out through the visual identification of test lines, allowing for an immediate readout of the test result. This simplicity and efficiency underline the significant role rapid lateral flow antigen tests play in current diagnostic practices, offering a practical solution for timely disease management and control.

1.1.2 NAAT

Nucleic Acid Amplification Testing (NAAT) is considered the gold standard for viral load testing and other presence/absence testing due to its high sensitivity and specificity.[22] This method enables the amplification of low levels of pathogenic DNA or RNA oligonucleotides to detectable levels, providing an essential tool for diagnosing and monitoring viral infections. NAATs are typically conducted in central laboratories, which require aseptic conditions with controlled temperature and humidity, trained staff, constant electricity, cold chain storage, and sensitive instrumentation. These stringent requirements, while necessary for the accuracy and reliability of NAATs, contribute to the challenges of widespread testing. The centralized nature of this testing approach often results in sampling delays and extended times for the return of results.

PCR and quantitative PCR

Polymerase Chain Reaction (PCR) is a widely used method for the amplification of DNA. PCR is fundamental to many procedures used in genetic testing, research, and diagnostics. PCR has become an indispensable technique used in medical laboratory research for a broad variety of applications including biomedical research and forensic science due to its single DNA copy sensitivity and single nucleotide specificity. The process involves repeated cycles of heating and cooling to permit different temperature-dependent reactions of DNA denaturation, primer hybridization, and enzymatic DNA extension to occur.

The PCR mechanism (Figure 3) utilizes two primers and a polymerase. During the first phase of the reaction, in a PCR cycle, the reaction temperature is raised to 95 °C to denature double-stranded DNA (dsDNA) to single-stranded DNA (ssDNA). The temperature is then lowered to 55 °C to anneal sequence

specific primers creating a small section of dsDNA, then the temperature is raised to 75 °C in which the polymerase enzyme binds to the 5' end of the primer-template duplex and extend towards the 3' end of the DNA, creating a complimentary copy. After the extension, the cycle is repeated, and the resulting dsDNA is denatured, providing additional templates for further amplification. Following this mechanism, PCR doubles the amount of DNA in each cycle. This process is repeated for a total of 45+ cycles. The extreme sensitivity (often less than 10 cps/rxn[23–25]) and specificity make PCR the gold-standard for amplification. However, the need for precise temperature control necessitates the use of expensive thermocyclers and a typical PCR assay takes hours to complete.

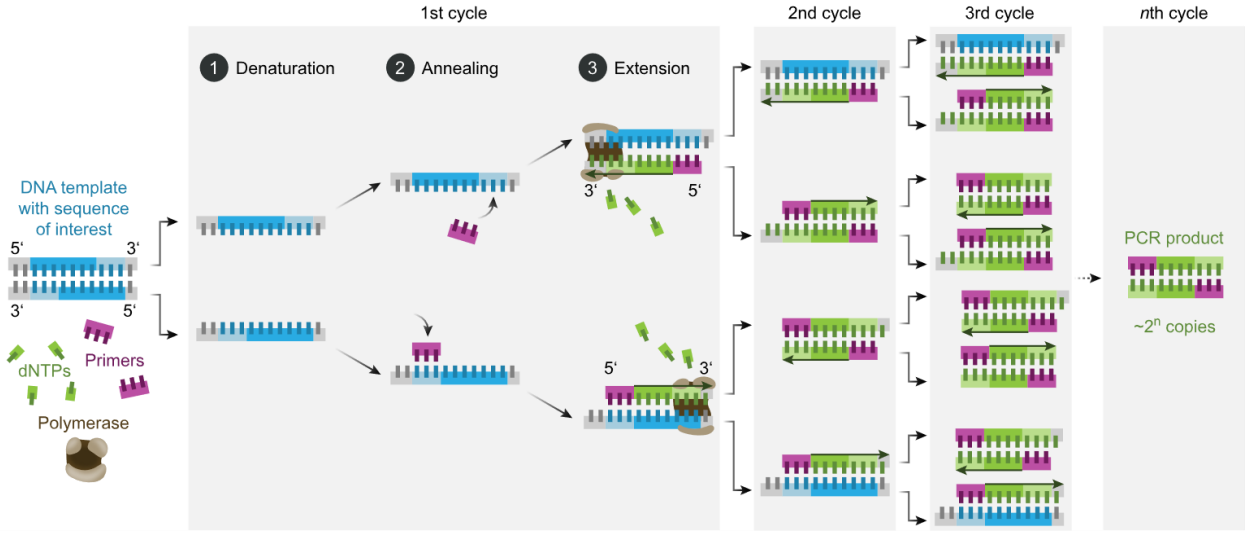

Figure 3. PCR Amplification mechanism.[26]

Quantitative PCR (qPCR), also known as Real-Time PCR, is a modified mechanism of PCR that utilizes an enzymatically cleaved homology prove that not only detects the presence of target nucleic acids, but also provides quantification by monitoring the rate of generation of the amplified product measured at each PCR cycle.[27] In qPCR, real-time fluorescence monitoring of the reaction is used to calculate a cycle-threshold (Ct) value, defined as the number of thermal cycles required for the fluorescent signal to reach a specified threshold. This is compared to calibration curve that is created with known target nucleic acid concentrations to establish the concentration of the "unknown" sample. qPCR is crucial tool in monitoring diseases in which pathogen load can information clinical treatment (e.g., HIV viral load monitoring, SARS-CoV-2, Hepatitis B, Hepatitis C).[27–31]

For the most precise absolute quantification of nucleic acids, Digital droplet PCR (ddPCR) is used. ddPCR utilizes thousands of discrete PCR reactions in microfluidic micro-drops and Poisson statistics to provide absolute sample quantification.[32,33] ddPCR typically has lower dynamic range than qPCR (five orders of magnitude for commercial systems such as the BioRad QX200) due to signal saturation, requires separate droplet generation prior to amplification cycling, and can suffer from false positives resulting from inappropriate thresholding.[34] Both qPCR and ddPCR are traditionally restricted to well-instrumented laboratories or hospitals due to cold chain dependent reagents, delicate instrumentation, reliable electrical power, proficient laboratory staff, and appropriate infrastructure to host required equipment.

NAAT Workflow

The procedure for NAAT involves several steps: collection, preparation, amplification, and detection of nucleic acids. Collection can either be self-administered or require trained healthcare personnel, depending on the type of sample being collected (e.g., blood, saliva, sputum, urine). The preparation process involves the lysis of pathogens and inactivating confounding factors. Lysis frees the target genomic material from the pathogen making it available to be amplified. Simultaneously, nucleases found in the sample must be inactivated to inhibit target degradation. Freeing target nucleotides from their viral envelopes or cell walls/membranes often utilizes various methods such as chemical, mechanical, electrical, thermal, or enzymatic techniques.[35–43] Centralized laboratories typically employ solid-phase extraction lysis methods, utilizing chaotropic salts, surfactants and sequential columns or filters to bind and release nucleic acids. These salts not only disrupt membranes but also denature nuclease enzymes that degrade free nucleic acids and hinder assay sensitivity.[38,39]

Following preparation, purified nucleic acids undergo amplification to increase their concentration to detectable levels. PCR is a widely used amplification method, known for its high sensitivity and specificity. PCR involves cyclically heating and cooling the DNA to denature it, anneal primers, and extend the primers to create double-stranded DNA, thereby exponentially amplifying the target nucleic acids.[44–46] Quantitative PCR (qPCR) adds the capability to quantify the amount of DNA by running a standard curve of known concentration alongside the PCR reaction, allowing for precise measurement of viral load. PCR and qPCR is detailed in the previous section.

The detection of amplified products can be conducted through various means, including fluorescent intercalating dyes, sequence-specific probes, color change indicators, UV-VIS, or electrochemical measurements.[47–49] These methods can provide real-time or endpoint analysis of the sample. Modern commercial high-throughput systems like the Roche COBAS and Abbot Alinity-m (Figure 4) have automated the sample preparation, amplification, and detection steps, significantly reducing the time and labor required compared to manual procedures. Such systems can process 500-1000 samples every 8 hours,

offering a "sample to answer" capability. However, the automation and scale of these systems require substantial upfront investments, typically around $150,000, and significant laboratory infrastructure to support the necessary environmental controls.[50]

Figure 4. Commercial high throughput viral load testing platforms.

Isothermal NAATs

Overview of Isothermal Methods

While Polymerase Chain Reaction (PCR) has long been the “gold standard” for DNA amplification, its reliance on thermocycling necessitates specialized equipment, limiting it to well-funded central labs, and limits its integration into compact devices suitable for the point of care. Isothermal NAATs have been developed to leverage the sensitivity and specificity of PCR while improving the assay time, resistance to typical inhibitors, and assay cost. As such, isothermals have begun to play a pivotal role in molecular diagnostics, enabling the detection of minute quantities of target molecules. Isothermals have emerged as promising alternatives, for PCR particularly for point-of-care diagnostics. These non-PCR techniques mimic in vivo amplification processes, offering high sensitivity, selectivity, and compatibility with high-throughput workflows. As a result, various platforms leveraging isothermal methods have been developed and commercialized. Multiple isothermal methods have been published: Nucleic Acid Sequence-Based Amplification (NASBA), Reverse Transcriptase-Free Exponential Amplification Reaction (RTF-EXPAR), Multiple Displacement Amplification (MDA), Helicase-Dependent Amplification (HDA), Strand Displacement Amplification (SDA), Rolling-Circle Amplification (RCA), Loop-Mediated Isothermal Amplification (LAMP), and Recombinase polymerase amplification (RPA). Figure 5 outlines key features of NASBA, LAMPA, SDA, RCA, and RPA compared to PCR. LAMP and RPA are of particular interest in this work and are detailed in subsequent sections.

Property	PCR	NASBA	LAMP	SDA	RCA	RPA
Nr of required enzymes	1	3	1	2	2	2
Primer design (Nr of primers)	Simple 2	Simple 2	Complex 4 or 6	Complex 2 or 4	Simple 2	Simple 2
Temperature	Thermal Cycling (95, 50—65, 72) oC	Isothermal ~41°C	Isothermal 60—65°C	Isothermal 37°C	Isothermal 30°C	Isothermal 37—42°C
Reaction time	2–3 h	1.5—2 h	<1 h	2 h	1.5 h	20–40 min
Target	DNA (RNA)	ssRNA (DNA)	dsDNA (RNA)	ssDNA (RNA)	Circular DNA (RNA)	dsDNA
Amplicon	dsDNA	RNA, DNA	Concatenated DNA	dsDNA	Circular DNA	Long dsDNA
Sensitivity	1–10 copies	Single copy	Single copy	10 copies	10 copies	Single copy
Detection	Gel electrophoresis, Real-time and ELISA	Gel electrophoresis, Real-time and ELISA, ECL	Gel electrophoresis, Real-time and turbidity	Gel electrophoresis, Real-time	Gel electrophoresis, Real-time	Gel electrophoresis, Real-time and ELISA
Tolerance to cotaminants	Low	Medium	High	Low	Low	High
Initial template denaturation	Yes	No	No	Yes	No	No
Template processivity	Heat	Rnase H	Strand-displacement property of *Bst* polymerase	Restriction enzymes Heat	Strand-displacement property of ϕ29 DNA polymerase	Recombinase
Advantages	Accurate and robust quantification	Design to detect RNA targets	10^9-fold amplification in less than 1 h	Suitable for miRNA profiling	Low amplification temperature (~37°C) ssDNA products are compatible with other isothermal techniques	Low amplification temperature (~37°C)
	Simplicity of the procedure	10^7-fold amplification in 2 h	Tolerance to inhibitory substances	10^5-fold amplification in 2 h	Produce long DNA fragments	Selective
	Well-stablished method	Kits commercially available	Highly specific	Commercially available platform	Specific for circular targets	Fastest amplification system (20–40 min)
	Availability of wide number commercial kits	Power saving (41°C)	Allows naked-eye detection	Power saving (37–50°C)	—	Tolerance to high volume reduction
	—	—	Great variety of commercial kits	—	—	Tolerance to inhibitory substances
Disadvantages	High equipment cost	Not ideal for DNA targets	Not suitable for small targets	Initial denaturation required	Only works with circular templates	Stringent reaction condition
	Intolerant to many substances	Less efficient for long RNA targets	False positive phenomenon often occurs	Requires sample preparation	RNA amplification is complex and often problematic	Amplification products cannot be readily detected by electrophoresis
	Error prone polymerase	Prone to false positives	Complex primer design	Limitation to small targets	Linear targets require ligation reactions	Commercial kits are expensive
	Less efficient than most of the isothermal methods	Need to optimize 3 different enzymes	—	Prone to unspecific amplification	Linear amplification profile	—
	Long amplification time	—	—	—	—	—

Abbreviations: PCR—Polymerase Chain Reaction; NASBA—Nucleic Acid Sequence-based Amplification; LAMP—Loop-mediated Isothermal Amplification; SDA—Strand Displacement Amplification; RPA—Recombinase Polymerase Amplification; RCA—Rolling Circle Amplification.

Figure 5. Overview of common isothermal DNA mechanisms.[51]

LAMP

Loop-Mediated Isothermal Amplification (LAMP) is a powerful technique for DNA amplification that operates under constant temperature conditions of 60–65°C. To achieve strand displacement and amplification, LAMP uses 4 to 6 primers and Bst, a strand displacing polymerase. The primers recognize 6 to 8 distinct regions on the target DNA. The fifth and sixth primers form “loop” structures during the

reaction. The primers are B1c-B3c (back complement 1-3), F1c-F3c (forward complement 1-3), LB (loop back), LF (loop forward) in Figure 6. These loops greatly increase amplification speed and facilitate subsequent rounds of amplification. Primer design is often aided by software tools like the NEB LAMP Primer Design Tool due to the complexity of having multiple primers. The amplification products are often very long and vary in length as the loop structures consist of numerous repeats of the short target sequence connected by single-stranded loop regions. including fluorescent dyes, turbidity measurements, and halochromic visual indicators.[49,52,53] Colorimetric detection, turbidity, lateral flow, and halochromic measurements are considered an end point detection while fluorescent detection mechanisms allow for Realtime analysis. Despite its broad applicability to pathogens like HIV-1, HPV-16, SARS-CoV-2, and Hepatitis B and C, LAMP faces challenges such as difficulty in multiplexing and the potential for nonspecific amplification due to the extensive primer design.[54–57]

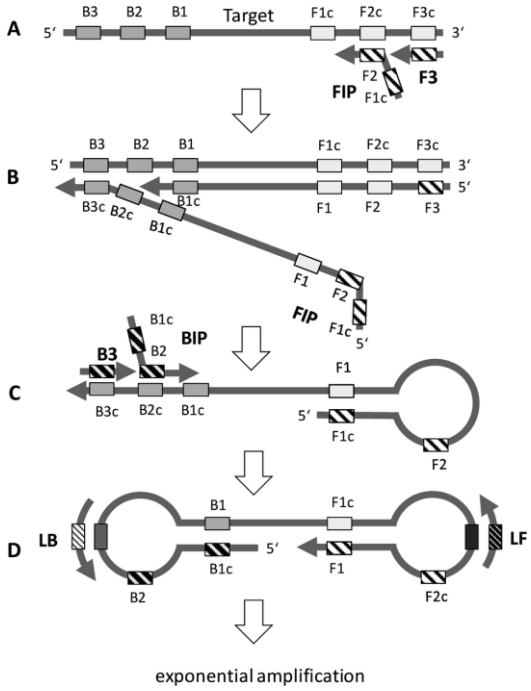

Figure 6. LAMP mechanism.[58]

RPA

RPA is an ideally suited isothermal amplification technique for point-of-care nucleic acid amplification tests (POC NAATs) due to its sensitivity (fewer than 10 copies per reaction), specificity, rapid assay time (less than 15 minutes), low incubation temperature requirement (approximately 40°C), inhibitor tolerance, and stability of its lyophilized reagents at room temperature.[59–61]. While RPA was under patent during part of this work and expired in early 2024, alternatives like Recombinase Aided Amplification (RAA) were

available on the market during the patent protection. Now that RPA is officially off patent we have seen an increase in vendors, such as ThermoFisher, selling RPA or RAA kits. RPA utilizes an internally quenched DNA hybridization probe, that when bound and cleaved, allows for real-time, sequence-specific fluorescence amplicon detection. Alternatively, endpoint detection can be carried out via gel electrophoresis or lateral flow analysis. For amplification, RPA utilizes long primer oligonucleotides and three core enzymes: recombinase, single stranded binding proteins, and a strand displacing polymerase. The recombinase enzymes pair to oligonucleotide primers to facilitate strand displacement and D-loop formation at homologous sequences in duplexed DNA. The D-loop is further stabilized by Single-Stranded DNA-Binding Protein (SSB) preventing primer displacement. Then, Bsu, the stand displacing polymerase, initiates DNA synthesis where the primer binds to the target DNA.

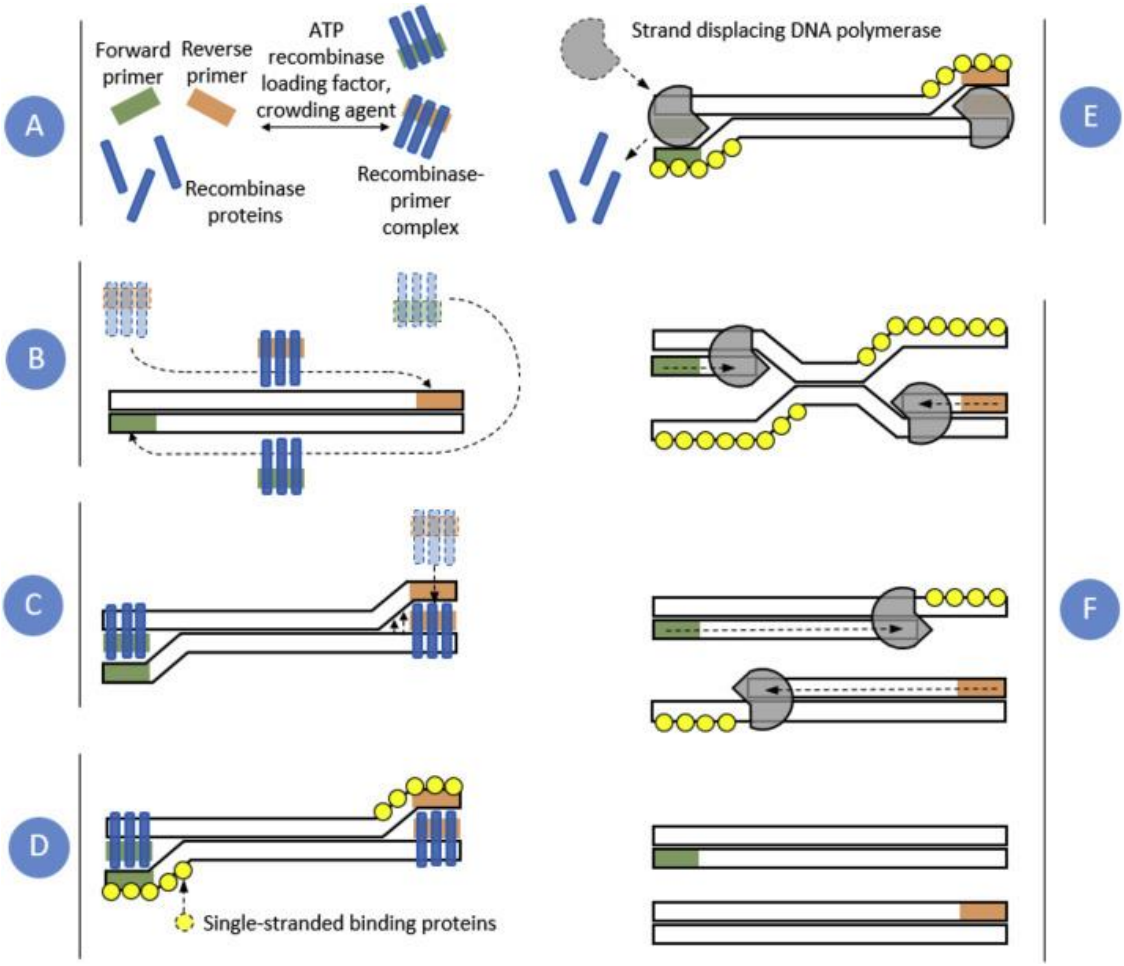

Figure 7. Recombinase polymerase amplification process.[62]

Quantitative Isothermal Nucleic Acid Amplification Tests

In an effort to reduce the barriers of qPCR testing, isothermal DNA amplification assays have emerged as replacement options to the traditional PCR assay. These assays have many perks and have been optimized for POC use with rapid run times <30 minutes, minimal heating requirements, and robustness to expected inhibitors. Yet these assays struggle with consistent quantification limiting the potential clinical utility to semiquantitative or order of magnitude approximation.[63] The hallmark thermal cycling parameter of PCR provides selective control of DNA amplification, only allowing the denaturation, annealing, and extension steps to happen once in a given cycle. Thus, as shown in Figure 3, DNA concentration is doubled every cycle, providing PCR with a solid base for quantification in real time when a known concentration control is run simultaneously.

Comparatively, isothermal assays utilize chemical energy, modified target templates, and simultaneous annealing and extension resulting in stochastic amplification efficiency. Efforts have been made to quantify LAMP and RPA reactions using time to threshold but have been only able to determine order of magnitude of viral load as time to threshold metrics can vary by up to a minute in subsequent reactions.[64,65] Changes in target sequence due to differing target subtypes and small reaction permutations can also drive changes in the reaction kinetics of these systems. [66–71]

Published assays using LAMP and other isothermals in a microwell chips and poison distribution statistics much like digital droplet PCR have shown progress and the ability for absolute quantification of nucleic acids.[72–76] These methods meet or exceed the required dynamic range and quantitative precision for clinical applications but struggle with POC applications such as genetic diversity, requiring specialized chips, emulsion generators, long filling times, technologically advanced imaging for quantification, and multiple fluid injections of immersible oil to: make, seal, and heat microspheres thus limiting their application in a POC setting. As shown in **Figure 8**. "Slip Chip" design.[77] less intensive chip designs coined “SlipChips” have also be published although these chips exhibit a smaller dynamic range.[77,78]

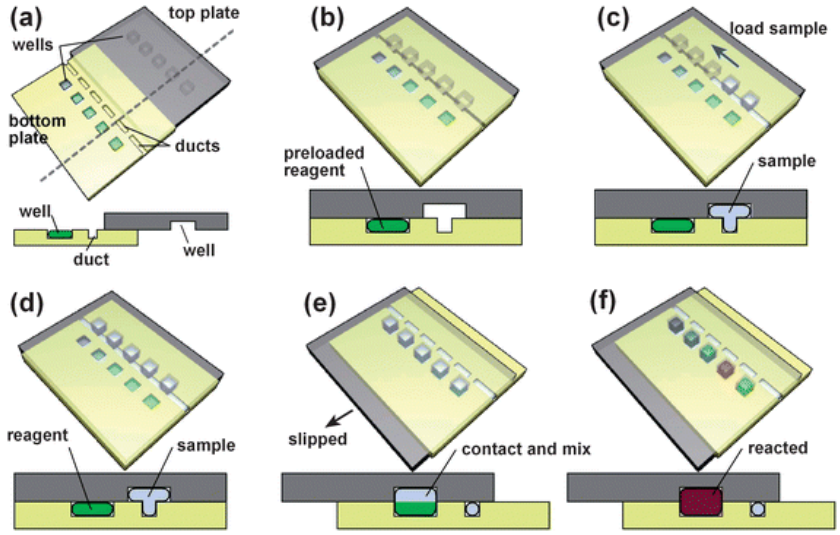

Figure 8. "Slip Chip" design.[77]

To circumvent the issues with microwell systems, hydrogel and membrane based support matrices have also been published. Hydrogels have been demonstrated to be a suitable support matrix for quantitative LAMP detection of SARS-CoV-2[79] and coliphages[80] in water treatment surveillance. Free form membrane based assays have also been published with the intent of reducing complexity and to automate sample loading are able to circumvent these issues by constraining the reaction mixture to membranes. This is a new and growing area of research with recent publications for the quantification of E.coli,[81] MS2 phage,[82] methicillin-resistant Staphylococcus aureus[83], Dengue[84], and HIV[66]. This has been an area of the Posner Research Group specialty and a growing area of interest.

1.2 COVID-19 Pandemic

Since its declaration as a pandemic in March 2020, COVID-19 has had major and lasting impacts on global health and economies, with over 770 million reported cases and 6.9 million deaths. This period has also been marked by a technical revolution in testing supported by initiatives like Rapid Acceleration of Diagnostics (RADX), although these advancements have predominantly benefited high-income countries (Figure 9). This disparity underscores the need for a more equitable distribution of healthcare innovations to manage and mitigate the spread of the virus effectively.

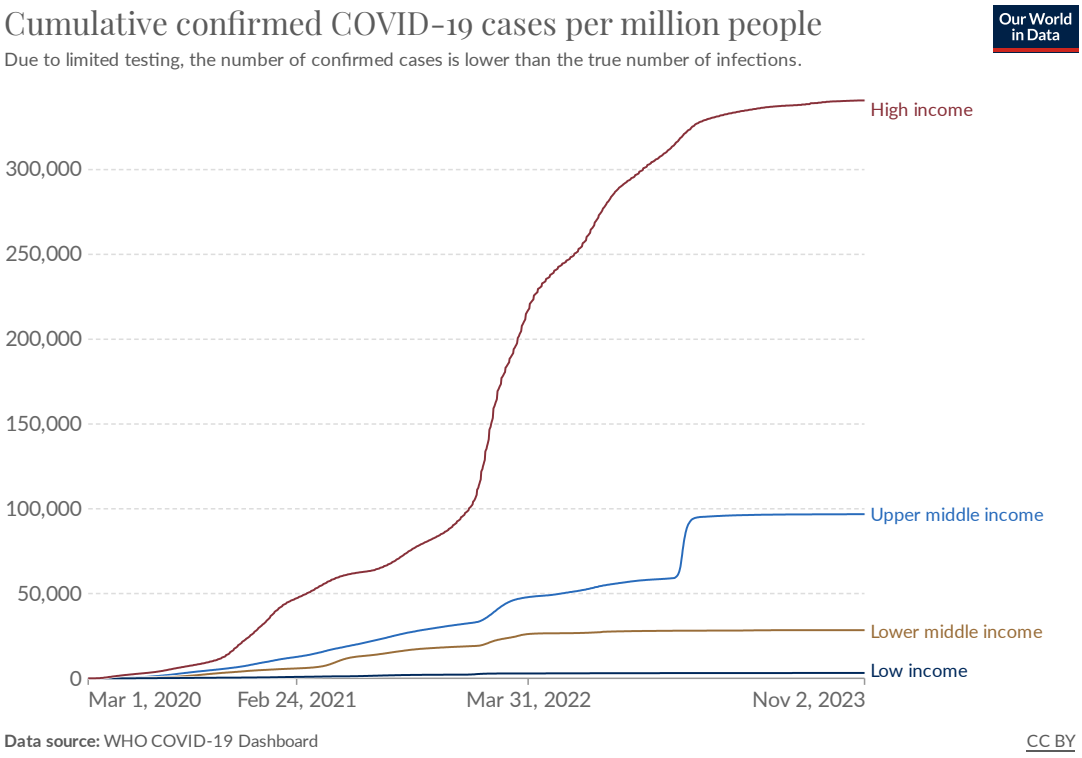

Figure 9. Cumulative confirmed cases of COVID-19. While a pandemic testing was concentrated in high income countries.

SARS-CoV-2, the virus responsible for COVID-19, is transmitted primarily through airborne respiratory droplets. While the potential for fomite-based spread exists, it is significantly lower than that of direct respiratory droplet transmission. SARS-CoV-2 is an enveloped, positive-sense single-stranded RNA virus, an approximate 29.9 kilobases genome that encodes 29 proteins. These include 16 nonstructural proteins involved in viral replication, four structural proteins that form the virus particle, and nine accessory proteins that modulate the host cell environment. The virus notably binds to the ACE2 receptor on host cells, facilitating entry and infection.

Viral shedding and transmission dynamics are critical to understanding and controlling the spread of SARS-CoV-2. Viral shedding can precede the onset of symptoms, often starting two days before. The highest viral titers are observed in the earliest phases of infection, typically 1-2 days before symptom onset and during the first 4-6 days of illness in patients without immunosuppression, with the illness duration ranging from 7 to 14 days. Furthermore, SARS-CoV-2 has demonstrated a high mutation potential, leading to the emergence of significant variants of concern, such as Delta and Omicron variants. These variants and the dynamic nature of the primary strain underline the complexity of managing the pandemic and the continuous need for vigilance and adaptation in public health responses.

1.3 Current Diagnostics Tests for SARS-CoV-2

1.3.1 PCR Gold Standard Testing for SARS-CoV-2

Reverse transcription PCR (RT-PCR) is the gold standard for SARS-CoV-2 molecular testing due to its high sensitivity and specificity, which is crucial for accurate detection during the early phase of infection when viral titers are low.[85] Scaled RT-PCR testing is primarily limited to central laboratories due to the need for specialized equipment for nucleic acid extraction, assay preparation, thermocycling, and target detection. These high-resource requirements result in delays from sampling to answer which delays clinical interventions that can prevent disease progression or reduce community transmission.[86]

1.3.2 Rapid Lateral Flow

Rapid lateral flow testing (rLFA) is the most widely used SARS-CoV-2 testing mechanism because of its low cost, ease of use, speed, and over-the-counter availability for use at home.[87] rLFA testing is was also allows for easy scaling due to low cost design and manufacturing which was highlighted in the distribution of free rapid COVID-19 antigen tests that started January 15, 2022. These tests became common due to their stability, rapid assay time (<15 minutes), limited user steps (collect, dilute, drop, interpret), and ease of visual interpretation. Despite their high stability and ease of use, one notable drawback is their poor sensitivity. Peer reviewed studies have shown that these tests have a 50% (95% CI, 45%-55%) accuracy compared to PCR during the infectious period.[88] This poor sensitivity has led the Centers for Disease Control and Prevention (CDC) to recommend serial testing over two days to confirm a negative test result for COVID-19 rule out diagnosis.[89]

Rapid lateral flow assay (LFA) antigen LFAs have poorer clinical accuracy compared to nucleic acid-based tests and have poorer limits of detection, so there are inherent risks that early infection may not be detected when low viral loads are typically present.[88,90–93]

1.3.3 Point of Care NAAT

Commercial point-of-care (POC) RT-PCR based diagnostics (Abbott ID Now, Cepheid GeneXpert Xpress, Roche cobas Liat, etc.) have been developed and received US FDA emergency use authorization to increase the accessibility of molecular tests with high clinical diagnostic accuracy. These cartridge-based platforms generally have an assay time greater than 30 minutes[94,95] and use desktop readers that automate fluidic handling, amplification, detection, and assay result interpretation. With the goal of increasing accessibility to NAAT testing, government initiatives to accelerate product development (e.g., NIH RADx program) led

to several single-use disposable and lower cost NAATs that were specifically targeted for community-based use (physician's office) or home/self-testing (e.g., Lucira CheckIt, Cue COVID-19, Aptitude Metrix, etc.) (Figure 10).[96–99] These commercially available tests use fluorescence or electrochemical detection and require onboard electronics to sense, analyze, and report test results. Early in the pandemic these tests had high utility in replacing PCR tests for airline travel and isolation bubbles.[100,101] Yet adoption of these tests later in the pandemic was limited as high per test cost and assay time made rapid lateral flow tests more appealing.

Figure 10. Commercial home-based NAATs for SARS-CoV-2 testing. Lucira Check-It and Cue Health Systems

1.4 Challenges and Unmeet Diagnostic Needs of POC NAAT Testing for SARS-CoV-2

Since the beginning of the COVID-19 pandemic, PCR testing has been a critical component in managing the pandemic but has had several challenges. Due to the requirement for rapid scale up and the sensitivity of PCR testing, establishing large-scale testing programs required a high degree of logistics and supporting infrastructure. From sample collection to processing and reporting results, each step of the process required coordination and resources. Due to the rapid influx of a high number of tests needing to be run, turnaround times varied significantly from hours to days, affecting the tests utility as a public health tool and limiting their effectiveness in rapid containment efforts. Further shortages of laboratory equipment, trained personnel, and necessary reagents (such as testing kits and RNA-extraction kits) limited testing capacity, highlighting the need for alternative testing mechanisms. Rapid antigen tests were developed to overcome the weakness of PCR testing: long assay times, slow sample to answer time, and low cost. However, these tests have inferior sensitivity compared to PCR tests as they are only used as a rule in not a rule out test.

To further reduce the sample to answer time while retaining the sensitivity and specificity of PCR, isothermal NAATS were developed. Several of these NAATS received FDA emergency authorization (Lucira, Cue, Aptidtude) for home use, allowing for highly sensitive and accurate distributed testing. These devices achieve simplification in user interaction, leveraging advancements in microfluidics and integrated the cartridge and reader. The requirement for onboard circuity and optics of these systems increased the complexity of these tests and resulted in a relatively test cost ($34-$90).

To bridge the benefits of PCR testing with rapid antigen testing an isothermal NAAT with lateral flow read out (LFA) is needed. The NAAT portion of the diagnostic will retain the sensitivity and specificity of PCR tests. Using isothermal methods allows for a rapid assay time that is resistant to typical inhibitors. NAAT testing also allows for duplexed reactions, adding a positive internal control to verify assay performance. The LFA readout will reduce the complexity of detection allowing for a reduced cost of manufacturing. The culmination of these properties will be an assay with the sensitivity and accuracy performance of PCR with the speed and cost of a rapid antigen test.

1.5 HIV Epidemic

The Human Immunodeficiency Virus (HIV), the etiological agent of the Acquired Immune Deficiency Syndrome (AIDS), was first identified in 1981, marking the beginning of a global health crisis that continues to affect millions worldwide. [102] Since its discovery, HIV has been responsible for approximately 80 million infections and 36 million deaths due to AIDS-related illnesses. [103] As of the end of 2020, the World Health Organization (WHO) estimated that 37.7 million people were living with HIV/AIDS globally, with 680,000 deaths occurring in that year alone. [104] The disease disproportionately burdens low- and middle-income countries, particularly in sub-Saharan Africa, which accounts for 70% of the global case count (Figure 11). [105]

HIV is a bloodborne virus that can also be transmitted through other potentially infectious materials, including semen, vaginal fluids, and breast milk.[106] The virus is characterized as an enveloped, positive-sense single-stranded RNA virus with a relatively small genome of 9.7 kilobases. It encodes 9 proteins and primarily targets CD4+ cells, a critical component of the human immune system.[107] By infecting and depleting these cells, HIV severely compromises the body's ability to fight off infections, eventually leading to death from opportunistic infections in the absence of effective treatment.[108]

One of the challenges in combating HIV/AIDS is the difficulty in diagnosing the infection. Often, individuals do not exhibit symptoms for years following infection, despite being capable of transmitting

the virus to others. [109] Additionally, the virus exhibits significant geographic diversity, with the main group M virus having nine subtypes. Subtype B is predominantly found in North America and Europe, while subtype C is common in South Africa.[110,111] Other subtypes, such as O and N, are primarily observed in smaller sections of Central Africa, indicating the virus's ability to mutate and adapt to different populations.[112]

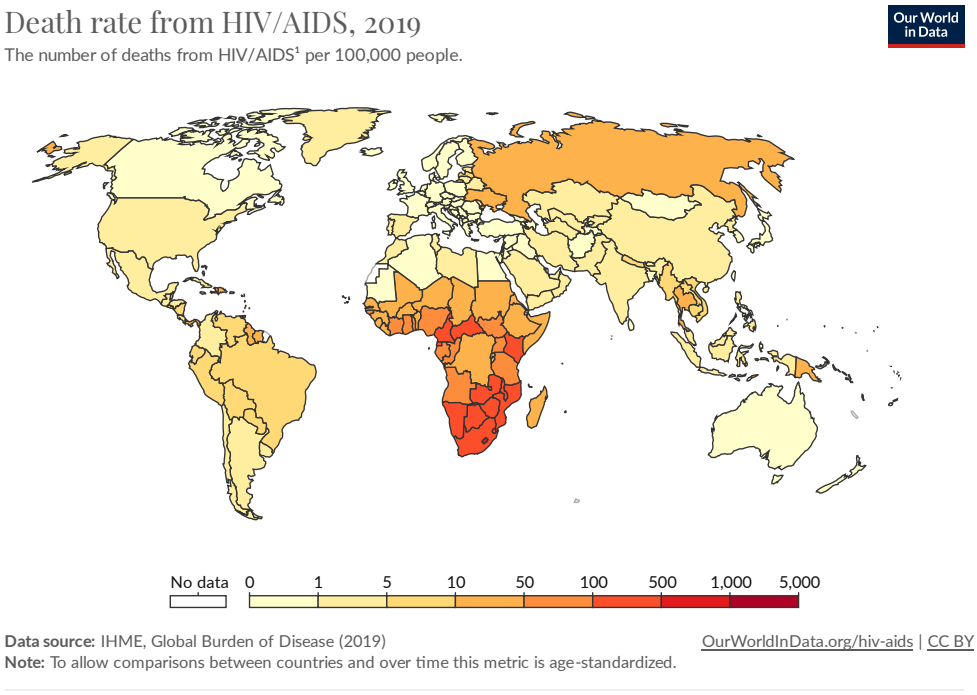

Figure 11. Death rate of HIV. Low- and middle-income countries are the most heavily burdened with HIV

Antiretroviral therapy (ART) has been a monumental advancement in controlling the HIV/AIDS pandemic. This therapeutic approach works by inhibiting the virus's ability to replicate within cells, effectively halting the progression of the virus. The success of ART is largely due to the development and use of several key classes of drugs, each targeting different stages of the viral life cycle. Reverse Transcriptase Inhibitors (e.g., Tenofovir) act as nucleotide analogues, inhibiting the reverse transcription process by which the viral RNA is converted into DNA, a crucial step for viral replication. Integrase Inhibitors (e.g., Bictegravir) prevent the viral DNA from integrating into the host cell's genome by inhibiting the integrase strand transfer process, a necessary step for the virus to replicate.[113] Protease Inhibitors (e.g., Darunavir) bind to the catalytic site of the HIV protease enzyme, blocking the cleavage of viral polyprotein precursors into functional proteins, thus preventing the maturation of new viral particles.[114] In 2020, an estimated 27.5 million people worldwide were receiving ART.[115] The widespread use of ART has led to significant viral suppression

among those treated, resulting in decreased HIV mortality rates and the virtual elimination of transmission.[116,117] Additionally, ART has been employed prophylactically for individuals at high risk of HIV infection as Pre-exposure Prophylaxis (PrEP), further reducing the chances of transmission.[118,119]

In 2014, the Joint United Nations Programme on HIV/AIDS (UNAIDS) set ambitious 90-90-90 targets to be achieved by 2020. These targets aimed for 90% of people living with HIV (PLHIV) to know their status, 90% of those who know their status to be receiving ART, and 90% of those on ART to achieve viral suppression. By 2020, progress toward these targets showed that 81% of PLHIV knew their status, 79% of those were on ART, and 92% of those treated were virally suppressed.[115] However, overall, only 59% of PLHIV had achieved viral suppression, indicating areas where further efforts are needed.

1.5.1 Need for Viral Load Testing

Viral load testing stands as a crucial tool in the control and management of the HIV pandemic. Viral load tests measure the levels of HIV RNA in the plasma extracted from whole blood and serve as an indicator of the disease's state and the efficacy of ART. The ability to quantify the viral load provides healthcare providers with essential data to tailor treatment plans effectively and monitor the patient's response to therapy. Regulatory agencies worldwide have established various definitions for viral suppression, reflecting the test's significance in disease management. The World Health Organization (WHO) considers viral suppression to occur at levels below 1,000 copies/mL, while both the Centers for Disease Control and Prevention (CDC) in the United States and the European AIDS Clinical Society (EACS) set a lower threshold, CDC at less than 200 copies/mL and EACS at less than 50 copies per mL. A crucial milestone in HIV treatment is achieving an "undetectable" viral load, which has led to the widely accepted principle that "undetectable equals untransmittable" (U=U), highlighting the reduced risk of HIV transmission.[120] Conversely, viral loads exceeding 1,000 copies/mL in patients undergoing ART are typically indicative of viral rebound, prompting clinical decisions to modify treatment regimens, often involving the switch to second-line drugs.[121] Regular monitoring through viral load tests, recommended every 3 to 12 months for patients on ART, is essential for timely adjustments to treatment plans and ensuring ongoing viral suppression.[122]

Moreover, viral load testing serves as the earliest detection mechanism for new HIV infections, with the virus becoming detectable as soon as 10 days post-exposure. This is significantly sooner than the detection window for HIV antigens, which appears 20 to 24 days following exposure.[7,123] Despite its critical role in early detection and management of HIV, the widespread implementation of viral load testing is hampered by its high resource requirements. This limitation restricts testing capabilities primarily to central

laboratories, resulting in only 60% of people living with HIV (PLHIV) having regular access to these tests. To achieve the UNAIDS 90-90-90 targets, approximately 60 million viral load tests are needed. [124] Highlighting the need for rapid and available testing.

1.5.2 Process Flow for Viral Load Testing

HIV viral load testing involves several complex steps. These include sample collection, blood fractionation, viral lysis, RNA extraction, amplification, and detection (Figure 12). One of the significant challenges lies in preparing the sample for "sample-to-answer" viral load tests. This preparation requires blood fractionation, virion lysis, and nucleic acid extraction before proceeding to downstream amplification and detection.

When conducting POC viral load testing, whole blood samples can be obtained through various methods: venipuncture (using 0.2 to 2 ml of blood), heel prick, or finger prick (using less than 200 µl of blood).[125,126] To improve amplification and reduce proviral DNA, the plasma is separated from the whole and the other constituents of whole blood are removed.[127,128] There have been developments in plasma separation that involve centrifugation, sedimentation, and membranes.[129–131]

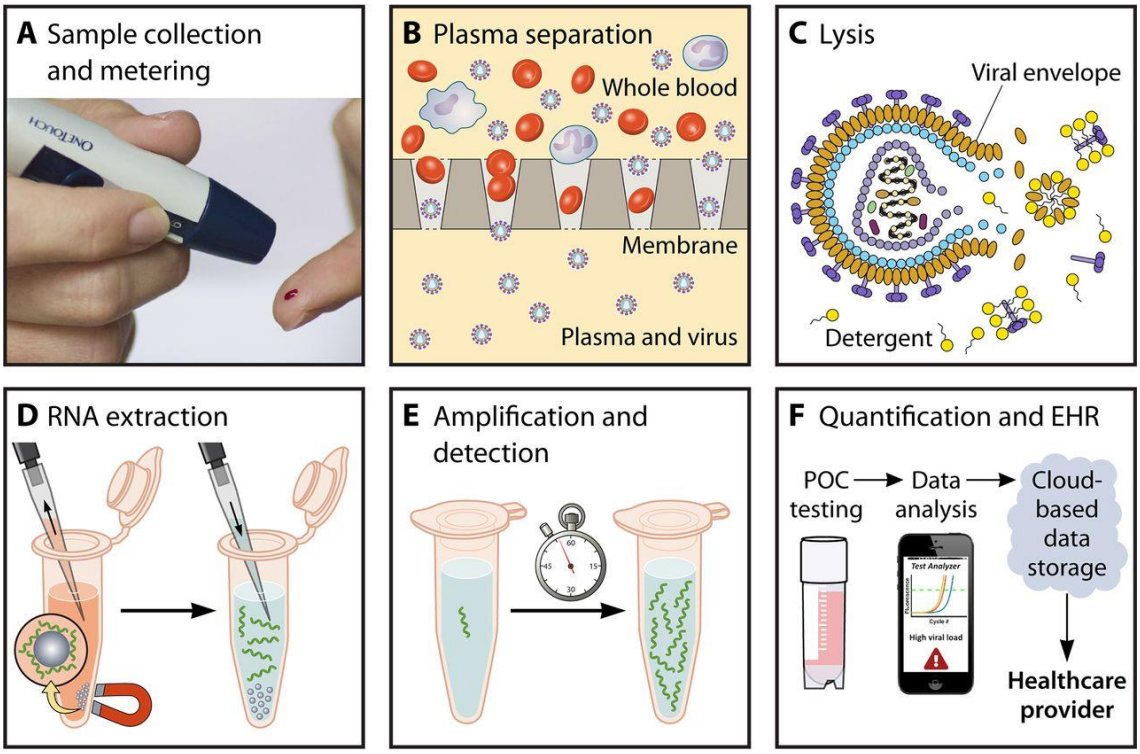

Figure 12. Various steps for a potential POC HIV viral load test.[132]

Once purified plasma is obtained, the work flow is similar to that in NAAT workflow above. Extracting the genomic RNA material from the HIV virion is crucial. The virion can be lysed with heating, detergents, enzymes, or chaotropic salts (71–74).[133–135] With the RNA free, purification is necessary to reduce contamination and inhibitory agents in downstream amplification. Solid phase extraction is the gold standard method, yet requires high concentrations of chaotropic salts and washing steps.[38] Research has been carried out to reduce the complexity of these streps suitable for a POC paper-based devices, such as chitosan-coated membranes[136] and electrophoretic separation of nucleic acids from blood.[67] Despite this, automated sample preparation of HIV lysis and RNA extraction from blood samples remains a challenge.[137,138]

qPCR has been the gold standard for NAAT testing for HIV.[139] Due to the requirements of thermocycling, stable power, aseptic preparation areas, and high purity target materials, PCR assays are difficult to employ at the POC. Many isothermal assays have been proposed that do not require thermocycling, are more robust to contaminants and inhibitors, and have faster run times.[71,140–142] Yet these assays lack quantification ability which is critical for clinical decision making.

1.5.3 Clinical Laboratory testing

Various molecular platforms exist for accurate, high-throughput HIV viral load testing (Hologic Panther Fusion, Abbott m2000, Roche cobas). These platforms integrate and automate the sample preparation and amplification using robotic or microfluidic manipulation allowing for 100s-1,000s of tests to be completed per hour. However, these methods typically require highly resourced laboratory infrastructure, highly skilled technicians, and large upfront investment (>200,000 USD). In remote locations, logistical challenges arise when transporting samples to centralized laboratory facilities, including scheduling specimen pick-up, maintaining sample integrity, and communication of results. POC assays offer an alternative by allowing testing outside of centralized labs, but they encounter specific limitations.

1.5.4 POC HIV Testing

To reduce the barriers in centralized laboratory testing, especially in remote clinical settings with limited resources, POC assays must function effectively under extreme environmental conditions (such as high temperatures, humidity, and dust). They should also minimize reliance on power supplies, facilitate simple sample collection, and feature automated equipment for user-friendly operation following minimal training. Furthermore, a POC HIV viral load assay must convey information about viremia levels consistent with

clinical standards for identifying virological failure. Currently, the World Health Organization (WHO) defines this threshold as 1,000 RNA copies/ml. Considering the availability of newer, more effective medications for viral suppression, modern POC HIV viral load assays should achieve a lower limit of quantification (200 copies/ml to meet EACS standards). Additionally, these assays should be user-friendly for local healthcare workers with minimal training. Ensuring diagnostic accuracy across diverse contexts remains critical for successful POC viral load testing.

1.5.5 Commercially Available Testing

In response to the global health challenges posed by HIV, several diagnostic devices have been developed. For HIV viral load monitoring, devices such as the Abbott m-PIMA, Diagnostics for the Real World's SAMBA II, and the Cepheid GeneXpert have made significant inroads (Figure 13). These devices have simplified preparatory steps and leverage advancements in microfluidics and cartridge-reader integration. As a result, several have been granted CLIA waiver status.[49] In the case of HIV viral load testing, devices like the Cepheid GeneXpert have been effectively deployed, requiring only a small volume of centrifuged blood to separate plasma for analysis. The GeneXpert only requires 1 mL of plasma and can deliver results within 91 minutes with a sensitivity of 14 copies per milliliter, and is capable of quantifying M, O, N, and P subtypes.[143–145]

Figure 13. Commercialized point-of-care NAATs for HIV viral load testing. (A) Abbott m-Pima (B) DRW Samba II (C) GeneXpert II

In the case of HIV viral load testing, despite these advancements, challenges remain. The cost of equipment, such as readers which can range between $10,000 to $25,000, and the ongoing need for consumable cartridges, present financial barriers.[132,146] Furthermore, while the requirement for technical training has been reduced, it has not been eliminated. The necessity of a power source also persists. As such, there is a clear need for continued innovation in this field. Efforts to further reduce the costs associated with testing,

shorten the time to results, simplify user procedures, and minimize training requirements are essential. Such innovations are critical for expanding the scope and reach of dispersed testing programs, making them more accessible to a wider range of users.

1.6 Challenges and Unmet Diagnostic Needs for POC NAAT Testing for HIV

Blood borne diseases pose a challenge for POC NAATs due to the complexity of blood as a sampling medium and is exacerbated by intricacies of HIV. HIV replicates in CD4+ cells as HIV inserts and integrates its proviral DNA within the cellular genome for viral component replication thus viral load assays cannot distinguish between viral RNA and proviral DNA which can inflate viral load measurements. To circumvent this issue many assays use plasma as the sample media in place of whole blood so only viral RNA is measured. This necessitates a separation step adding to the complexity of a potential POC device. Further, hemoglobin and nucleases found in blood must be removed and inactivated during sample preparation as these are known amplification inhibitors. HIV is also a genetically diverse virus with HIV-1 having four groups that are further split into additional subtypes. This genetic diversity makes nucleic acid targeting difficult as mismatched primers can result in reduced or non-amplification. The relevant and necessary limits of detection in viral load monitoring are also extremely demanding. A published target product profile proposes an optimal limit of detection of 200 copies/ml and sample specimen of less than 200 µl of finger capillary blood. Considering plasma is around 55% of blood by volume that leaves only 22 copies of RNA for amplification, the limit of most assays in ideal conditions forgoing any preparation steps. Thus, there is an unmet need for a POC device that automates all diagnostic steps, including sample preparation and amplification, ideally without high electrical power demands and instrumentation costs for robotics, optics, or pumps.

1.7 Research objectives

In the work I present in this document I aim to address bottlenecks amplification and detection in the NAAT testing workflow. For SARS-CoV-2 I will do this using a novel implementation of internal control mechanisms for sample validation to report on the preparation, amplification, and detection of SARS-CoV-2. This work blends the sensitivity and specificity of a PCR based diagnostic test with the speed and ease of use of a rapid antigen test. Then, as I detailed in previous sections, I have demonstrated the need and requirements of HIV viral load testing at the point-of-care. For HIV I will implement a novel assay for the

extended dynamic range for HIV viral load testing. In order to address these objectives, I will detail the following works:

1. Development of a one-pot, duplexed RT-RPA SARS-CoV-2 assay with an MS2 bacteriophage as a full process control.
2. Improve the upper quantifiable range of ANSA using physiochemical optimization to allow for more distinct nucleation sites to be counted.
3. Develop machine learning models to accurately extend the dynamic range of ANSA by extracting additional information from image data.

2 SARS-CoV-2 recombinase polymerase amplification assay with lateral flow readout and duplexed full process internal control

2.1 Introduction

From the onset of the SARS-CoV-2 pandemic, diagnostic testing has played a crucial role in monitoring and diagnosing new infectious cases. SARS-CoV-2 and the associated COVID-19 disease is expected to circulate indefinitely as SARS-CoV-2 continues to mutate, introducing new sub-variants with enhanced immune evasion.[147] Diagnostics will continue to play a key role in the timely identification of new cases to stop the spread of disease, inform masking and isolation standards, initiate clinical decisions with patient care plans (e.g., monoclonal antibodies, Paxlovid, etc.), and ensuring safe community gatherings and public openings.[99]

Isothermal NAATs with LFA readout can offer the high diagnostic accuracy of RT-PCR and the low-cost and ease of use of antigen-based LFAs. Recombinase polymerase amplification (RPA) is an attractive isothermal amplification method due to its speed (<15 mins), accuracy, and low incubation temperature (~40 °C). Early in the pandemic, multiple SARS-CoV-2 RPA assays were published that targeted either the nucleocapsid (N)[148–151], spike (S)[150,152], RNA dependent RNA polymerase (RdRp)[153], or open reading frame 1 (ORF1ab)[152,154] genes with analytical sensitivities as low as 10 RNA copies per reaction while leveraging fluorescent output and/or lateral flow detection. Several RPA assays using LFA detection have incorporated duplexing of multiple SARS targets, RNase P for sampling validation, or simultaneous detection of SARS-CoV-2 and influenza virus targets.[155–159] While targeting the human RNase P gene is useful for confirming sampling integrity from a human source, it is not a full process internal control as it is DNA-based and fails to report on potential RNA degradation and reverse transcription.

In this work, I report on the development of a one-pot, duplexed RT-RPA SARS-CoV-2 assay with an MS2 bacteriophage as a full process control. The duplexed assay can detect amplicons with real-time fluorescence or lateral flow readout using commercially available RPA reagent kits that include an exonuclease for molecular probe cleavage (TwistAmp Exo). The MS2 bacteriophage process control reports on successful operation of lysis, reverse transcription, and amplification. The assay has a SARS-CoV-2 RNA sensitivity of 25 copies per reaction when using fluorescence readout and 50 copies per reaction with lateral flow detection. We also demonstrate the ability of the current assay to detect the SARS-CoV-2 Delta and Omicron variants. To our knowledge, this is the first report of a duplexed SARS-CoV-2 lateral flow

detection assay to incorporate a full process internal control that reports on lysis, reverse transcription, and amplification. This is also the first reported usage of TwistAmp exo RPA kits for both fluorescence and lateral flow readout, opening the potential for multiple assay readout options with a single reagent format given the resources at the point of testing.

2.2 Materials and Methods

2.2.1 SARS CoV-2 Virus RNA and Virion Stocks

Purified RNA for influenza A (NR-2773), influenza B (NR-10047), HCoV-NL63 (NR-44105), HCoV-OC43 (NR-52727), HCoV-229E (NR-52728), SARS-CoV-2 Delta Lineage B.1.617.2 (NR-56127), and SARS-CoV-2 Omicron Lineage B.1.1.529 (NR-56494) were used for the specificity analysis and variant detection (BEI resources, USA). Intact bacteriophage MS2 was grown and isolated using an established protocol.[160] Quantified SARS-CoV-2 virus inactivated via gamma irradiation (NR-52287) was obtained from BEI Resources. All purified RNA and virus stocks were stored at -80°C until use.

2.2.2 SARS-CoV-2 RT-RPA Assay Development and Fluorescence Readout

Monoplex SARS-CoV-2 RPA reactions contained 29.5 µL TwistAmp rehydration buffer (TwistDx Limited, UK), 2.6 µL of 10 µM forward primer, 2.6 µL of 10 µM reverse primer (Integrated DNA Technologies, USA), 0.75 µL of 10 µM FAM-labeled probe (Eurogentec, Belgium), 0.5 µL of 50 U/µL reverse transcriptase (Agilent AffinityScript, USA), 5 µL of quantified synthetic SARS-CoV-2 RNA (Twist Bioscience, USA), and 6.55 µL of nuclease-free water added to a TwistAmp Exo pellet (TwistDx Limited, UK). 2.5 µL of 280 mM of magnesium acetate (TwistDx Limited, UK) was added to the RPA tube cap, bringing the total reaction volume to 50 µL. We agitated the tubes by repeatedly inverting them for 20 seconds to activate the DNA polymerase with the magnesium cofactor before placing them in a benchtop fluorometer designed for use with isothermal nucleic acid amplification assays (Axxin T16, Axxin, AUS). The RT-RPA protocol consists of an initial five-minute incubation step at 39°C, after which the reaction tubes are removed from the fluorometer, agitated for 30 seconds, placed back into the fluorometer, and incubated for 10 additional minutes. The LED intensity setting of the T16 fluorometer was set to 7% for the FAM channel.

The RT-RPA assay was designed to target the nucleocapsid (N) gene based on the SARS-CoV-2 reference genome (GenBank NC_045512). The assay uses an internally quenched fluorophore probe that was designed using computational and manual methods. Candidate probe sequences were generated using RPA assay design software PrimedRPA.[161] The final probe sequence for the assay was selected based on the

location of available thymine residues for an internally quenched fluorophore, genome conservation through alignment of other available sequences, and low degree of homology through BLAST alignment of other respiratory viruses. Twelve primer pairs were then designed around this probe sequence using PrimedRPA[161] and screened using RT-RPA with fluorescence readout. The best primer candidates were chosen based on time to threshold and slope of the exponential amplification curve. The primers were redesigned with single base-pair shifts and length changes for second round screening, following the TwistDx assay design manual. The primers were again screened for optimal time to threshold. In total, 21 different primer pairs were evaluated with the top performing pair being selected for subsequent experiments (Figure 14). The resulting primer pair (Table 1) displayed the shortest time to threshold and the steepest exponential amplification slope. MS2 primers and probe are provided in Table 1.[162]

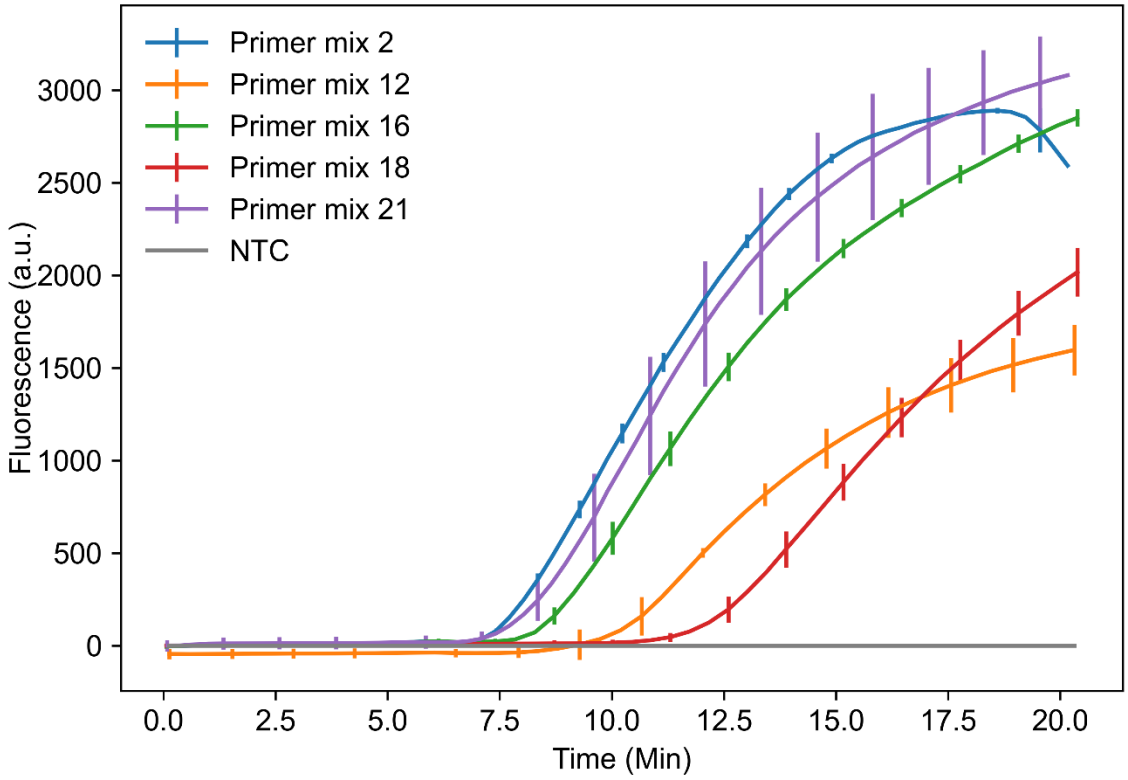

Figure 14. SARS-CoV-2 primer screening. Primers were designed following the Twist RPA design manual. All primer mixes were tested at 103 copies per reaction. Lines show an average of three replicates with error bars as the replicate standard deviation. Primer mix 2 was selected as the optimal primer combination and used for all subsequent testing.

Sequence-specific amplicon detection of SARS-CoV-2 and MS2 via RT-RPA employs enzymatically-cleaved homologous probes. These probes have 48 base pairs, use a FAM or ROX fluorophore, a tetrahydrofuran (THF) residue, an internal quencher (only in fluorescence readout probe design), and a 3'

block to inhibit probe extension. The fluorescence detection mechanism for SARS-CoV-2 uses a thymine modified with a FAM fluorophore that is 5' of a proximal THF site and a subsequent thymine modified with an internal fluorophore quencher, as detailed elsewhere.[163] Fluorescence detection of MS2 follows the same methodology with the difference of a ROX fluorophore in place of the FAM fluorophore. Given sufficient sequence homology, the DNA exonuclease III (Exo) acts on the THF site, freeing the fluorophore and quencher and allowing for fluorescence. While this assay utilizes a sequence-specific probe, perfect homology across the primer and probe targeting region is not required as RPA has been shown to tolerate up to 15 mismatches, allowing for a high degree of cross variant detection.[71] In silico alignments displayed two total mismatches for the delta variant with a G to T mutation on the probe's first 5' base, the other mutation occurs outside the primer or probe regions. Alignments also show 3 consecutive mismatches (GGG to AAC) in the omicron variant. These occur outside the primer and probe hybridization regions, and therefore do not impact the assay's performance.

Duplexed RT-RPA assays with fluorescence readout used the same reaction protocol as outlined above, with adjustments to include MS2 bacteriophage RNA, primers, and probe. Duplexed RT-RPA reactions for SARS-CoV-2 and MS2 included 1.08 µL of 10 µM MS2 forward primer, 1.08 µL of 10 µM MS2 reverse primer (Integrated DNA Technologies, USA), 0.19 µL of 10 µM MS2 probe labeled with a ROX fluorophore (LGC Biosearch Technologies, UK), 2 µL of 4.2×10^5 copies per µL (cps/µL) MS2 RNA (Sigma Aldrich, USA), and nuclease-free water as needed to achieve a total reaction volume of 50 µL. As outlined above, tubes were agitated immediately before placing in an Axxin T16 for incubation at 39°C and fluorescence readout. The LED intensity setting in the FAM channel was set to 7% while the ROX LED intensity was set to 52%.

2.2.3 Lateral Flow Detection of SARS-Cov-2 RT-RPA Assay

For LFA detection assays, both the reverse SARS-CoV-2 primer and MS2 reverse primer had a biotin and digoxigenin moiety added respectively while the MS2 probe utilized a 5' FAM fluorophore in place of the internal ROX. Reactions were run as described earlier except the final concentration of SARS-CoV-2 forward and reverse primers were 420 nM each with 120 nM of probe and MS2 forward and reverse primers were 210 nM with 60 nM probe. After incubation at 39°C, we diluted the RPA product 1:25 in running buffer (HybriDetect 2T, Milenia Biotec, Germany), and pipetted 10 µL of diluted product directly onto a lateral flow test strip (HybriDetect 2T, Milenia Biotec, Germany) before placing the LFA vertically in a tube with 80 µL of running buffer (HybriDetect 2T, Milenia Biotec, Germany). The immediate dilution negated the need to stop the reaction with EDTA.

After eight minutes of run time, the LFA test strips were removed, pat dried with a Kem wipe (Kimberly-Clark, USA) and scanned with an Epson V370 photo flatbed scanner for use in code-based image analysis. The LFA images were processed by a code (Python 3.10) that calculates the line average intensity of the test line region. A positive result was determined if the line intensity of the test line exceeded the intensity threshold set by the average of all NTCs plus three standard deviations. For qualitative presentation here, the LFA were dried and digitally imaged (EOS Rebel T3, Canon) with a 60mm macro lens.

Duplexed RT-RPA with lateral flow detection leveraged the chemistry above with the addition of MS2 RNA, primers, and probe. Duplexed reactions included 1.05 μL of 10 μM forward primer, 1.05 μL of 10 μM MS2 reverse primer labeled with digoxigenin, 0.3 μL of 10 μM MS2 probe labeled with a FAM fluorophore (Integrated DNA Technologies), 2 μL of 4.2×10^5 cps/μL MS2 RNA (Sigma Aldrich), and nuclease-free water as needed for a 50 μL total reaction volume. The duplexed assay with LFA readout was conducted in the same manner as outlined for single target detection.

Table 1 Optimal primer and probe sequences for the SARS-CoV-2 assay.

Oligo	**Sequence**
SARS-CoV-2 Forward	AAGCCTCTTCTCGTTCCTCATCACGTAG
SARS-CoV-2 Reverse	GTTGGCCTTTACCAGACATTTTGCTCTCA
SARS-CoV-2 Reverse Lateral Flow	GTTGGCCTTTACCAGACATTTTGCTCTCA-[biotin]
SARS-CoV-2 Probe	GGCGGTGATGCTGCTCTTGCTTTGCTGC-[T(FAM)]-G-dSpacer-[T(BHQ1)]-TGACAGATTGAACCAGC-Spacer C3
MS2 Forward Primer	TCGAGAGAAAGATCGCGAGGAAGATCAATACATA
MS2 Reverse Primer	CCTCAGCAATCGCAGCAAACTCCGGCATCTACT
MS2 Reverse Primer – Lateral Flow	CCTCAGCAATCGCAGCAAACTCCGGCATCTACT-[DIG]
MS2 Probe – Fluorescence	CTTCTTTGTTGTCTTCGACATGGGTAA-[T(ROX)]-C-dSpacer-[T(BHQ2)]-CATGTTTGAATGGCC-Spacer C3
MS2 Probe – Lateral Flow	[FAM]-CTTCTTTGTTGTCTTCGACATGGGTAATC-dSpacer-TCATGTTTGAATGGCC-Spacer C3

We use two different RPA probe designs in the LFA assay, which are detailed in Table S1. The first is an internally quenched probe targeting SARS-CoV-2 that is also used for fluorescence readout. The second is

a probe with an unquenched 5' terminal fluorophore label for MS2 amplicon detection as described in the TwistDx design manual and as published in past RPA assays with LFA readout.[163–165] LFA "sandwich" immunochemistry detection on a nitrocellulose strip uses these RPA probes combined with modified primers: 5' biotinylated SARS-CoV-2 reverse primer and 5' digoxigenin-labeled MS2 reverse primer. LFA banding visualization is based on the binding of a dual labeled RPA product being "sandwiched" between the immobilized receptor and an anti-FAM antibody conjugated to a gold nanoparticle. The first binding domain detects the SARS-CoV-2 amplification product which is labeled via the biotinylated reverse primer and cleaved FAM probe, as illustrated in Figure 15. The second binding domain detects the MS2 amplification product which is similarly labeled with digoxigenin and FAM. The third binding domain serves as the LFA flow control by capturing conjugated gold nanoparticles that did not bind to RPA products.

2.2.4 Viral Lysis and MS2 Bacteriophage Internal Control

For viral lysis studies, inactivated SARS-CoV-2 and MS2 viral stocks were diluted in PBS pH 8.0 buffer to 600 genome copies per µL. To ensure no extracellular RNA was present in the samples prior to lysis, 5 µL of the viral samples were treated with 5 µL of 10 mg/mL RNase A (ThermoFisher) followed by an inactivation step of 5 µL of RNasin™ Plus Ribonuclease Inhibitor (Promega, USA). These steps were carried out sequentially at 37°C for 5 minutes each to degrade free RNA prior to lysis. Heat lysis was completed with incubation at 95°C for 5 minutes. 5 µL of the lysate was then spiked directly into RT-RPA reactions. Non-lysed controls without the 95°C heat lysis step were run to verify the absence of free RNA in viral stocks.

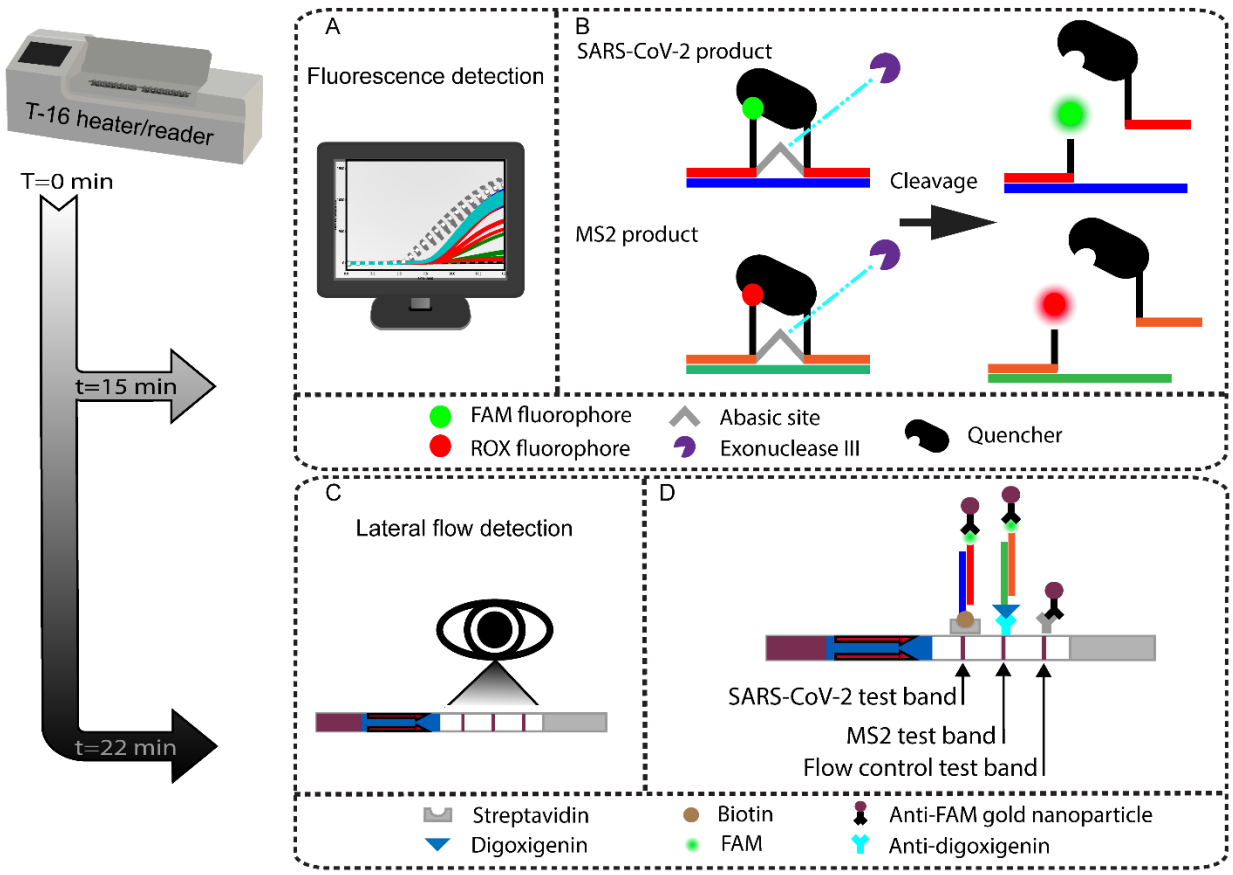

Figure 15. Overview of the COAST assay. Illustration of the duplexed RT-RPA assay with either real-time fluorescence or LFA-based detection. **(A)** The one-pot RT-RPA assay can be read out in real time using a fluorometer held at a constant 39°C. **(B)** Mechanism of Exonuclease cleaved fluorophore and quencher pairs for real-time multiplexed detection. When the SARS-CoV-2 amplicon is cleaved, the FAM fluorophore is detected. When the MS2 product is cleaved, the ROX fluorophore is detected. **(C)** Duplexed endpoint detection is also possible by LFA. **(D)** Design of the LFA. The LFA test strip is comprised of three ligand-receptor binding domains and includes the flow control line, labeled MS2 process control test line, and labeled SARS-CoV-2 test line.

2.3 Results and Discussion

We evaluated the limit of detection (LOD) of the RT-RPA assay for SARS-CoV-2 and duplexed detection of SARS-CoV-2 and the MS2 internal control using fluorescence readout. Figure 17A shows real-time RT-RPA fluorescence intensities over a 15-minute incubation for reactions ranging from 5 to 250 SARS-CoV-2 RNA copies per reaction (cps/rxn) with five replicates at each concentration. Figure 17B shows SARS-CoV-2 and MS2 duplexed RT-RPA reactions with varying SARS-CoV-2 RNA concentrations and 8×10^4 cps/rxn of MS2 RNA for all experiments. For all duplexed reactions at varying SARS-CoV-2 input copies,

the corresponding MS2 reactions successfully amplified, except the no template controls (NTCs) which contained no SARS-CoV-2 or MS2 RNA. For both the mono and duplex RT-RPA reactions, we observe strong amplification in less than 10 minutes down to 25 cps/rxn of each replicate. We also evaluated the RT-RPA assay at copy loads greater than 250 cps/rxn, up to 5×10^5 cps/rxn, which all amplified consistently (Figure 16). We observed more variability in exponential amplification slope and time to threshold in the low copy replicates. A similar effect has been observed in other RPA studies.[65,155] Figure 17B also demonstrates the effect of multiplexing on the reaction as the time to threshold and total overall fluorescence output of the SARS-CoV-2 assay is inhibited when compared to the monoplexed reaction. This inhibition is due to the competition of the SARS-CoV-2 and MS2 primers and probes for the limited RPA reagents needed for amplification.

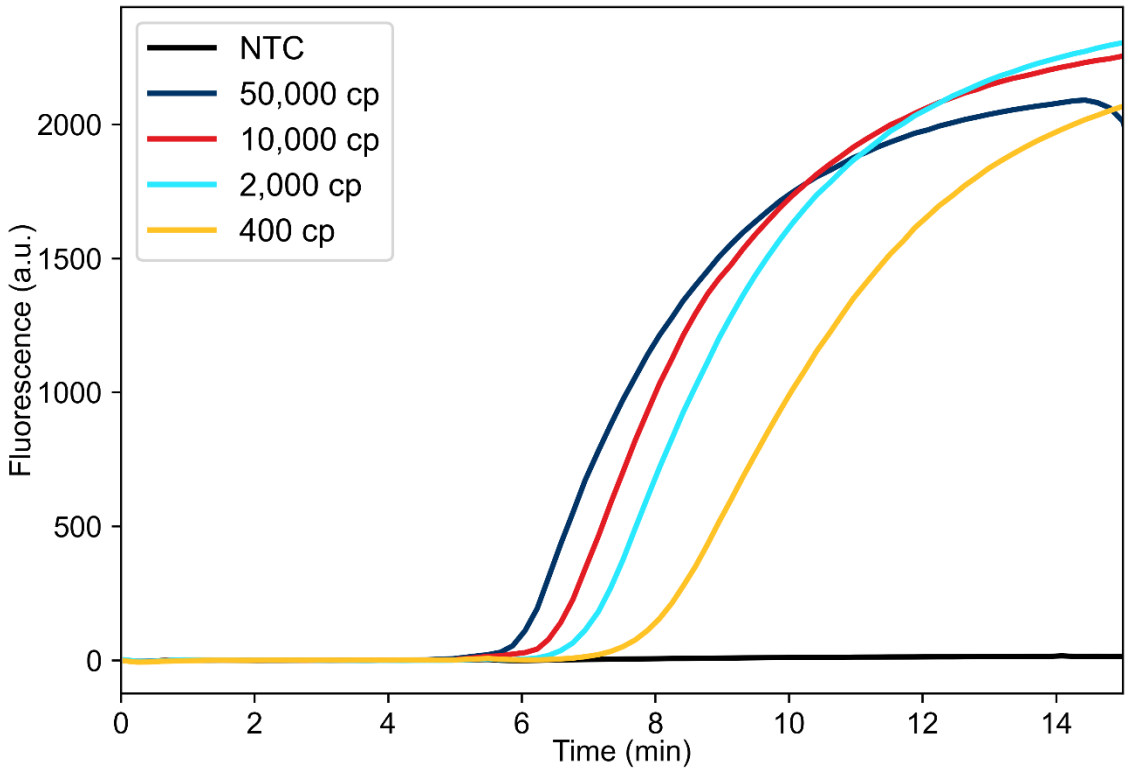

Figure 16. SARS-CoV-2 detection at high copy input. Detection of copies per reaction of RNA by the single target SARS-CoV-2 assay. All tested RNA input from 50,000-25 copies per reaction amplified successfully in one pot RT-RPA.

Within the duplex RT-RPA assay, the MS2 input copies and concentrations of primers and probe were optimized to retain a low LOD for SARS-CoV-2 detection, while also consistently amplifying the MS2 internal control. The SARS-CoV-2 primer and probe concentrations were conserved throughout both the mono and duplexed assays. MS2 primer and probe concentrations were determined through a systematic

screening of lower MS2 oligo concentrations while maintaining SARS-CoV-2 assay performance. Concurrent with the oligo concentration, we evaluated MS2 input copies on the amplification behavior. The final concentration of MS2 RNA in the assay was determined through optimization such that the time to threshold of the MS2 amplification was less than 7 minutes and all MS2 reactions consistently amplified regardless of input copy load of SARS-CoV-2 RNA. We observed that the optimal total oligonucleotide concentration in the reaction was 1540 µM. Further increases in the oligo concentration demonstrated increased time to threshold and reduced exponential amplification slope, resulting in worse duplexed assay performance. We hypothesize that the decrease in performance is due to oligo saturation of the single stranded binding proteins and/or recombinase proteins, which inhibits the strand invasion and primer hybridization steps of RPA.

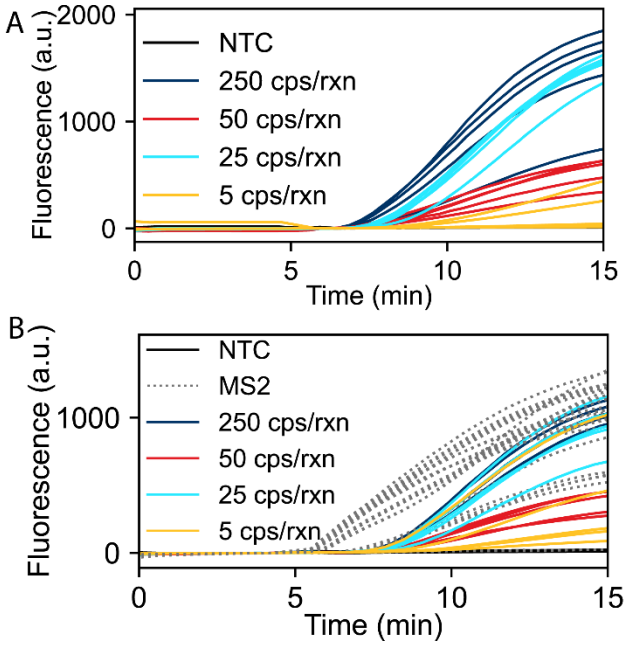

Figure 17. RT-RPA amplification of SARS-CoV-2 RNA. The number of RNA target copies given per reaction. **(A)** Single target detection of SARS-CoV-2 (N=5). **(B)** Duplexed detection of SARS-CoV-2 and MS2 (N=5). All reactions containing MS2 RNA internal control amplified. Data shown with a baseline correction by subtracting the fluorescence value at 4 minutes.

In order to implement LFA detection of RT-RPA products, we explored different probe designs and TwistAmp RPA enzyme kits for LFA detection. Many previously published RPA assays with LFA readout use the TwistAmp nfo kit and a 5' unquenched fluorophore probe as in the TwistAmp RPA design manual.[163–165] At the time of experimentation, the TwistAmp nfo kit was discontinued and no longer

available for purchase from TwistDx Limited (now a subsidiary of Abbott Laboratories). Attempts were made to spike purchased endonuclease IV (nfo) enzyme to a TwistAmp basic kit with mild success (data not shown); however, through experimentation we found that sensitivity of the LFA assay was improved using the TwistAmp exo kits, which are typically reserved for real-time fluorescence readout. We evaluated the performance of the internally quenched fluorescence detection probe design compared to a 5' unquenched fluorophore LFA probe design and found the detection limit to be equivalent. Further discussion is available in the appendix section 6.1. To demonstrate the utility of these probe designs, we carried out all LFA readout experiments using the 5' unquenched FAM fluorophore probe design for MS2 detection and the internally quenched FAM fluorophore probe design for SARS-CoV-2 detection. We observed that employing TwistAmp exo kits and internally quenched probes enables dual readout, either through real-time fluorescence or endpoint LFA analysis. This is notable because RPA primer and probe screening is most efficiently performed using real-time fluorescence data to indicate optimal primer and probe combinations, which can then be leveraged directly for LFA readout if desired.

Using the RPA probe design, we conducted experiments to detect SARS-CoV-2 using RT-RPA paired with lateral flow readout. Figure 18 shows representative LFA strip images and quantitative measurement of LFA line intensities (5 strip average) for SARS-CoV-2. The images show positive lines for the flow controls and SARS-CoV-2 for all concentrations down to 25 copies per reaction. The MS2 LFA line is not present, as expected, because the MS2 RNA, primers, and probe are not included in the monoplex version of the assay. The quantitative results in Figure 18B show that the line intensity increases with increasing input copy numbers.

We repeated these lateral flow readout experiments with the duplex RT-RPA assay for SARS-CoV-2 with MS2 internal control. Figure 19 shows representative strip images of the duplexed LFA and quantitative measurement of LFA line intensities averaged over 5 replicates. The images show a positive line for the flow control, MS2 internal control, and the SARS-CoV-2 strip regions for all concentrations down to 25 copies per reaction. We observe that the MS2 line intensity levels are greater than the SARS-CoV-2 test lines. This is likely due to the excess MS2 RNA in the reaction. The quantitative analysis shows that the SARS-CoV-2 line intensity decreases with copy number, except at 25 cps/rxn where the average line intensity and standard deviation is much greater than expected. This is due to two replicates, one where the SARS-CoV-2 test stripe intensity was much greater than three replicates and one replicate that failed to develop a line at an intensity reaching the determination cut off both visually and by the objective code method. This low line intensity replicate was retested with the same result. As observed in the fluorescence

readout data in Figure 17, high variation in RT-RPA amplification is common near the limit of detection of the assay.

Table 2 summarizes the observed LODs of the RT-RPA assay with fluorescence or LFA readout for both monoplex detection of SARS-CoV-2 and duplexed detection of SARS-CoV-2 and the MS2 internal control. We list the detection fraction of SARS-CoV-2 RNA from 250 cps/rxn to 5 cps/rxn stratified by readout method and monoplexed versus duplexed target detection. RT-RPA with fluorescence readout demonstrated lower LOD with mixed positive results at 5 cps/rxn and a limit of detection of 25 cps/rxn in both single target and duplexed assays. Monoplexed RT-RPA with LFA readout exhibited a 100% SARS-CoV-2 detection rate down to 25 cps/rxn. The duplexed LFA of variable SARS-CoV-2 target and fixed MS2 target demonstrated 100% detection rate down to 50 cps/rxn and 80% detection rate at 25 cps/rxn. Neither monoplexed nor duplexed LFA could detect any LFA banding through either visual or analytical detection at 5 cps/rxn.

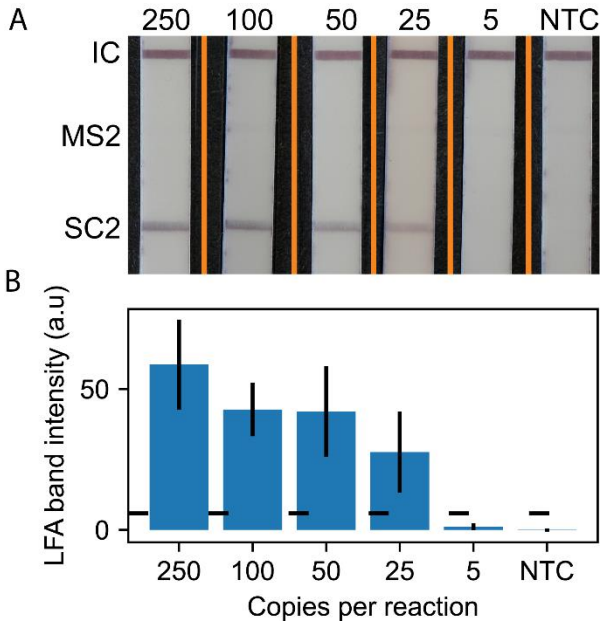

Figure 18. Monoplexed LFA analysis. A) Representative lateral flow test strip readouts for RT-RPA assays with varying SARS-CoV-2 RNA input copy numbers. Orange lines denote composite image, strips taken from separate images and merged into one. B) Average (N=5) SARS-CoV-2 test line intensity plotted with error bars representing one standard deviation (N=5 for all concentrations). The horizontal dotted line is the positive test threshold defined as the NTC SARS-CoV-2 test line average intensity plus three standard deviations.

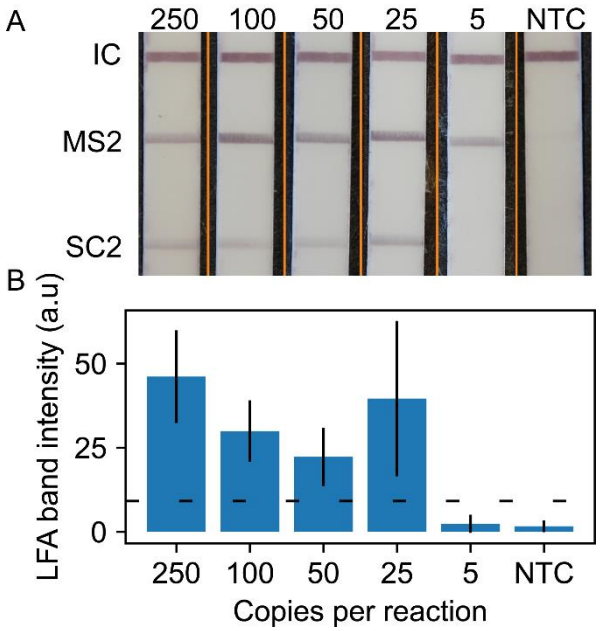

Figure 19. Duplexed LFA analysis. A) Representative test output. Orange lines denote composite image, strips taken from separate images and merged into one. B) Average (N=5) SARS-CoV-2 test line intensity. Horizontal dotted line is the positive test threshold defined as the NTC SARS-CoV-2 test line average intensity plus three standard deviations.

Table 2 Detection results of RT-RPA for respective assay and readout type. Positive test outcome threshold determined by NTC signal intensity average plus three standard deviations.

Detection Method	**250 cps/rxn**	**100 cps/rxn**	**50 cps/rxn**	**25 cps/rxn**	**5 cps/rxn**	**NTC**
Singleplex RT-RPA with fluorescence	5/5	5/5	5/5	5/5	3/5	0/5
Duplex RT-RPA with fluorescence	5/5	5/5	5/5	5/5	2/5	0/5
Singleplex RT-RPA with LFA	5/5	5/5	5/5	5/5	0/5	0/5
Duplex RT-RPA with LF A	5/5	5/5	5/5	4/5	0/5	0/5

The duplex RT-RPA assay with LFA readout was tested with other respiratory viruses in order to assess its analytical specificity. Table 3 shows detection of SARS-CoV-2 variants Delta B.1.617.2 and Omicron B.1.1.529 and cross-reactivity screening against genomic RNA from other common respiratory viruses. The data shows that the assay has no cross-reactivity with influenza A, influenza B, human coronavirus 229E (HCoV-229E), HCoV-NL63, or HCoV-OC43. The SARS-CoV-2 Delta and Omicron variants RNA were detected in all three replicates at input copy loads of 10^3 cps/rxn (Figure S6-7). We did not thoroughly evaluate the LOD for these variants of concern, but we expect similar results to Table 2 which used RNA from the ancestral SARS-CoV-2 strain. In alignments of these SARS-CoV-2 variant sequences with our RPA primers and probe, we discovered no mismatches in the hybridization regions; therefore, we anticipate no significant effect on limit of detection. There are some sublineages that introduce minimal mismatches with our RPA sequences, but we do not expect significant impacts to our assay's performance due to the mismatch tolerance of RPA that has been reported previously by our research group and others.[64,71]

Table 3 Other viral RNA screened with the duplexed RT-RPA LFA assay. We evaluated cross-reactivity using Flu A/B RNA and other common human coronaviruses. We demonstrated detection of SARS-CoV-2 variants of concern.

Virus	**Concentration (cps/rxn)**	**Positive replicates**
Flu A	10^3	0/3
Flu B	10^3	0/3
HCoV-229E	10^3	0/3
HCoV-NL63	10^3	0/3
HCoV-OC43	10^3	0/3
Delta	10^3	3/3
Omicron	10^3	3/3

We validated the internal MS2 viral control using heat for viral lysis and sample preparation. Heat lysis has been demonstrated as an effective viral lysis technique compatible with nucleic acid amplification assays.[150,166,167] We conducted a series of duplexed RT-RPA experiments with LFA readout at 10^3 copies per reaction (N=3) to demonstrate efficacy of heat-based lysis and the MS2 full process internal control. Prior to RT-RPA analysis, we pre-treated intact SARS-CoV-2 virus and MS2 bacteriophage to generate

four different samples: MS2 and SARS-CoV-2 both heat-lysed, only SARS-CoV-2 lysed, only MS2 lysed, and no lysing. Figure 20 shows representative images of LFA strips for RT-RPA of pretreated samples directly added to reactions. All four conditions yielded the expected results as using lysed materials permitted successful RT-RPA and LFA detection, while unlysed materials did not amplify and therefore gave negative test results. In instances where MS2 detection fails, this indicates an invalid test result due to a failure of one or more integral steps, and retesting is required. This result could be due to RNA degradation or unsuccessful viral lysis, reverse transcription, or amplification. Failure to use a full process internal control may increase risk of false negatives and misdiagnosis, which prevents immediate clinical interventions that mitigate community spread.

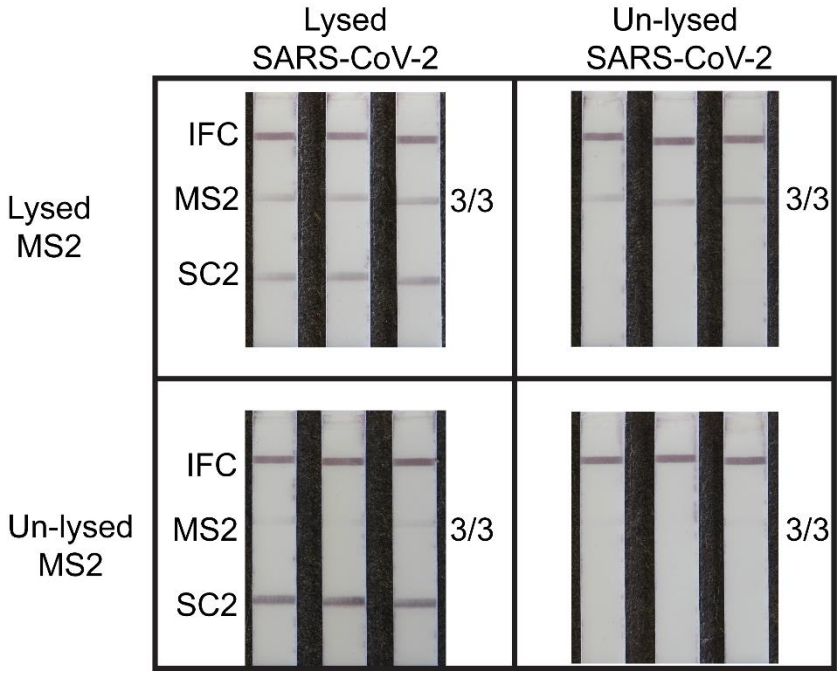

Figure 20. Images of LFA strips. Images demonstrating the successful lysis and RT-RPA of SARS-CoV-2 and the MS2 internal control. As expected, samples containing unlysed SARS-CoV-2 or MS2 are not successfully amplified and detected. The top row demonstrates true positive results (left) and true negative results (right) as the MS2 test line is detectable. The bottom left image demonstrates a failure of the MS2 internal control, even though SARS-CoV-2 is still detected. The bottom right image shows a complete assay failure where no banding is detected. Reading a valid test would require one of the two images from the top row. The bottom row demonstrates a failure in the internal control and an invalid test.

2.4 Summary

We developed a rapid, duplexed, single-pot RT-RPA nucleic acid amplification assay with lateral flow readout for SARS-CoV-2 with a MS2 bacteriophage as a full process internal control. We demonstrated the

duplexed amplification and detection of SARS-CoV-2 and MS2 in real time using both fluorescence readout with an LOD of 25 copies per reaction sensitivity with a reaction time of 15 minutes and end point visual readout using lateral flow strips with 50 copies per reaction sensitivity with test results in under 25 minutes. The assay detects both the delta and omicron SARS-CoV-2 variants and does not exhibit any cross-reactivity with influenza A, influenza B, or other common human coronaviruses (HCoV-NL63, HCoV-OC43 and HCoV-229E). We demonstrated that MS2 serves as a process control for lysis, reverse transcription, amplification, and readout. While we used an Axxin T16 to incubate the RPA reactions, other low-cost heat blocks, ambient temperature, self-regulating chemical reactions, and body heat [60,168,169] have been effective and demonstrate that the heating energy required for the RPA reaction does not require mains electricity. Additional work on lysis, fluid handling, reagent storage, heating, and amplicon containment is required to realize an integrated POC device suitable for commercialization.

This SARS-CoV-2 assay meets multiple characteristics for assay performance as set forth by the World Health Organization's COVID-19 Target Product Profile (TPP) for priority diagnostics to support response to the COVID-19 pandemic.[170] The TPP lists the desirable analytical test sensitivity to be equivalent to 10^4 genome copies per mL. We have demonstrated a duplexed assay with an analytical sensitivity of 50 copies per reaction. The TPP further lists desirable analytical specificity as the ability to detect all SARS-CoV-2 viral strains, not reacting with interferants, and not cross reacting with other common viral diseases that present with common signs and symptoms of COVID-19 like influenza A/B. Here, we have demonstrated that the assay detects both the delta and omicron variants while not cross reacting with other human coronaviruses nor influenza A or B. For interpretation of test results, the TPP lists visual manual readout in both the acceptable and desired categories which is achieved with our lateral flow readout mechanism. We have demonstrated this assay to be rapid with lateral flow results in 28 minutes from raw sample lysis to answer. The use of RPA also has inherent benefits as the lyophilized reaction pellets have been proven to be stable outside of cold chain storage for up to 12 weeks.[171]

To our knowledge, this assay is the first reported duplexed SARS-CoV-2 RPA assay for lateral flow strip detection format that incorporates an internal full process internal control that reports on the successful lysis, reverse transcription, and amplification of each RNA test reaction. It is also the first reported use of the RPA TwistAmp exo kits for both fluorescence and lateral flow detection formats opening the possibility for multiple assay readout options with a single kit, albeit with slight differences in assay performance. This utility of exo-based kits for LFA also enables convenient RPA assay design and optimization as primer and probe combinations can be tested with real-time readout instead of endpoint analysis.

3 Quantitative Point-of-care test for HIV

3.1 Introduction

HIV viral load testing serves a vital role in ending the HIV pandemic as these tests both diagnosis new HIV cases and are utilized to monitor existing cases. Many agencies have campaigns for regular HIV testing for at risk individuals. These campaigns push to identify new HIV cases, treat exiting cases, and monitor cases for HIV viral suppression. One such agency and campaign is UNAIDS with the 90-90-90 and updated 95-95-95 campaigns.[172] Routine viral load testing is crucial in monitoring the greater than 25 million people living with HIV and who are on ART. These routine tests are used for virological failure surveillance, cases where ART fails to suppress the virus to undetectable levels making transmission of the virus possible. Virological failure can be attributed to one or a combination of factors such as poor ART adherence, drug resistance, and drug interactions leading to reduced efficacy.[173] These routine tests also allow for clinical interventions to be made whether that be a change in course of the prescribed therapy, a change to second line drugs, or counseling to improve adherence.[174]

There is an estimated need for 60 million quantitative HIV viral load tests every year, primarily in low- and middle-income countries (LMIC). These countries have the highest burden of disease and have limited accessibility to central laboratory testing.[124] Current viral load monitoring efforts in LMICs require patients to travel to a clinic where blood samples are collected. These samples are then sent to a central laboratory for processing, causing delayed results often on the order of weeks. This delay in sample to answer leads to a loss of follow up as patients may not be contactable, delays in care for those who can be reached, and lack of interventions being provided at the time of care.[132] There are ongoing efforts to decentralize HIV viral load monitoring using next-generation POC tests performed in outpatient clinics. Decentralized testing aims to eliminate these roadblocks by allowing for quick sample to answer testing and providing same day interventions. Studies on POC viral load tests have shown that decentralized, clinic-based VL testing increases the number of ART patients with suppressed viral loads.[175] The WHO, NIH, and other public health institutions have funded initiatives to develop HIV viral load tests that can be applied in a wide range of settings such as well-resourced clinics and patients' homes.

While qualitative testing may suffice for some diagnostic applications, HIV viral load monitoring requires quantitative measurement of RNA concentration in blood to make appropriate clinical decisions. For patients receiving ART in the USA and Europe, the CDC and European AIDS Clinical Society (EACS) recommend an initial baseline quantitative viral load tests with subsequent routine testing.[176–178] Based on the result of the testing and monitoring, different therapies can be implemented as certain therapies are not recommended for high viral loads (500,000 cps/mL).[173,174,179] The WHO also recently updated

recommendations to treatment schedules for those who have undetectable viral loads, those with viral loads between 50 and 1,000 copies per mL, and those with viral loads greater than 1,000 copies per mL.[176] Further, the definition of viral suppression differs based on location as the EACS defines viral suppression as a vial load of less than 50 copies per mL whereas the CDC defines viral suppression as a vial load of less than 200 copies per mL. Both of these definitions are less than that of the WHO which defines viral suppression as less than 1,000 copies per mL.[176–178]

The current standard for viral load testing relies heavily on PCR and thermocyclers, leading to high costs and long processing times. This is due to the fact these tests are carried out in labs that use quantitative PCR (qPCR) or digital PCR (dPCR), both of which are limited to well-resourced central labs.[139] There are POC tests that leverage microfluidics for fluid manipulation and decreased run times, like the Abbott m-PIMA HIV-1/2 VL, Cepheid Xpert HIV-1 VL, and Molbio Truenat HIV-1.[132] However these platforms are still expensive ($5,000 to $20,000), take 55 to 90 minutes to run, and require reliable electricity as well as centrifugation for sample prep for plasma separation or process whole blood.[132] There is an urgent need for more affordable and faster quantitative HIV viral load testing methods that can be used outside of specialized labs.

3.1.1 Amplification Nucleation Site Analysis (ANSA)

The Posner research group (PRG) has developed a novel isothermal amplification method that leverages the viscous nature of RPA to produce discrete sites of DNA amplification that can be counted in a digital amplification strategy. This method retains the speed and simplicity of the RPA reaction with no additional instrumentation or preparatory steps like the aforementioned “SlipChips” and other digital amplification approaches. Additionally, this method utilizes simple porous membranes as support material for the RPA reaction, or it can be completed completely in the fluid phase, not requiring any support material. In contrast to other isothermal amplification methods, RPA employs viscous agents such as polyethylene glycol to boost enzymatic reaction efficiency,[163,171] which we believe limits the diffusion of amplified products, thereby creating isolated amplification sites.

3.1.2 Membrane-Based ANSA

Amplification Nucleation Site Analysis (ANSA) on a glass fiber membrane involves incorporating a typical RPA mixture into a porous membrane, warming it to around 40°C, capturing fluorescence images, and then counting the visible amplification sites, which directly relate to the initial nucleic acid concentration. This method is outlined in Figure 21. In a *Lab on a Chip* journal article that I co-authored, we studied the quantitative range of ANSA for DNA concentrations spanning multiple orders of magnitude. We established

that these nucleation sites can be accurately imaged and counted using an economical mobile phone-based fluorescence imaging setup and an Android application.[66] I wrote python code to run natively on android using the Chaquopy SDK which takes a time-resolved image stack, isolates the image from the 12.5-minute mark image, automates the counting of nucleation sites through processes like auto-cropping, filtering, binarization, and the Hough circle transform. Our initial findings show a clear relationship between the number of nucleation sites and the starting input DNA concentration, ranging from 50 to 3,000 copies per reaction covering approximately two logarithmic scales. At higher nucleic acid concentrations, exceeding 3,000 copies per reaction, the nucleation sites tend to cluster and overlap, posing a challenge for precise manual or algorithmic counting (Figure 23).

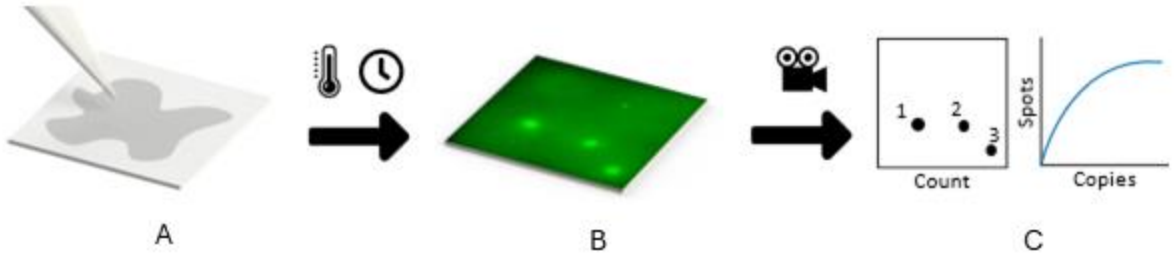

Figure 21. Paper-based ANSA Method. The RPA reaction is pipetted on to a glass fiber membrane (A). The membrane is heated and imaged (B). The images are analyzed for sites and correlated to initial input copy concentrations.

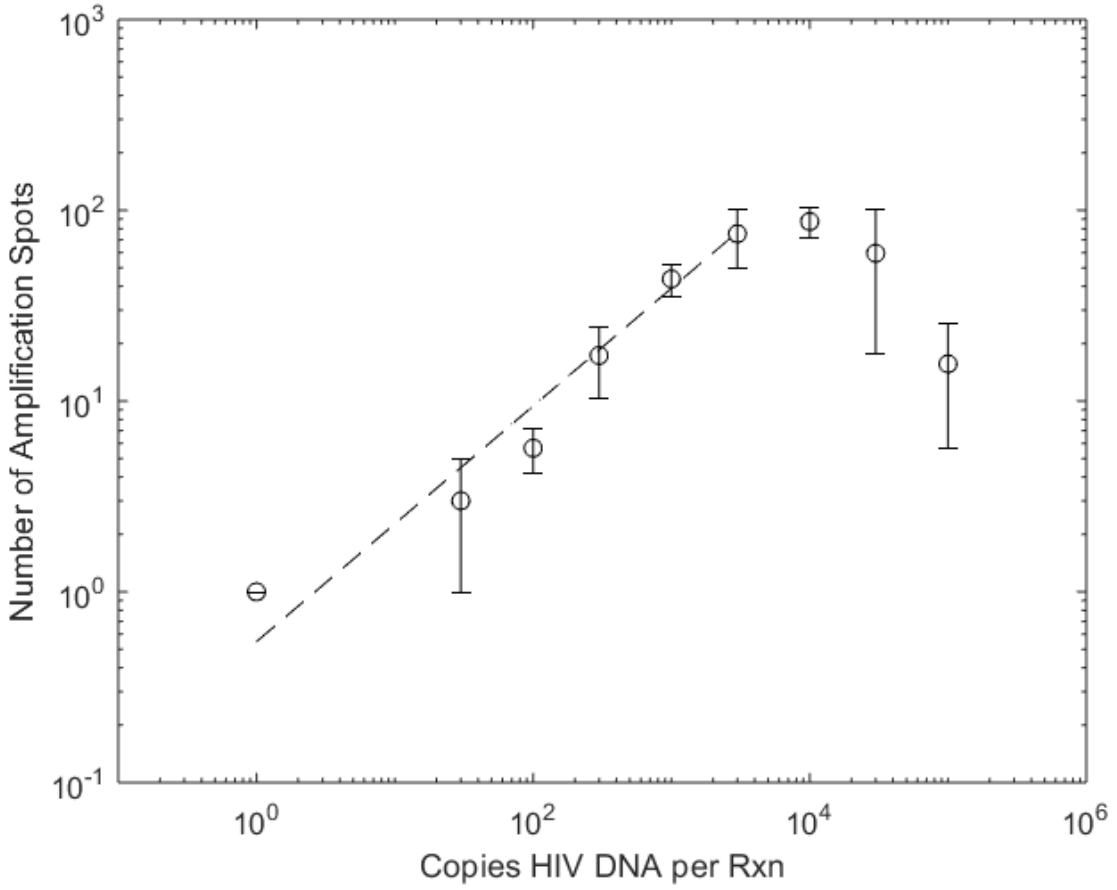

Figure 22. Initial ANSA quantitative correlation in a paper-based system. Data points represent the average and standard deviations (n = 3) for each target copy number tested and quantified. Dashed lines represent fitted models in all cases, we observe a strong relationship between nucleic acid input copy number and number of amplification nucleation sites. At high copy numbers (>10 000 cps rxn^{-1}), the number of measured nucleation sites decreases due to merging of amplification sites and inability of the experimental methodology to resolve and quantify the individual nucleation sites.

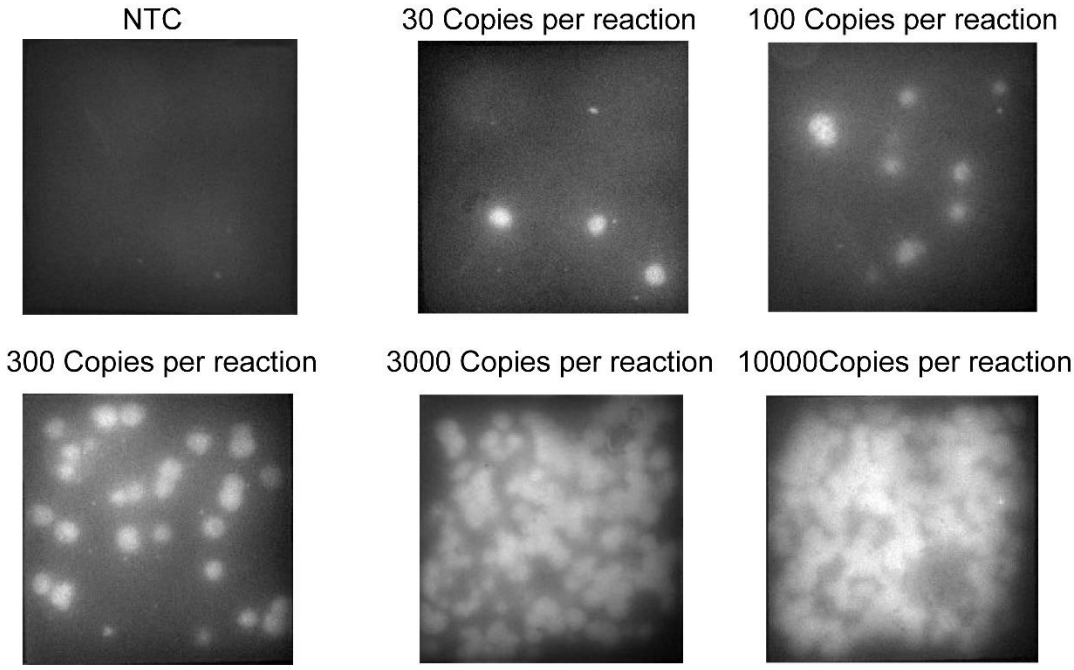

Figure 23. Site merging at high copy numbers. Images of RPA amplification of HIV-1 DNA on GF/DVA membrane captured using a microscope and mobile phone with copy number ranging from 30 to 100 000 cps rxn^{-1}. Images were recorded at t = 750 s. At lower copy numbers (30–3000 cps rxn^{-1}), we observe discrete amplification nucleation sites, with a positive relationship between number of nucleation sites and input copy number. At high copy numbers (10 000 and 100 000 cps rxn^{-1}), the nucleation sites are numerous, and they merge into a splotchy heterogenous fluorescence image, making it difficult to discriminate individual sites for viral load quantification.

3.1.3 Need For Increasing Dynamic Range of Membraned Based ANSA

Quantitative HIV viral load assays must be both analytically accurate and span at least 5 orders of magnitude to be clinically useful. Clinical guidelines in high resource settings mandate an initial viral load baseline measurement followed by routine monitoring. The CDC and EACS recommend against certain therapies when viral loads exceed 500,000 copies per mL.[177,180] Further, thresholds for "viral suppression" differ by setting: the EACS defines suppression as < 50 copies per mL, the CDC as < 200 copies per mL, whereas the WHO uses ≤ 1 000 copies per mL and now tailors treatment modifications to the < 50, 50–1000, and > 1000 copies per mL strata.[176] Sustained suppression below 1000 copies per mL markedly reduces transmission and underpins the UNAIDS 95-95-95 goals; more than 30 million people currently rely on routine viral-load testing to maintain effective ART worldwide. [181–183]

The same need for broad, precise quantification extends to other pathogens. Elevated high-risk human papillomavirus (HPV) loads predict progression to cervical neoplasia, improving triage precision in screening programs.[184] In hepatitis C management, baseline and on-treatment HCV RNA quantification confirm active infection and track direct-acting-antiviral efficacy.[185] Environmental qNAATs guide wastewater-based epidemiology by measuring viral decay and community prevalence.[82] Enhancing the accuracy and dynamic range of Amplification Nucleation-Site Analysis (ANSA) is therefore essential not only for point-of-care HIV viral-load testing but also for these emerging quantitative applications.

In its membrane-based format ANSA quantifies only 50–3 000 copies per reaction (Figure 22. Initial ANSA quantitative correlation in a paper-based system.), well below the 20–500 000 copies per mL range required for point-of-care HIV management. At high template concentrations amplification sites become crowded, merge, and dim, confounding automated counting. Further discussion on attempts to optimize membrane-based ANSA with imaging improvements and geometry improvements can be found in appendix section 6.2. To overcome this ceiling, I translated ANSA into a minimalist glass-slide microfluidic chip and systematically tuned polyethylene-glycol (PEG)–mediated phase separation of RPA mixtures to understand the growth of ANSA sites and tune the performance suitable for HIV quantification.

3.1.4 Microfluidic Chip-Based ANSA

Here I translate ANSA to a simple microfluidic chip to investigate the dynamics of ANSA and study the role of PEG in site formation and growth. I demonstrate RPA reactions performed between glass slides using a tailored reaction buffer with adjustable PEG concentrations. My results indicate that PEG concentration significantly influences both bulk fluorescence and peak fluorescence intensity of RPA reactions, where elevated PEG concentrations lead to decreased reaction efficiency as evidenced by lower fluorescence signals. Additionally, I observe a reduction in nucleation site diameter at higher PEG concentrations, which minimizes the occurrence of site merging. By utilizing high PEG concentrations, I successfully expand the quantitative range of ANSA to 4.7 orders of magnitude demonstrating ANSA's suitability for rapid, isothermal quantitative nucleic acid amplification assays within simple microfluidic chip. For further information on reducing bubble formation in the microchip, failed frame seal experiments, increasing the signal by increasing the relative probe ratio, and imaging artifacts and flow see appendix section 6.3.

3.2 Methods

3.2.1 Fabrication of Microfluidic Chip

RPA reactions are performed on glass slides in reaction chambers constructed by laminating both sides of polycarbonate (0.005", TAP Plastics, USA) with double-sided tape (9492MP-2-10, 3M, USA). The reaction chambers are first cut in the double sided tape using a flatbed cutter (FCX4000-50ES, Graphtec America, Inc., USA) to accommodate a 97 µL reaction volume. The geometry of the reaction chamber is detailed in Figure 24. Briefly, the chamber consists of an entry port (1.5 mm in diameter, 3.0 mm long) leading to a 19.6 mm diameter main reaction chamber with a 140° 4.0 mm vent port. The narrow inlet generates large capillary forces, while the wide vent port enables hydrophobic pinning to facilitate complete filling. For each glass slide, two reaction chambers are cut per sheet.

Polyethylene terephthalate glycol (PETG) coverslips are cut using a CO_2 laser (PLS6.150D, Universal Laser Systems, USA). We use PETG because it does not exhibit discoloration or increased autofluorescence upon laser cutting. In contrast, the laminated tape/polycarbonate/tape material demonstrates autofluorescence at the laser-cut interface, necessitating the use of a flatbed cutter. The design and schematics of the assembled chips are seen in Figure 24.

Prior to adhesion, 3 × 2 in. plain microscope slides (Premiere, C & A Scientific, USA) are cleaned with an acetone wash followed by an isopropyl alcohol wash to remove contaminants. Reaction chambers and coverslips are sealed onto the microscope slides and plasma treated for 5 minutes (PDC-001, Harrick Plasma, USA).

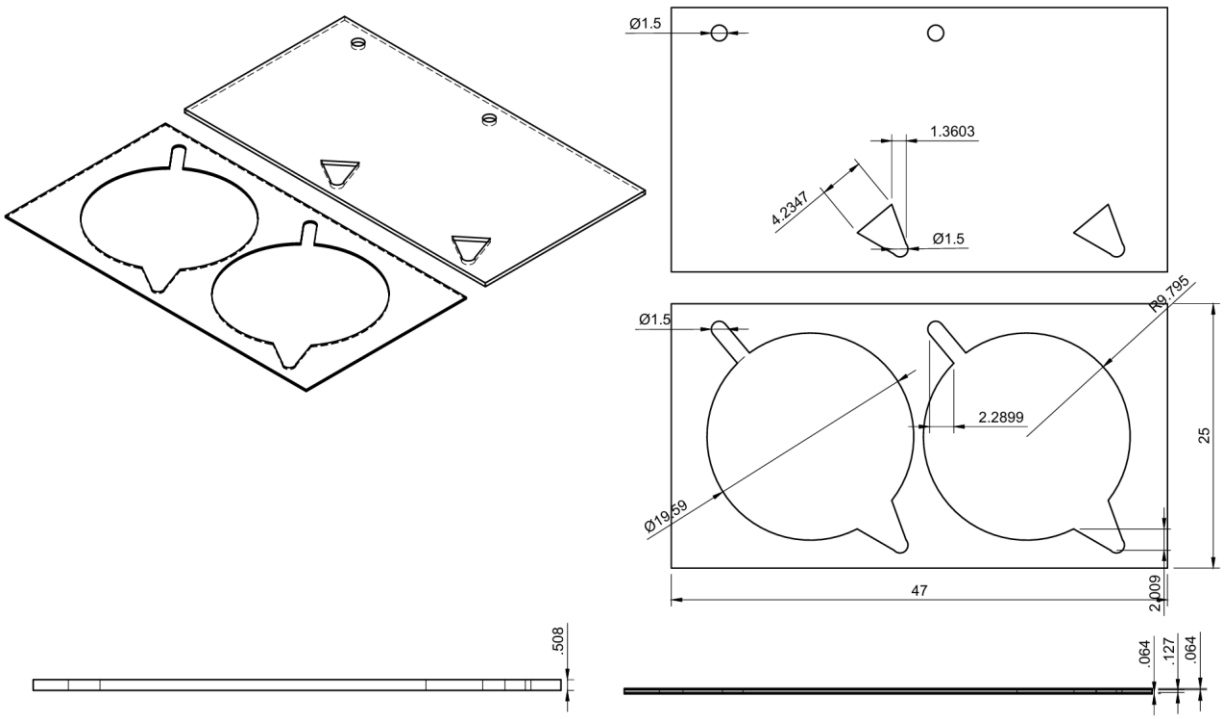

Figure 24. Layout and dimensions of the microfluidic chip for ANSA work.

3.2.2 RPA Conditions

We prepare a custom RPA buffer consisting of 70 mM Tris (77-86-1, Sigma Aldrich, USA), 35 mM HCl (7647-01-0, Sigma Aldrich, USA), and 200 mM KOAc (127-08-2, Sigma Aldrich, USA). A 20% (w/v) PEG 35K (25322-68-3, Sigma Aldrich, USA) solution is prepared by vortexing. PEG is added to the custom buffer at volumes required to achieve the desired final concentration.

In RPA experiments, we target synthetic DNA of the HIV-1 genome (group M, subtype A) (gBlocks Gene Fragments, Integrated DNA Technologies, USA). Primers and probes are used as described by Lillis et al.[71]

The amplification mastermix consists of two TwistAmp exo kit lyophilized pellets (TwistDx, GBR) that are combined into a single tube, 73.8 µL custom rehydration buffer, variable volume of 20% PEG solution, 540 nM forward and reverse primers (Integrated DNA Technologies, USA), and 120 nM sequence-specific probe that is compatible with exonuclease III cleavage (LGC Biosearch Technologies, GBR). The mastermix of custom rehydration buffer, primers, and probe is added to the lyophilized exo-kit RPA pellets, rehydrating them. The target DNA is then added and the mixture is inverted five time to allow for mixing. The tube is re-opened and 14 mM MgOAc is pipetted onto the tube cap bring the total reaction volume to 100 µL. The tube is left open under vacuum for 30 seconds to remove bubbles, then closed and centrifuged for ~30 seconds to initiate the reaction and ensure homogeneous distribution of reactants. The 97 µL

reaction volume is then immediately pipetted into the entry port of the glass chip. The reaction volume is undersized to account for pipetting loses and to reduce the addition of air bubbles during the blow step of pipetting.

For tube-based experiments, tubes are placed into a T16-ISO instrument (Axxin, USA), incubated at 39 °C, and fluorescence is recorded for 20 minutes, with a manual mixing step at 4 minutes.

3.2.3 Loading of Microfluidic Chip

A 100 µL RPA reaction (mastermix and target) is pipetted into the inlet chamber. The inlet and outlet chambers are then backfilled with mineral oil (8042-47-5, Sigma Aldrich, USA) before being sealed with PCR tape (TempPlate RT Select Optical Film, USA Scientific, USA) to prevent contamination via aerosolized amplification products. The sealed glass chip is placed on a resistive heater (53-421235, TurboFlex, USA) covered with a 0.06" anodized black aluminum plate and backed with 3" Styrofoam, set to 39 °C using an external temperature controller with a thermistor attached to the heating surface as detailed in Figure 25. ANSA Imaging Set-up. The reaction is imaged for 15 minutes, after which the glass chip is sealed in a plastic bag and disposed of. The experimental process is shown in Figure 26.

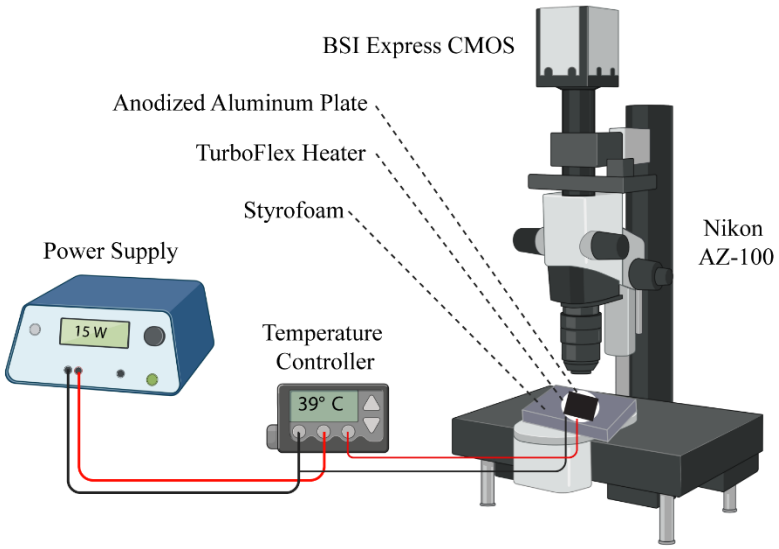

Figure 25. ANSA Imaging Set-up.

3.2.4 Imaging and Data Analysis

Epifluorescence microscopy using an upright multi-zoom microscope (AZ100, Nikon, JPN) with 0.5× objective, filter cube set for green fluorophores (FITC-5050A, Semrock Optical, USA), white light excitation source (X-Cite exacte, Excelitas Technologies, USA) imaged the evolution of RPA nucleation

sites in the glass chip. The 0.5× objective has a 43 mm field of view diameter. Grayscale images were captured every 5 seconds for 15 minutes using a back-illuminated CMOS camera (Prime BSI Express, Teledyne Photometrics, USA).

I process the images to extract nucleation site counts and determine the initial DNA input copies (Python 3.9.21, Python Software Foundation). First, Gaussian blurring with a 7x7 kernel size is applied to each frame to minimize pixel-level noise. Temporal background subtraction is performed using a rolling-ball filter with a 3-frame window, which computes the average of the preceding, current, and succeeding frames to suppress temporal background fluctuations. A global background subtraction is then applied across all frames, normalizing the image background to zero by averaging the first 25 frames, which removes bright imperfections or artifacts from the glass reaction chips. A circular mask is applied to each frame to isolate the central region of interest and exclude peripheral areas that are not the reaction chamber of the chip, further minimizing edge-induced artifacts and bubbles. Following the preprocessing steps, an algorithm applies a local-maximum detection procedure (*peak_local_max*, scikit-image v0.24.0)[186] to identify discrete fluorescent nucleation sites in each frame. The algorithm outputs the maximum number of sites detected and number of sites detected at 7.5 minutes.

For single puncta analysis across varying PEG concentrations the same process as outlined above is followed. All nucleation sites identified using the local-maximum detection procedure are then fit using a two-dimensional Gaussian function (curve_fit, SciPy v1.12.0). Puncta whose eccentricity, calculated as the ratio of sigma_x to sigma_y (sigma_x/sigma_y), is between 0.95 and 1.05, indicating near-perfect circularity are then saved individually as separate images with a 40 pixel buffer in all directions from the identified peak, ensuring complete imaging of the puncta in later frames and including only circular non-overlapping puncta are included in further analysis.

I process the images to extract gaussian fit parameters and determine the growth kinetics. I start by fitting a two-dimensional Gaussian function (curve_fit, SciPy v1.12.0) to each individual puncta image derived from above and save the parameters of amplitude, standard deviations (sigma_x, sigma_y), and fit quality (R^2). The gaussian radius (sigma) values are averaged. I analytically calculate the area under the Gaussian curve (AUC), representing integrated fluorescence, from amplitude and sigma values. Data across puncta are consolidated into condition-specific CSV files.

Subsequent filtering criteria include removing frames with a rolling average intensity below 50 and discarding puncta whose maximum intensity does not exceed four times the minimum intensity, ensuring a minimum brightness increase consistent with puncta growth in order to remove bubbles or dust that do not exhibit increasing brightness as expected from the puncta. Frames preceding stabilization of the

Gaussian fit, identified by consistent stability in rolling mean and standard deviation within a tolerance of 1, are also discarded, with typical stabilization after frame 70 to remove errant gaussian fitting parameters. Entire puncta are discarded if the diameter (sigma) exceeds 18 pixels, a threshold chosen based on empirical observations indicating that sites with sigma greater than 18 had typically merged.

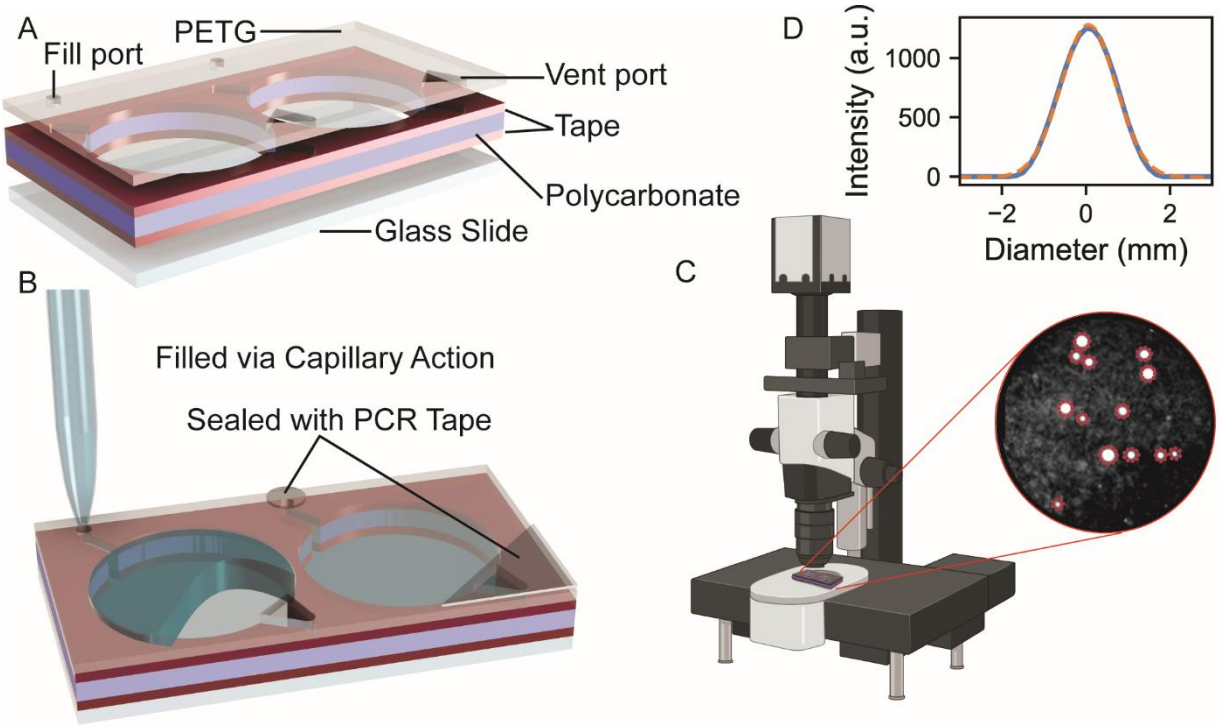

Figure 26. The chip-based ANSA procedure. The illustrated process depicts the steps involved in chip-based amplification nucleation site analysis. (A) Reaction chips are made using laser cut PETG top plates, digitally cut double-sided tape (red layers) laminated polycarbonate (blue layer) intermediate spacers, and a glass slide bottom plate. (B) RPA reaction mastermix and target DNA are dispensed into the chips using the inlet port. The narrow inlet and hydrophilic treated materials allow for capillary filling while the exit port expansion allow for a stop valve to allow for complete filling. The inlet and outlet are backfilled with mineral oil and covered with PCR tape. (C) The reactions are heated to 39 °C and imaged for 15 minutes using fluorescence microscopy. Discrete amplification sites form (shown as white dots) within the reaction volume. (D) Amplification sites with Gaussian intensity profiles are analyzed (blue solid line) for site formation and fitted with a gaussian (orange dashed line). A gaussian fit enables the extraction of site width, peak intensity, and area under the curve.

3.3 Results and Discussion

This work presents a detailed investigation into the growth dynamics of discrete RPA reactions in free solution contained in a shallow microfluidic chip. In the previous membrane based ANSA report, we

observed discrete amplification sites in RPA reactions conducted within a porous membrane, and I hypothesized that the viscous nature of the RPA reaction buffer combined with the microscale structure of the porous membrane suppressed convective and diffusive transport, leading to the formation of isolated amplification sites.[66] Here, I translate ANSA to a membrane-free microfluidic environment, employing a custom buffer formulation with varying PEG concentration. As noted in both the original RPA publication and associated patent literature, PEG is an essential component for enabling recombinase loading and strand invasion; in its absence, little to no nucleic acid amplification is observed. [163,187] I hypothesize that varying PEG concentration will impact reaction kinetics of RPA as well as the growth and diffusion of RPA amplification reactants and products in individual reactions sites.

Figure 27 shows representative fluorescence micrographs for RPA reactions in a shallow microfluidic chip for PEG concentrations of 1%, 4%, 8%, and 10%. As the PEG concentration increases the size and intensity of the sites decreases. The size of the spots appear to be similar for the 1% and 4% PEG concentrations although the 4% begins to show a few sites that appear smaller. The 8% and 10% PEG concentrations show smaller sites and the 10% also shows fewer sites compared to the other concentrations.

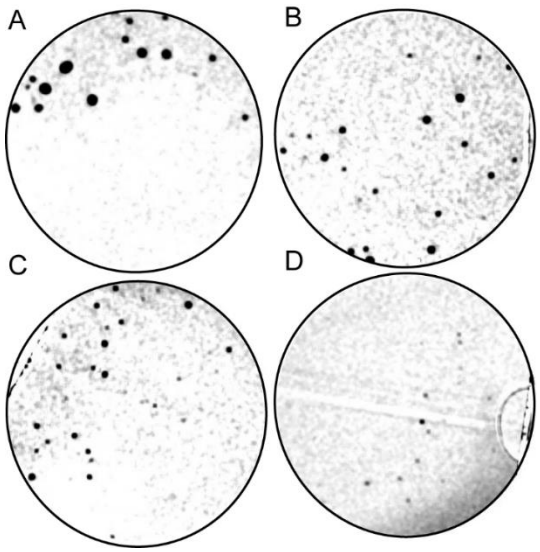

Figure 27. Fluorescence micrographs of ANSA reactions. Images are inverted to show RPA reaction sites in black. The black circle denotes the boundary of the reaction chamber. Representative images shown at 7.5-minute incubation times for (A) 1%, (B) 4%, (C) 8%, and (D) 10% PEG concentrations. Note that the reaction site diameter decreases with increasing PEG concentration.

I observe the growth of individual ANSA sites within the reaction chambers and monitor the reactions via fluorescence generated by the hydrolysis of the RPA probe. Figure 28A shows the fluorescence intensity of a single RPA reaction site from 8 to 26 minutes. The distribution of the fluorescence intensity is Gaussian

and grows in intensity and width with time. I hypothesize that the emergence of this shape results from localized amplification reactions at the site, where fluorescent products diffuse outward while reactants including uncleaved probe, primers, dNTPs, recombinases, single-stranded binding proteins, creatine, and creatine kinases diffuse inward. At 6.5 minutes, the amplification spot becomes visible and is only 210 microns in diameter. At 15 minutes, the spot reaches 530 microns. At 17.25 minutes the spot is 610 microns, after this time, there is no further increases in intensity.

I fit Gaussian distributions to the intensity profiles and extract under the normalized area under the curve (AUC) and the distribution width (*i.e.,* site diameter), represented by the Gaussian two sigma. Figure 28B shows the spot diameter, normalized AUC, and normalized fluorescence as a function of time. In Figure 28B the AUC and fluorescence are normalized by their respective maxima. The site diameter steadily increases linearly ($R^2 = 0.99$) until 17.25 min after which the growth rate slows to an apparent asymptote near 800 microns. The maximum normalized intensity increases exponentially, similar to a RPA amplification curve from 5.66 to 17.25 minutes, where it reaches a maximum and decreases. The AUC follows a similar trend, peaking shortly after the fluorescence intensity reaches maximum and then decreases.

The black line in Figure 28B focuses on the site diameter as a function of time after the 17.25-minute mark, where fluorescence reaches its peak, and estimates the site diameter to as the estimated diffusion distance of the FAM fluorophore. I calculate the diffusion coefficient for FAM based on its reported diffusion coefficient at 25 °C in water[188] and adjust it based on the viscosity of a 3% PEG 35,000 solution at 40 °C.[189] Using this corrected value, I observe strong agreement with a pure diffusion model ($R^2 = 0.88$).

The initial phase of site growth is dominated by exponential amplification of the reaction, leading to rapid fluorescence increase. As the available reactants are consumed the reaction slows and diffusion becomes the primary driver of site expansion. Although fluorescence intensity begins to decline, the site diameter continues to increase in a manner consistent with diffusion from a point source. The AUC supports this interpretation, remaining constant for a period after the fluorescence peak before gradually decreasing. This decline likely results from photobleaching of the fluorophore over the 30-minute experiment, during which it is continuously excited, or from the signal dropping below the detection threshold.

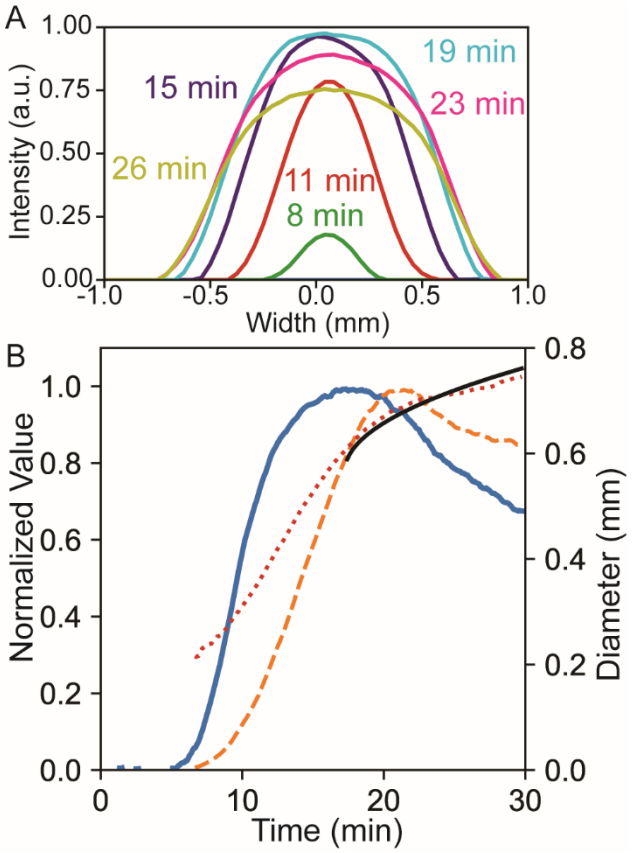

Figure 28. Single site growth over a 30-minute reaction time. (A) The gaussian profile for a site over time. Each wider line shows the site intensity increasing with time. The intensity and width of the distribution increases with time. (B) The measured diameter (dotted red line), the normalized integrated Area Under the Curve (AUC, dashed orange line), the normalized fluorescence (solid blue line), and the simulated pure diffusion fit of carboxyl fluorescein after the maximum intensity of the reaction has been reached (solid black line) are plotted for a site over time. The AUC and fluorescence are normalized by their respective maximums.

I found that PEG concentration impacts the endpoint reaction product generation. Figure 29A shows the bulk in-tube fluorescence intensity as a function of PEG concentration. At PEG concentrations below 1%, fluorescence intensity remains low, followed by a gradual increase and a peak between 2.5–3.5%, consistent with the performance of the commercial buffer. Beyond 4%, a sharp decline in fluorescence is observed. This data shows that in tube-based bulk reactions with our custom buffer the optimum PEG concentration for maximum fluorescence output is found between 1.5% and 3.5% PEG. Figure 29B shows the endpoint diameter of spots for varying concentrations of PEG. Across a PEG concentration range of 1–3.5%, I observe consistent end-point diameters; however, concentrations ≥5% PEG result in a sharp reduction in

site diameter. This threshold behavior may be attributed to several factors, including steric hindrance that inhibits or slows recombinase and polymerase activity; the promotion of non-specific secondary structures; hindered strand separation required for D-loop formation; altered DNA hybridization and melting dynamics; impaired diffusion of reactants; and reduced frequency of molecular collisions necessary for efficient amplification. The most likely contributor to the observed loss in performance is the formation of an aqueous two-phase system (ATPS). PEG is commonly used to induce liquid-liquid phase separation for protein purification and concentration via precipitation. [190,191] Studies using PEG 6000 have demonstrated phase separation at concentrations between 7–10%, resulting in the formation of protein-rich phases,[192] while PEG 35000 has been shown to induce phase separation between 4–10% depending on the presence and concentration of sodium and potassium salts.[193] In our system, the combination of monovalent (potassium) and divalent (magnesium) salts in the buffer may shift the threshold for phase separation to lower PEG concentrations. I propose that this ATPS partitions reaction components into PEG-rich and salt-rich phases, concentrating and aggregating some proteins in one domain while excluding them from the DNA-containing phase. This separation may also generate inhomogeneous microenvironments—such as shifts in pH or enzyme hydration—that contribute to enzyme denaturation and further reduction in RPA efficiency.

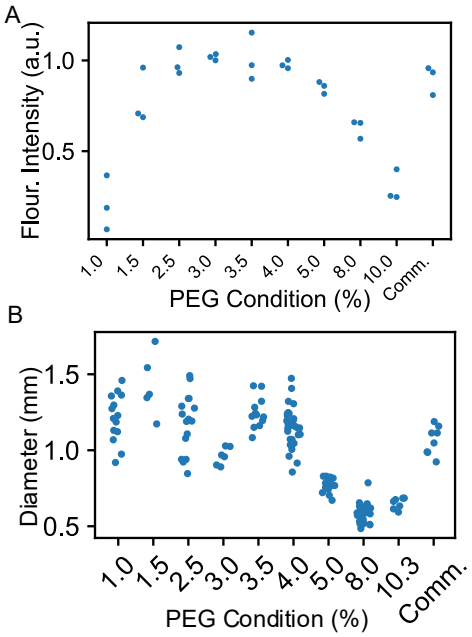

Figure 29. Endpoint conditions for tube and chip-based experiments. (A) Endpoint bulk fluorescence intensity of RPA reactions performed in tubes, measured using the Axxin T-16 after a 15-minute reaction. The normalization is set based on the average commercial buffer intensity. (B) Swarm plot of endpoint individual amplification reaction spot diameters at 15-minutes as a function of reaction

Figure 30 shows the diameter of individual reaction spots as a function of time for (A) 1%, (B) 2.5%, (C) 5%, (D) 8%. This data shows that the diameter increases approximately linearly during this phase. I hypothesize that fluorescent products are initially generated at the center of the amplification site and subsequently diffuse outward, where they serve as templates for further amplification, creating a moving reaction front. Over time, the central region becomes depleted of reactants, causing product generation to stagnate locally. Modeling this behavior is challenging due to the presence of a time-dependent, nonlinear signal generation term in addition to passive diffusion, which dominates site expansion at later time points. This data shows that site growth is faster at low PEG concentrations, where reactants and products can diffuse at higher rates, and slower at high PEG concentrations, where diffusion becomes increasingly restricted.

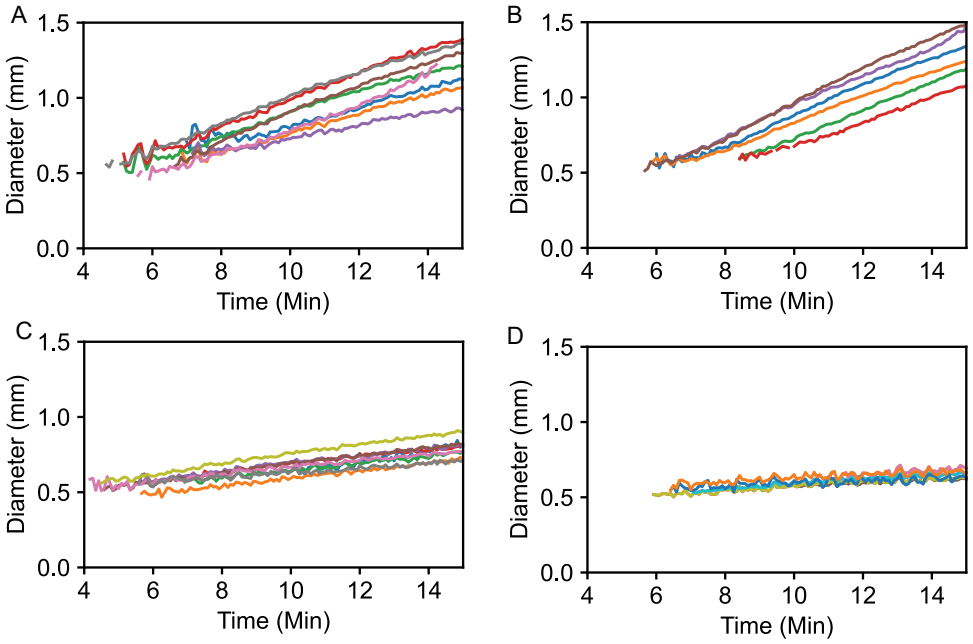

Figure 30. Width of individual reactions spots as a function of time with varying mastermix PEG concentration. Representative site diameters over time for (A) 1%, (B) 2.5%, (C) 5%, and (D) 8% PEG.

One of the primary motivations of this work is increase the upper limit of quantification (ULOQ) of ANSA. In previous work on membranes I demonstrated a dynamic range of 67–3,000 copies per reaction with a steep drop off above 3,000 copies due to sites merging and overlapping.[66] I hypothesized that increasing the projected area and making reaction spots smaller would enable larger ULOQ because it would result in a larger number of nonoverlapping reaction spots that can reliably identified and counted. Figure 31 shows

the number of nucleation sites as a function of the number of HIV-1 nucleic acid copies per reaction for PEG concentration to 8% conducted in the shallow microfluidic reaction chamber. The data exhibit a power-law (log–linear) relationship between the number of amplification nucleation sites and the input target copies across the tested range of 20 to 100,000,000 copies per reaction. All experiments were performed in at least triplicate, consistently showed positive amplification, and no amplification was observed in no-template controls (NTCs). Consistent with our previous report on ANSA, the number of amplification nucleation sites follows the relationship $y=mx^b$. Here I find our fit parameters to be $b = 23.904$ and $m = 0.310$. This model fits well up to ~10,000 copies per reaction, beyond which site counts become increasingly variable, though without the steep drop-off I previously observed.

I hypothesize that the increased variability at high target concentrations (above ~500 site counts) arises from limitations in image resolution and pixel availability in our current imaging setup. Each 1 mm corresponds to 24 pixels, and the resulting image stacks are 450 × 450 pixels, corresponding to an imageable area of 18.75 × 18.75 mm, or approximately 301.41 mm². Given that the average puncta diameter at 7.5 minutes is 0.598 ± 0.0468 mm, the theoretical maximum count is approximately 1,253 puncta (assuming perfect packing). Accounting for realistic spatial stacking constraints (30–60%), the effective maximum count ranges from 373 to 752 puncta.

Consistent with this estimate, I observe increased variability and eventual undercounting as the number of sites approaches 500 which can mask clinically significant high-titer samples. This suggests that a critical packing density has been reached, beyond which amplification spots begin to overlap or blur due to the finite spatial and optical resolution. The reaction chamber has 162,968 total pixels, and as spot density increases, the available pixel area per spot decreases, compounding the challenge of discrete site identification. Thus, undercounting at high concentrations likely reflects a saturation of the system's imaging capacity rather than a true plateau in amplification efficiency. Further improvements in spatial resolution and chamber design could help alleviate these limitations and extend the measurable dynamic range.

It is important to note that the current spot-counting approach relies on data from a single timepoint, typically capturing amplification nucleation at a fixed endpoint. However, other groups have explored real-time or kinetic-based quantification strategies for RPA, such as determining the time to threshold (Tt) of fluorescence intensity with poor results.[194,195] Incorporating temporal information could significantly enhance quantification accuracy and robustness, especially at higher target concentrations where static analysis becomes more error-prone. In the future, leveraging additional timepoints or continuous imaging could provide a richer dataset for analysis. Furthermore, advanced computational tools such as machine

learning may offer powerful means to extract quantitative insights from complex amplification dynamics, enabling improved performance in high-density imaging conditions.

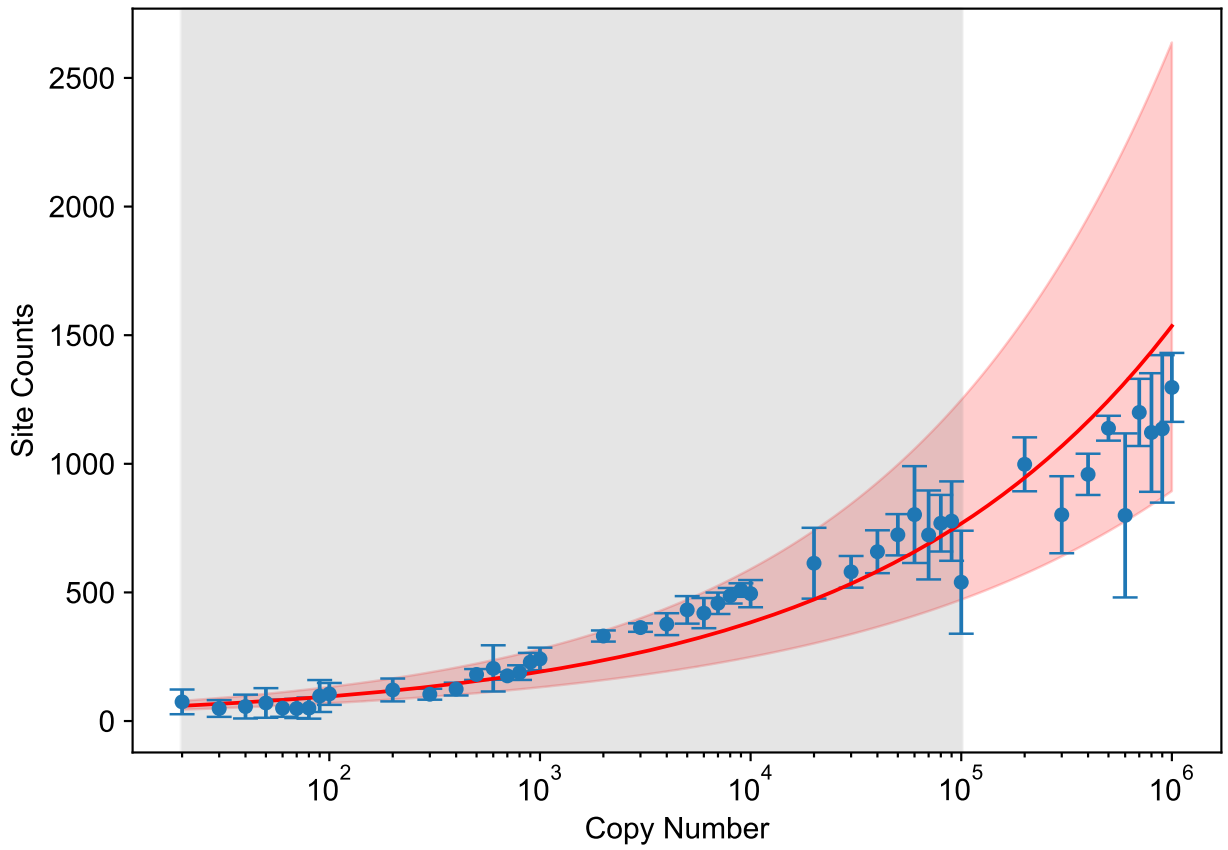

Figure 31. Microchip range quantifying DNA with Spot counts in microchips. Blue points show the mean and standard deviation (n=3) of ANSA counts at concentrations on a log scale. Red solid line show a power law regression on the range [20,100000]. Red shading shows a 95% confidence interval (α=0.05). Grey shading is the clinical diagnostic range of HIV.

4 Quantification Of HIV-1 DNA Isothermal Amplification Images Using Convolutional Neural Networks

4.1 Introduction

Determining HIV viral load across a clinically relevant 5-$\log_{10}$ copy span is essential for treatment selection, resistance monitoring, and transmission control. Isothermal Amplification Nucleation-Site Analysis (ANSA) offers a low-cost, chip-based alternative to qPCR, but its quantitative range is limited. At high target concentrations, puncta merge and begin to occupy >40% of the imageable area, making accurate counting unreliable.

Physical and chemical chip modifications described in the previous chapter delayed site coalescence but did not extend the upper limit of quantification (ULOQ) to meet clinical needs (Figure 31). These earlier methods also relied on a single time point, ignoring the rich spatial and temporal fluorescence information captured during the reaction.

Convolutional neural networks (CNNs) have shown strong performance in image-based regression and classification tasks. [196] I have previously developed CNN models for similar datasets, and preliminary results showed that 2D fluorescence images at single time points could be analyzed using a CNN architecture.[197,198] Residual Networks (ResNets), in particular, are well-suited to extracting spatio-temporal features from image sequences and have demonstrated robust performance in medical imaging by mimicking layered visual processing.[199] I hypothesized that a ResNet trained on selected time points from ANSA image sequences could accurately discriminate input DNA concentrations, even in conditions where conventional site counting fails.

Here, I present a ResNet-18-based pipeline that classifies HIV DNA using two models: one based on clinically relevant viral load thresholds and another spanning five orders of magnitude. Seven frames were selected from 15-minute fluorescence movies, capturing baseline, growth, and plateau phases. Reactions included 20–10^6 copies, as well as non-template controls. The model achieved 94.6% accuracy across clinical categories and >92% accuracy in single-log bins, outperforming the site-counting baseline. These results demonstrate that deep learning can extend ANSA's dynamic range to meet clinical requirements without additional hardware, unlocking the full potential of time-resolved isothermal amplification assays.

4.2 Methods

4.2.1 Overview of ANSA Image Analysis via ResNet Model

Figure 32 demonstrates the ResNet model analysis pathway. 15-minute-long ANSA reactions with images taken every 5 seconds are taken on microfluidic chips as described in Section 0 over the range of 20-10^6 copies per reaction. Non template controls are also collected in the same manner by replacing the template addition step with sterile nuclease free water. Frames of interest used as input channels in the ResNet model architecture for training. Frame selection, model selection, and hyperparameter tuning are detailed below. The trained model is then evaluated using a validation dataset.

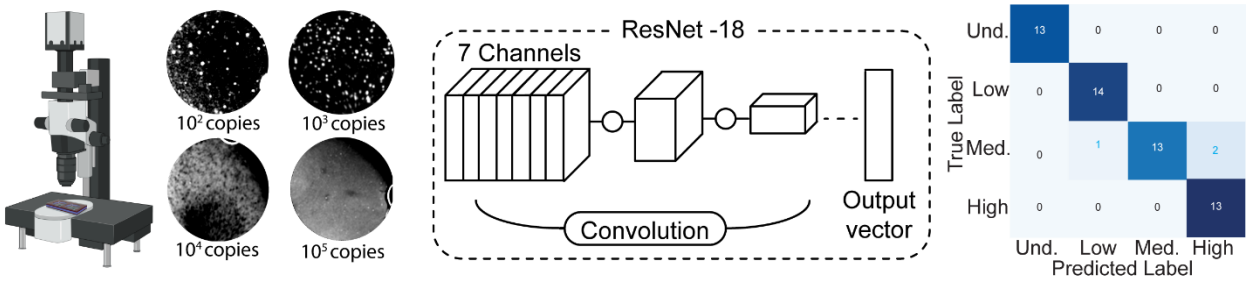

Figure 32. ANSA process for ResNets. Time-resolved fluorescence microscopy images were acquired every 5 seconds over a 15-minute period (B) Images were preprocessed with background subtraction and resized to 500x500px. Seven key time points were selected and fed into a ResNet model. The image shown corresponds to 100,000 DNA copies. (C) The ResNet processes image sequences through layered convolutions, extracting features and classifying HIV viral loads. (D) The model was evaluated for accuracy on four clinical viral load categories and across a 5-log DNA concentration range.

4.2.2 Selection of Time Points for Model Input

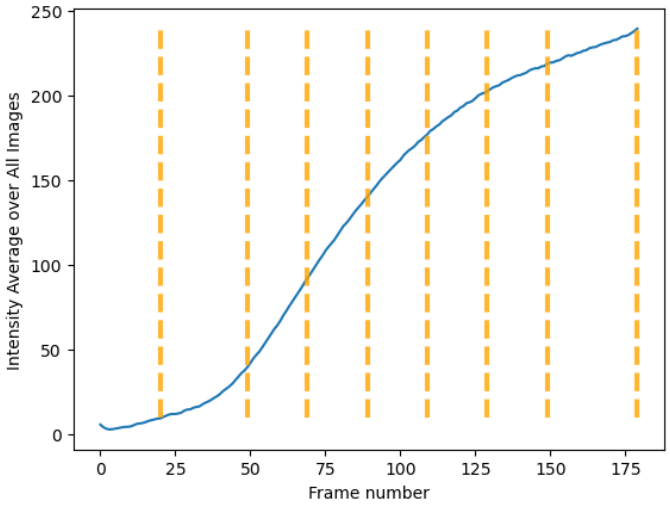

Figure 33. Temporal dynamics of average fluorescence intensity during an RPA reaction**.** The blue line represents the average pixel intensity across all image frames over time, illustrating a sigmoidal growth pattern consistent with tube-based RPA fluorescence kinetics. Orange dashed lines denote selected time points used for input channels in ResNet.

Figure 33 shows the average frame intensity across all images for all frames imaged and the selected frames used for the input channels in the ResNet. The resulting curve (blue line) of the frame average intensities exhibits a sigmoidal profile, characteristic of amplification-based fluorescence reactions, with an initial lag, exponential signal growth, and plateau phase. To capture representative points along this progression, seven key frames were selected. The first time point was defined as an average of the first 20 frames to establish a background baseline. The following frames were selected: frame 49 (4:05 min, early growth in high concentrations), frame 69 (5:45 min, early growth in low concentrations), frame 89 (7:25 min, midpoint of the reaction), frame 109 (9:05 min, early plateau phase), frame 129 (10:45 min, mid-plateau phase), frame 149 (12:25 min, late plateau phase), and frame 179 (15:00 min, end of reaction). These points were marked with vertical orange dashed lines on the intensity plot and were used to define biologically relevant fluorescence phases for input into the ResNet model.

4.2.3 Image Preprocessing and Dataset Preparation

All fluorescence image stacks were sourced from an organized directory containing processed .tif files. Each stack was loaded using scikit-image (v0.24.0)[186], converted into a PyTorch tensor, and resampled via bicubic interpolation to a uniform spatial resolution of 500 × 500 pixels across all frames. During this

process, a channel dimension was added to maintain a consistent tensor shape of (1, 180, 500, 500). Each tensor was then saved individually in .pt format.

After preprocessing, the dataset was randomly shuffled and partitioned into training (60%), testing (20%), and validation (20%) subsets as seen in Table 4 and Table 5. To facilitate categorical classification, each tensor was assigned to an input DNA concentration class based on its associated label. The categorization thresholds for the clinical model were defined as: "undetectable" (<200 copies), "low" (200–1,000 copies), "medium" (1,000–10,000 copies), and "high" (>10,000 copies). The categorization thresholds for the logarithmic-scale model were defined as: "undetectable" (<100 copies), "low" (100–1,000 copies), "medium" (1,000–10,000 copies), "high" (10,000–100,000 copies), and "very high" (>100,000 copies).

Table 4. Logarithmic scale model (Train/Test/Validation) split

	10^1	10^2	10^3	10^4	10^5
Split	44/13/13	30/14/14	26/13/14	32/11/8	28/7/7

Table 5. Clinical utility model (Train/Test/Validation) split

	Undetectable	Low	Medium	High
Split	45/14/13	29/13/14	26/13/14	60/18/15

Tensors were then organized into corresponding category-specific folders within each dataset split, ensuring class balance across training, validation, and testing sets.

4.2.4 Model Architecture and Training

A modified ResNet18 architecture was used for classification tasks. The first convolutional layer was adjusted to accept seven input channels (corresponding to the seven selected frames) rather than the default three. The fully connected classification head was replaced with a sequential module consisting of a dropout layer followed by a linear layer to output five input DNA concentration classes. Training was performed using a CUDA-enabled GPU. Data were loaded into memory using custom PyTorch Dataset and DataLoader classes with a batch size of 32. To address class imbalance, a weighted random sampler was implemented based on inverse class frequency. Models were trained using two different objective schemes: one corresponding to clinical utility thresholds ("Clinical Utility Model") and another corresponding to

logarithmic thresholds ("Logarithmic Model"). Separate hyperparameter optimization was performed for each model, and final architecture was selected independently. Performance metrics including training loss, validation loss, and classification accuracy were recorded at each epoch. Final model performance was assessed on the held-out test set, and a confusion matrix was generated to visualize classification performance.

4.2.5 Hyperparameter Optimization

Hyperparameter tuning was performed using OPTUNA[200] with Bayesian optimization. The search space included model depth (ResNet18 or ResNet34), learning rate, weight decay, dropout rate, scheduler gamma value, and optimizer type (Adam, SGD, ASGD, LBFGS). The optimization objective was to minimize the negative validation accuracy across 25 epochs, using a median pruning strategy to terminate underperforming trials early.

Initially, model startup used random weight initialization, which introduced substantial variability in validation performance across identical hyperparameter sets. To address this, an early version of the OPTUNA optimization loop was implemented in which each sampled hyperparameter set was retrained multiple times, and only the best-performing trial per hyperparameter set was retained before sampling new hyperparameters. While this approach improved robustness to random initialization effects, it proved computationally inefficient and significantly slowed convergence.

Consequently, the final optimization strategy adopted a pruning and resampling approach. Trials were evaluated at intermediate epochs, and poorly performing configurations were terminated early. This strategy converged toward similar optimal hyperparameters as the original retrain-and-select approach but achieved convergence faster, albeit requiring a greater total number of trials. A total of 200 OPTUNA trials were conducted to identify the final hyperparameter set used for model training.

4.3 Results

Here I demonstrate that ResNets are capable of producing quantification classification over two different levels of classification. The first classification is semiquantitative and separates the data into four classes that are significant to the clinical decision-making process for HIV viral load testing. The second classification is also semiquantitative with five classes that represent the 5-$\log_{10}$ copy span of the dataset. To this end, two separate models were developed: the Clinical Utility Model and the Logarithmic Model. While both models shared the same base architecture (ResNet-18) and were trained for 25 epochs, they

were optimized independently using distinct hyperparameter configurations as in Table 6. This demonstrates the ability of ResNets to make semiquantitative classifications over four or five classes.

Table 6 Summary of hyperparameters.

Hyperparameter	Clinical Utility Model	Logarithmic Model
Model Depth	18	18
Learning Rate	0.00388	0.000107
Weight Decay	1.93×10^{-4}	2.37×10^{-6}
Dropout Rate	0.243	0.496
Gamma Rate	0.939	0.940
Optimizer	SGD	Adam
Epochs	25	25

The Clinical Utility Model employed the SGD optimizer with a relatively high learning rate (0.00388), moderate weight decay (1.93×10^{-4}), and a dropout rate of 0.243. In contrast, the Logarithmic Model used the Adam optimizer, with a substantially lower learning rate (1.07×10^{-4}), lighter regularization (2.37×10^{-6} weight decay), and a higher dropout rate of 0.496. Both models used exponential learning rate decay with similar gamma values (~0.94). These differences reflect the varying complexity and generalization needs of their respective output distributions.

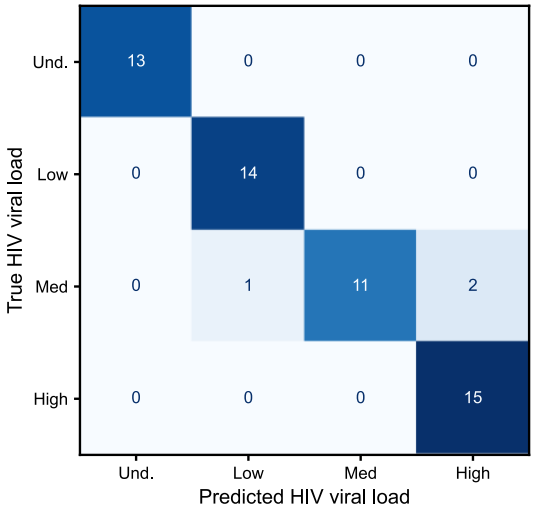

Figure 34. Clinical utility confusion matrix. The matrix displays predictions across four categories, with color intensity reflecting classification frequency. Diagonal entries represent correct predictions.

The Clinical Utility Model achieved an overall classification accuracy of 94.6% across four response categories: Undetermined (Und.), Low, Medium (Med), and High. Figure 34 shows the model demonstrated perfect sensitivity (100%) for the Und., Low, and High categories, correctly identifying all instances within those groups. The Medium category exhibited slightly reduced sensitivity (78.6%), with misclassifications primarily into the adjacent Low (one instance) and High (two instances) classes. Overall, the model showed strong discriminative capability, with minimal confusion among non-adjacent categories.

The Logarithmic Model achieved 92.7 % classification accuracy across five logarithmically spaced output categories, covering input DNA concentrations from 10^1 to 10^5 copies. Figure 35 (log-scale confusion matrix) shows perfect sensitivity (100 %) for the 10^4 and 10^5 categories and high sensitivity for 10^1 (92.3 %), 10^2 (85.7 %) and 10^3 (85.7 %). Misclassifications were mostly confined to the adjacent mid-range classes (10^2 and 10^3), indicating some overlap at those decision boundaries. The slightly higher dropout observed in these bins is probably due to their smaller representation in the validation set rather than a limitation of the logarithmic formulation itself. Overall, performance at the extremes remained excellent, enabling reliable detection of both high- and low-concentration samples.

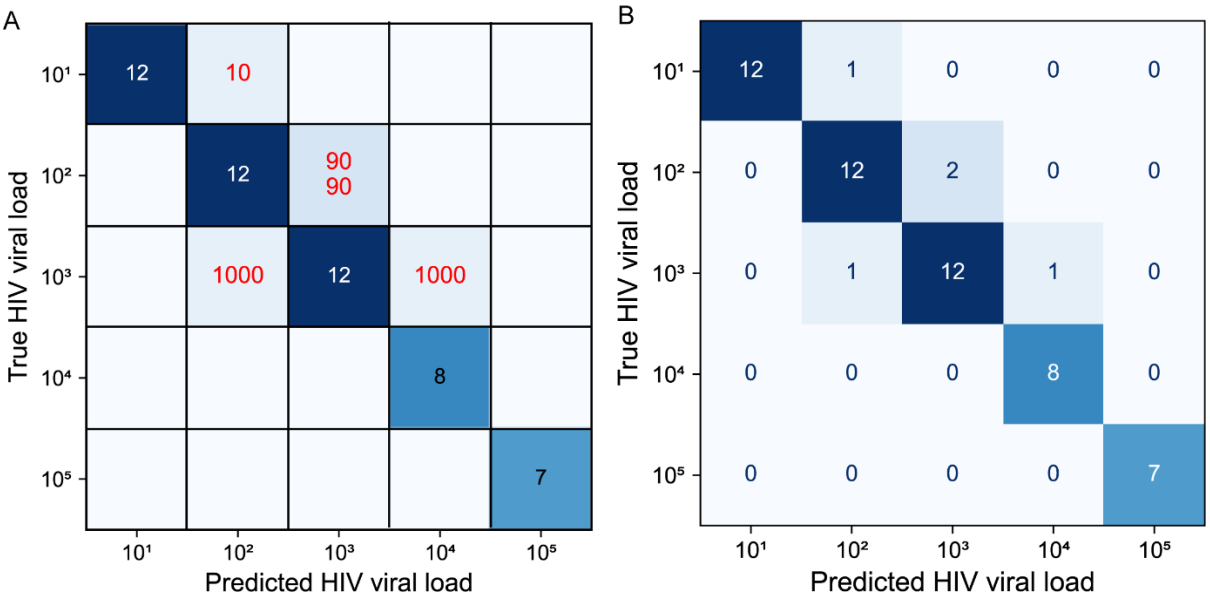

Figure 35 Logarithmic-scale confusion matrix. Confusion matrix shows classification performance across logarithmic-scale categories**.** Each cell represents the number of samples classified into each predicted category. Diagonal entries indicate correct classifications, with darker shades representing higher counts. (A) shows incorrect predictions have the true label quantity in red. (B) show total prediction counts without the incorrect label.

4.4 Discussion

Precise quantification of nucleic acid input concentrations using isothermal amplification methods remains challenging, particularly at high target concentrations where amplification sites grow, merge, and overlap spatially. In conventional implementations of Amplification Nucleation Site Analysis (ANSA), this overlap has historically limited the upper limit of quantification (ULOQ), as simple site counting becomes unreliable when discrete puncta cannot be easily resolved.

In this work, we introduce a machine learning-based strategy that addresses these limitations by leveraging the temporal evolution of amplification reactions. By sampling fluorescence intensity patterns across multiple key timepoints during the amplification process and using a deep convolutional neural network (ResNet-18) for classification, we enrich the feature space available for quantification. Instead of relying solely on static endpoint images, the model integrates both spatial and temporal cues, capturing differences in amplification kinetics that reflect underlying input DNA concentrations.

This approach substantially improves quantification performance across a wide dynamic range, maintaining discriminative accuracy even in cases where visual overlap of amplification sites would confound traditional counting methods. By utilizing time-evolved data, the model can distinguish between reactions that may appear superficially similar at a single timepoint but exhibit distinct temporal growth dynamics.

Notably, this method enables robust classification across input DNA concentrations spanning nearly five orders of magnitude. It provides a scalable, low-complexity alternative to physical partitioning approaches such as droplet digital PCR, without requiring specialized microfluidics, compartmentalization, or intricate hardware. The integration of machine learning directly into the analysis pipeline also opens the possibility for real-time or near-real-time quantitative diagnostics based on simple imaging platforms.

While these results represent a significant advance, challenges remain, particularly at intermediate input concentrations where amplification site density and growth kinetics can overlap. In this regime, the temporal evolution patterns of different concentrations become less distinct, and the models exhibit reduced classification specificity. Misclassification appears to arise not from limitations in optical resolution or imaging capacity, but from biological overlap in amplification dynamics at neighboring concentration ranges. Future work may benefit from incorporating finer temporal sampling, additional spatial features, or ensemble modeling strategies to further enhance specificity in these challenging mid-range conditions.

Overall, this study demonstrates that combining time-resolved imaging with deep learning significantly enhances the quantitative capabilities of isothermal amplification reactions. It establishes a foundation for scalable, field-deployable molecular diagnostics capable of precise nucleic acid quantification without the need for hardware-intensive compartmentalization.

5 Summary and Recommendations

5.1 Summary

The work presented in this dissertation set out to relieve two persistent bottlenecks in point-of-care (POC) nucleic-acid testing by providing reliable sample validation for rapid respiratory diagnostics and wide-range quantification for HIV treatment monitoring by pairing pragmatic chemistry choices with low-cost readouts. Guided by those aims, the thesis delivers (i) a duplexed SARS-CoV-2 reverse-transcription recombinase polymerase amplification (RT-RPA) assay that embeds an MS2 bacteriophage full-process internal control, and (ii) an expanded-range Amplification Nucleation Site Analysis (ANSA) platform, enhanced with microfluidics and machine-learning image analysis, for quantitative HIV viral-load testing. Together these advances illustrate a cohesive strategy for affordable, electricity-light molecular diagnostics that can move from central laboratories into community clinics and even homes.

The SARS-CoV-2 component achieves single-tube duplex amplification and either real-time fluorescence or lateral-flow detection in under 25 minutes. It reaches 25 viral RNA copies per reaction by fluorescence and 50 copies by lateral flow while correctly flagging amplification failures through the MS2 control, thereby safeguarding against false negatives due to lysis, reverse transcription, or amplification errors. The assay also detects Delta and Omicron variants and shows no cross-reactivity with influenza A/B or common seasonal coronaviruses, all while using ambient-temperature-stable TwistAmp Exo pellets that simplify cold-chain logistics.

For HIV, the dissertation pushes membrane-based ANSA from a 50–3000 copy quantitative window to a clinically relevant 20–100,000-copy span. This is accomplished first by physiochemical and microfluidic redesign that reduces site merging at high titers, and then by a ResNet-18 model that uses spatial-temporal fluorescence features to classify viral loads with 92–95 % accuracy across WHO treatment decision bands.

In sum, this dissertation demonstrates that thoughtful assay architecture duplexed internal controls for robustness and image-rich ANSA for quantitation can compress laboratory-grade molecular testing into formats that are fast, inexpensive, and deployable far from mains power. Continued engineering toward sealed, disposable cartridges and expanded field validation will position these technologies to close critical diagnostic gaps for both emergent respiratory viruses and chronic infections such as HIV.

5.2 Reflections and Future work

5.2.1 Buffer Engineering to Push ANSA Performance

My data show that fluorescence intensity peaks at roughly 2.5 – 3.5 % w/w PEG 35 k but collapses when the mixture crosses what I hypothesize to be the PEG-rich/salt-rich phase boundary above about 5 %. Paradoxically, the higher viscosities obtained beyond that point are desirable because they shrink nucleation-site diameters and extend the dynamic range. To decouple viscosity from phase separation I suggest blending hydrophilic polymers such as lower-molecular-weight PEG (4–8 k), dextran 40–70 k, Ficoll 400, polyvinyl-pyrrolidone or other viscous modulators. Additionally, exploring small-molecule viscosifiers like sorbitol or sucrose which will raise viscosity without salting-out. Glycerol in the 5-20 % range was tested in limited capacity but I saw what looked to be signs of non-specific probe cleavage in the form of site that were fractionally the expected size. The two phase system could be further mitigated with fine-tuning of the ionic strength and pH, adjusting KOAc/MgOAc ratios or adding zwitterionic buffers (HEPES, MOPS) in search of conditions that support 6–8 % PEG before phase separation. Mapping this parameter space against bulk fluorescence and site-diameter read-outs will yield a quantitative viscosity/phase-diagram map.

5.2.2 Brighter and More Photostable Reporter Chemistry

Because the assay currently relies on FAM, whose quantum yield and photobleaching limit signal, I suggest testing higher quantum yield and more photostable dyes such as Alexa Fluor 488, Atto 565, sulfo-Cy3/Cy5 and LD655. Alternatively, tandem-labelled probes that double photon output could be explored. To my knowledge, there are no published assays using or evaluating a dual fluorophore exonuclease-cleavage kinetics. The exploration of quantum dots or dye-loaded polymer dots, which have the highest quantum yield with exceptional photostability, would likely improve site signal to noise ratios but at the detriment of a potential POC device requiring laser optics.

5.2.3 Fundamental Studies of ANSA Generalizability

While I show the kinetics of site growth in section 3.3 the fundamental underpinnings of ANSA site formation are unknown which brings the translatability of this technology into question for other assays. Further work should be done across assays of different type (RPA vs RT-RPA, the later was demonstrated stable in Sullivan *et al*) and target types (short vs long vs genomic input nucleic acids) and their effect on ANSA site-count regressions and ResNet predictions. I hypothesize that longer templates should lengthen

polymerase occupancy, slow burst growth and likely delay the frame used for site counting to a small degree; once sufficient amplicon template is available the genomic or long sources will be unfavored and fast amplification should dominate. This will likely hinder the ResNet model more as longer templates might be interpreted as lower concentrations.

5.2.4 Ablation Mapping of ResNet Input Channels

The current ResNet-18 samples seven timepoints that span baseline through plateau. By systematically blanking one channel at a time and tracking validation-accuracy loss, we could identify which frames are most informative. Saliency and Grad-CAM analyses would further reveal whether early-growth or plateau images and which spatial regions drive predictions, guiding buffer modifications and potentially shortening acquisition times for field-deployable readers.

5.2.5 Toward Fully Integrated Cartridges

Combining an optimized buffer, brighter reporters and a truncated imaging sequence with our low-cost glass-slide chip sets the stage for a sealed, blister-actuated cartridge. To date, however, no fully integrated RPA point-of-care device or cartridge has been reported, and several hurdles must still be cleared. Foremost is the formulation's dependence on high-molecular-weight polyethylene glycol: PEG is solid at room temperature, its glass-transition temperature is well above ambient, and even when liquefied the high viscosity complicates both lyophilization and subsequent fluid handling within micro-channels. Addressing this will require either novel cartridge designs capable of metering viscous reagents or the substitution of PEG with alternative molecular crowding agents that retain RPA activity while improving manufacturability as theorized in section 5.2.1. Embedding heat-lysis and lyophilised reagents in laminated pouches would then deliver a single-step, electricity-light device aligned with WHO target product profiles for most infectious diseases. Collectively, these efforts will transform ANSA from a promising laboratory prototype into a robust, broadly translatable platform for quantitative point-of-care diagnostics. Preliminary data show that high-output dental blue LEDs (ams OSRAM LZ1-10DB00-0100, Austria) can excite FAM without additional filtering, further reducing system complexity.

6 Appendix

6.1 6.1 Evaluating EXO versus NFO RPA Kits for Lateral-Flow Analysis

Early experiments were constrained by the unexpected discontinuation of the TwistAmp nfo kit, the formulation traditionally recommended for lateral-flow read-out. Attempts to “re-create” nfo reactions by spiking purified endonuclease IV (10 – 50 000 U rxn^{-1}) into TwistAmp Basic pellets produced only intermittent test-line development at the highest enzyme loads. Figure 36 LFA Comparison of EXO and NFO. Twist EXO kits resulted in similar LFA band intensity compared to the QT Biotech RAA kits. From left to right the test peaks are: Internal flow control, MS2 Control, SARS-CoV-2 Test.shows parallel tests with commercial Recombinase-Aided Amplification (RAA) pellets from QT Biotech showed performance that was indistinguishable from TwistAmp Exo reagents when those Exo pellets were used without their real-time probe and paired instead with 5′-labelled LFA probes. Surprisingly, Exo-based reactions generated robust test-lines even though the exonuclease should, in principle, degrade the fluorophore-labelled strand after probe cleavage. This empirical observation justified adopting Exo pellets for all subsequent duplex SARS-CoV-2/MS2 assays, simplifying screening because the same chemistry now supports either real-time fluorescence or endpoint LFA detection .

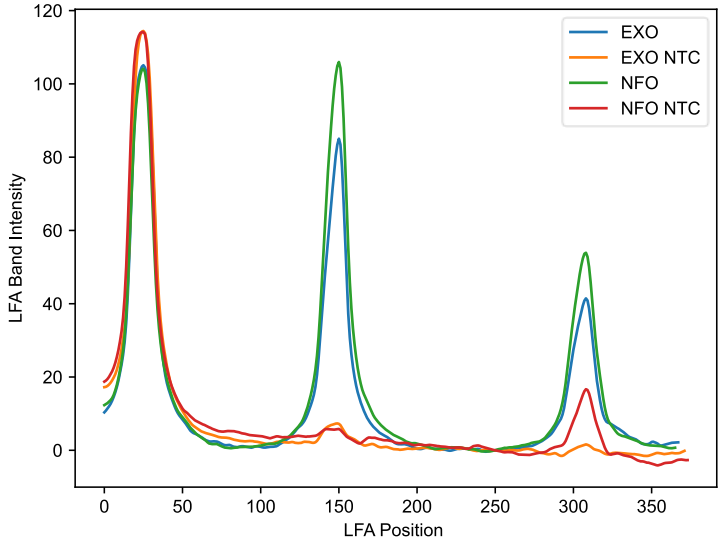

Figure 36 LFA Comparison of EXO and NFO. Twist EXO kits resulted in similar LFA band intensity compared to the QT Biotech RAA kits. From left to right the test peaks are: Internal flow control, MS2 Control, SARS-CoV-2 Test.

6.2 Membrane Based ANSA

6.2.1 Image-Acquisition Optimization for Earlier Site Counting

Image-capture parameters were refined to permit earlier detection of nucleation sites. All previously presented ANSA experiments were conducted on a Nikon AZ100 multizoom microscope equipped with a back-side-illuminated (BSI-Express) CMOS camera. The instrument carries 0.5 ×, 1 × and 5 × objectives with numerical apertures (NA) of 0.10, 0.50 and 0.10, respectively; the published protocol used the 0.5 × objective at 5 × zoom and produced a signal-to-noise ratio (SNR) of 3–5 on membrane.

To test whether a higher NA would improve SNR, a Nikon TE2000 microscope fitted with 2 × (0.60 NA), 10 × (0.30 NA) and 20 × (0.45 NA) objectives were evaluated. These optics increased SNR to 20–30 but caused pronounced photobleaching. Photobleaching was mitigated by lowering the epi-fluorescence excitation power, inserting additional neutral-density filters and synchronizing a source shutter with a sequential transistor–transistor-logic (TTL) circuit. The TTL circuit was driven by a 5 V square-wave generator and delay box to open the shutter 40 ms before each 100 ms exposure on a Photometrics Cascade II camera.

Confocal imaging was also assessed by imaging 16 μm fluorescent microspheres on a Leica SP8 confocal microscope with 10 × (0.30 NA), 20 × (0.70 NA) and 40 × (0.60 NA) objectives. Neither the TE2000 nor the SP8 resolved complete ∼300 μm nucleation sites in the reaction volume because the depth of field at these numerical apertures (2–11 μm) was two orders of magnitude smaller than the site diameter.

Accordingly, the AZ100 fitted with the 1 × (0.10 NA) objective at 3 × zoom was selected for all subsequent work. Images are recorded as 16-bit files with 5 s exposures, yielding an SNR of approximately 10 on membrane. On glass microchip these settings result in a SNR greater than 20.

6.2.2 Physical Geometry Optimization to Increase Upper Quantifiable Range

Optimizing the physical geometry of the reaction area would allow for an increased area for sites to form, further decreasing the density of sites in an effort to reduce site merging. The current membrane used for ANSA is Whatman GF/DVA which is a bound glass fiber membrane that is often used in blood and saliva lateral flow assays. This membrane is highly absorbent necessitating the membrane be cut to 7.2 square millimeters to hold the 50 μL reaction volume. Other membranes have been shown to be compatible with qualitative paper-based LAMP assays. The notable assays utilized other glass fiber membranes,[81] polyethersulfone membranes,[201–203] and track-etched polycarbonate membranes.[82] A potential roadblock in

membranes selection for ANSA is screening them for RPA compatibility and accounting for variations in commercial production. These membranes often have proprietary coating designed for their intended use case, and coatings vary across different suppliers. Unpublished studies in the PRG have shown these coatings to be detrimental to RPA compatibility and necessitated pre-treatment steps to remove such coatings. Additionally, physical constraints on membrane size will need to be set for compatibility with the imaging setup used for detection. Large membranes relative to the working distance of the camera sensor will decrease efficiency of the optical filters and mirrors needed to image the fluorescent sites. Further, in conjunction with section 6.2.1 I have found that decreasing the z-height of the reaction volume leads to significant decreases in signal to noise ratios making image detection of sites much more challenging. For these reasons, optimizing the physical geometry of the reaction area is not on my experimental plan.

6.3 Glass Slide ANSA

6.3.1 Bubble Reduction in ANSA

When the reaction is transferred from membrane to a shallow glass-slide chip, micro-bubbles become the dominant artefact: they fluoresce intensely and can be mistaken for amplification sites by the counting mechanisms. The most effective mitigation is prevention. Pipette mixing is avoided, the “blow-out” step is omitted, and the fully rehydrated RPA mix is briefly degassed under vacuum before MgOAc addition. The finished mixture is loaded by capillary action into oxygen-plasma-treated chips; inlet and outlet ports are then back-filled with mineral oil and sealed with PCR film. This regimen almost eliminates bubble formation and, together with a reduced reaction volume (≤ 97 µL), produces images in which bona-fide nucleation sites can be reliably segmented algorithmically.

6.3.2 Evaluation of Commercial Frame-Seal Cassettes versus Custom Cartridges

The first generation of disposable reaction chambers explored both off-the-shelf frame-seal cassettes and polymer–tape laminates. Commercial frame seals (#SLF0601, BioRad, USA), although convenient, enclosed a nominal 266 µm optical path in a 15x15mm frame that was volumetrically oversized for a 50 µL reactions. Figure 37 show the surplus head-space trapped air, encouraging condensation and recurring bubble nucleation. These voids complicated automated cropping: the liquid phase meandered unpredictably, forcing dynamic masks that undermined the fixed-size image tiles required for the machine-learning pipeline. Custom assemblies based on layered plastics and pressure-sensitive adhesives eliminated the void and allowed for thickness control.

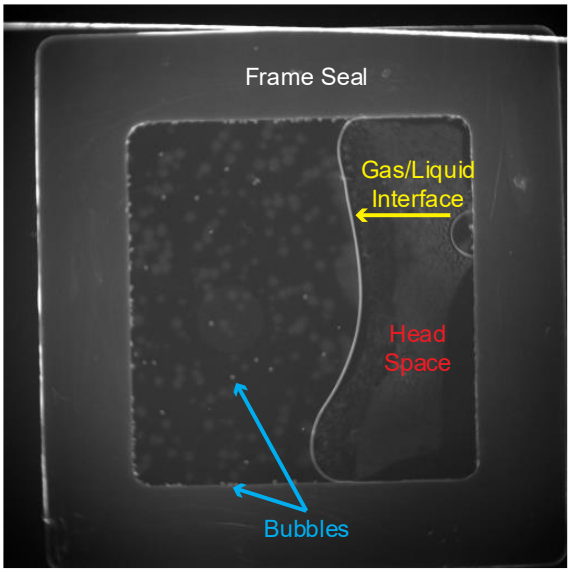

Figure 37 Frame Seal ANSA reaction. The frame seals required the coverslips to be applied in a roll on fashion that was prone to bubble formation on the edge of the frame seal as shown in cyan. The 65 µL volume was also oversized for the 50 µL reaction allowing fo r an void headspace to allow condensation as shown in red. This also made for unpredictable gas/liquid interfaces as shown in yellow.

6.3.3 Modulating the Probe-to-Primer Ratio to Enhance ANSA Signal

To try and boost ANSA site signal I explored increasing the relative probe concentration while keeping the total oligonucleotide concentration constant. The probe fraction was increased and the reverse-primer fraction decreased. Fluorescence rose with probe excess, reaching a modest maximum at ≈ **1.3–1.4** × the baseline probe concentration. This was observed in both T-16 and ANSA reactions. Beyond that point the signal appeared to lose stability and I observed a baseline fluorescence and NTC signal increase. Further this added complexity in preparing the customized master-mixes and outweighed the benefit. Subsequent assays therefore reverted to the standard 1 × probe / 1 × primer formulation.

6.3.4 Reaction-Well Flow Artefacts and Their Mitigation

Thermal Drivers

Initial heaters used a single cartridge element driven by an AC duty-cycle. Using a Flir thermal camera I could see areas of varying temperature. Video microscopy also captured a cyclical “breathing” of the reaction volume synchronized to the heater pulses. Here the reaction could be seen expanding and shrinking with the heater duty cycle. Changing to a DC-powered resistive thin film heater stacked with copper and aluminum spreader plates and backed by insulating expanded polystyrene produced uniform, steady-state temperatures and minimized the breathing artefact. Mineral-oil back-filling also provided an

additional damping and seal that both restricted airborne amplicon release and suppressed residual volumetric fluctuations.

Chemical Drivers

A parallel investigation traced sporadic inter-well flow to ageing polyethylene glycol stocks. Solutions older than one week lost their dispersive character, presumably through micro-aggregation, and the most severe flow events correlated with these “stale” batches. Implementing a weekly 20 % w/v PEG preparation, aliquoting, −20 °C storage and same-day single use restored reagent reliability and eliminated the chemically induced flows.

6.4 Structured Data Generation and Random Forest Regression

Image-analysis pipeline

I implemented a workflow in Python 3.11 to quantify fluorescence-spot formation in time-lapse microscopy stacks to utilize time resolved image features. All images were processed using the method described in section 3.2.4. All analyses were executed on a workstation running Windows 10 with an Intel Core i5-6600 CPU and 16 GB RAM.

Pre-processing and spot detection

Individual image sequences were stored as 16-bit, 3-D TIFF stacks (frames × height × width; typical size ≈ 180 × 500 × 500). Stacks were read with scikit-image v0.23.0 (skimage.io.imread). For each frame we identified putative fluorescence “spots” (puncta) using skimage.feature.peak_local_max with a minimum inter-peak distance of 2 pixels, a relative intensity threshold of 0.01, and an absolute intensity threshold of 150 arbitrary units (a.u.). These parameters were chosen empirically to minimize false positives in background regions while retaining a high degree of visually confirmed spots across a representative training set.

Feature extraction (extract_spot_features)

For every frame (*t)* I recorded (i) the number of detected spots, (ii) the fractional area of the field above the 150-a.u. threshold, and (iii) the mean bulk fluorescence intensity. A reference frame at $t = 90$ (7.5 minutes) served to derive non-temporal descriptors—e.g., spot count, bulk fluorescence, and mean spot size (area ÷ count). This time point was chosen as spots are typically formed by this point and are small enough to not overlap. These are the static time points. The dynamic time points are taken as the largest

change over a 10 frame window and are: Δ max spot count- the largest frame-to-frame spot count increase, Δ max area- the largest increase in high-intensity area, and Δ max bulk- the largest increase in mean bulk intensity.

The time-to-threshold metric was defined as the first frame in which at least one spot was detected. All metrics were collated in a Python dictionary and returned to the calling routine.

Data assembly A hard-coded dictionary mapped each DNA copy-number condition (e.g., “20”, “1000”) to its replicate TIFF filenames. The root directory (G:\Shared drives\Posner Group Current\Cole's Files\ANSA\RPA on glass slides\100_serial\processed) anchored all file paths. The main loop iterated over every (condition, replicate) pair, invoked the extract_spot_features function detailed above, and appended the resulting records to an in-memory list. Each record was annotated with its TIFF filename and parent copy number. The accumulated list was converted to a pandas v2.2.2 DataFrame. Copy-number strings were cast to float64, transformed to log10, and rows containing infinite or NaN values were discarded.

Predictive modelling

The DataFrame generated above was used as a structured data set for Regression tasks. The feature matrix (x variable) includes all columns of the DataFrame except copy_number and log_copy_number; the response (y variable) is log copy number. Three regression families—*LinearRegression*, *DecisionTreeRegressor*, and *RandomForestRegressor*—are benchmarked. For each model I performed 100 independent 80% 20% random train-test splits, Fit the model, and made predictions on the hold-out set, and accumulate train/test mean-squared error (MSE). All predictions were stored in a wide table indexed by the true label to enable error-bar visualization (mean ± SD of predicted values per class). Average train and test MSEs quantify generalization, while the prediction tables feed an aggregated “predicted vs. actual” plot to illustrate systematic bias. To access coefficient stability, the raw coefficients weights are range-normalized ($\beta_i \times (\text{range } x_i)$) and collected over 100 splits. Box-and-whisker, error-bar and swarm plots demonstrate the both the directionality and the variance of each weight, providing insight into feature importance. Figure 38 shows the normalized model coefficients for the random forest regressor for 100 random test train splits of the data. In Figure 38 we can see the dynamic datapoints (max_) show the highest impact on the prediction indicating that adding dynamic factors have a large model weight.

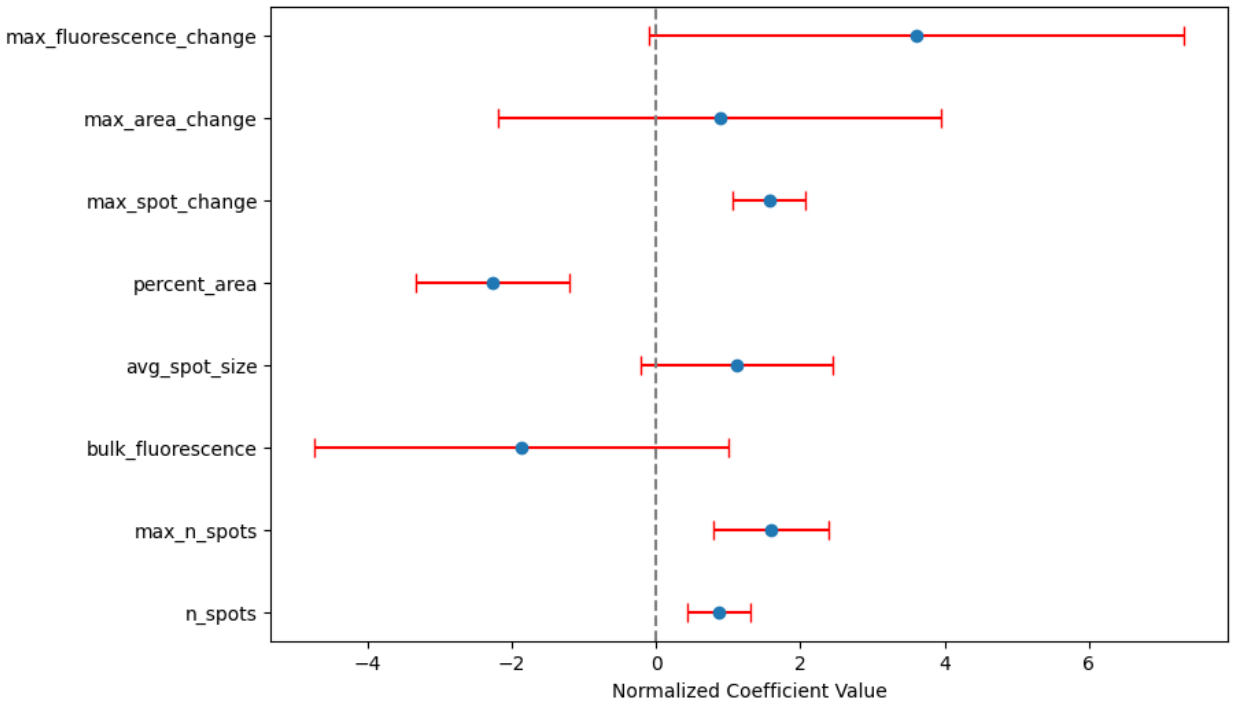

Figure 38 Random Forest Regression Model Weights. The addition of dynamic temporal data (max_ categories) have the highest model weights showing a positive impact of the dynamic data on prediction.

Validation against manual counts

Manually scored spot counts from an independent data set ("Ben's spot counts"- the counted sites from previous publication[66]) are converted to predicted copy numbers via the derived power law from the original publication. The resulting log predictions are compared to their true log copy numbers by MSE, both globally and for the ≤ 3,000 cps subset. These baseline errors are plotted with Random-Forest predictions trained on automated features. Figure 39 show the output of the random forest regressor, the best model by both accuracy and range. Here we see that the added dynamic data and machine learning are able to extend the dynamic range of the prediction to 10,000 copies. This study demonstrates the added value of the machine-learning approach for copy-number estimation.

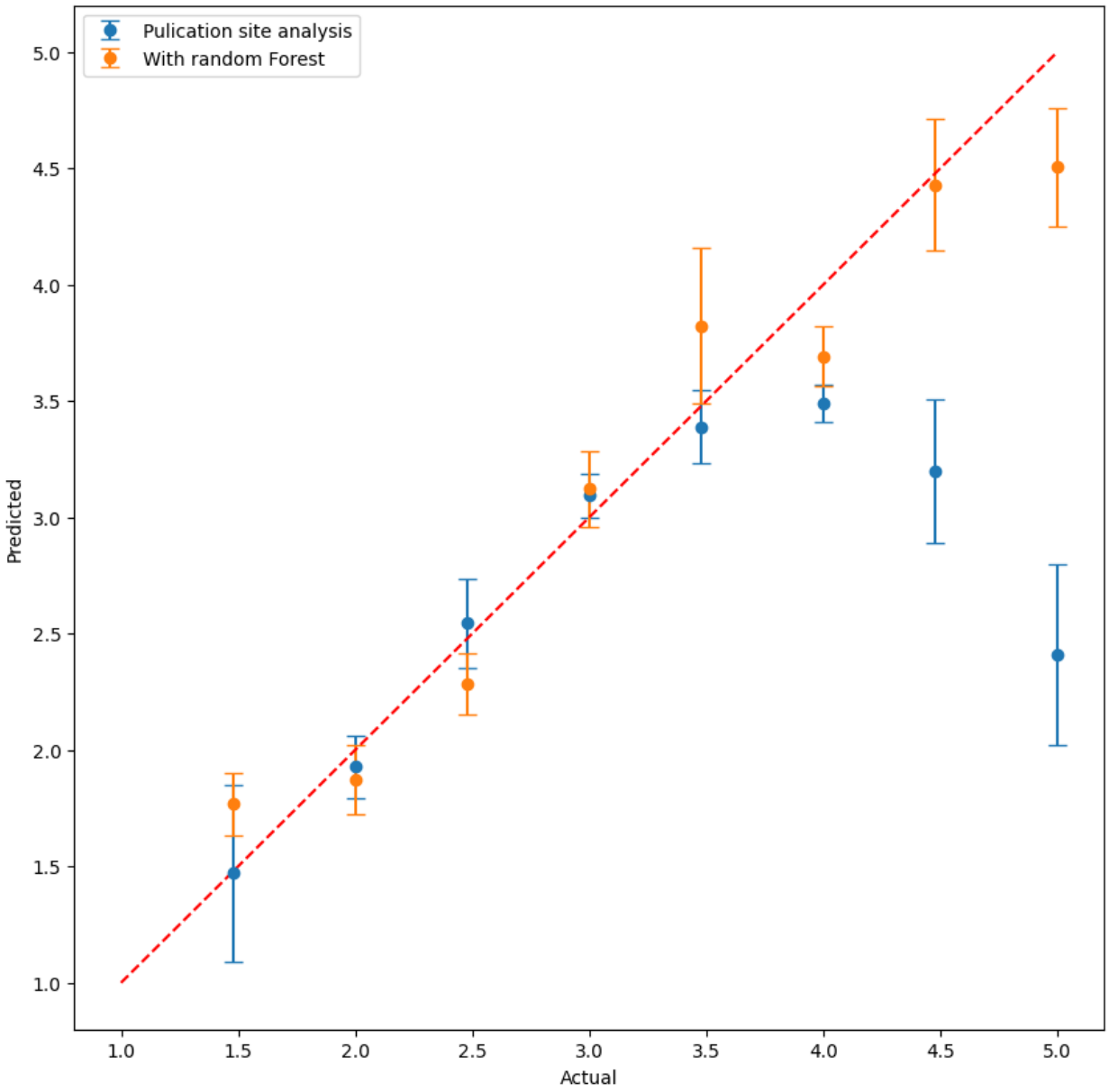

Figure 39 Random Forest Regression Plot. DNA quantification from original ANSA publication shown in blue with three standard deviations. Random forest regression using dynamic structured data shown in orange with three standard deviations. Linear fit shown in dashed red line.

References

(1) Peng, P.; Liu, C.; Li, Z.; Xue, Z.; Mao, P.; Hu, J.; Xu, F.; Yao, C.; You, M. Emerging ELISA Derived Technologies for *in Vitro* Diagnostics. *TrAC Trends Anal. Chem.* **2022**, *152*, 116605. https://doi.org/10.1016/j.trac.2022.116605.

(2) Vashist, S. K.; Marion Schneider, E.; Lam, E.; Hrapovic, S.; Luong, J. H. T. One-Step Antibody Immobilization-Based Rapid and Highly-Sensitive Sandwich ELISA Procedure for Potential in Vitro Diagnostics. *Sci. Rep.* **2014**, *4* (1), 4407. https://doi.org/10.1038/srep04407.

(3) Zhu, H.; Fohlerová, Z.; Pekárek, J.; Basova, E.; Neužil, P. Recent Advances in Lab-on-a-Chip Technologies for Viral Diagnosis. *Biosens. Bioelectron.* **2020**, *153*, 112041. https://doi.org/10.1016/j.bios.2020.112041.

(4) Aydin, S. A Short History, Principles, and Types of ELISA, and Our Laboratory Experience with Peptide/Protein Analyses Using ELISA. *Peptides* **2015**, *72*, 4–15. https://doi.org/10.1016/j.peptides.2015.04.012.

(5) Cox, K. L.; Devanarayan, V.; Kriauciunas, A.; Manetta, J.; Montrose, C.; Sittampalam, S. *Figure 1: [Diagram of a sandwich ELISA...].* https://www.ncbi.nlm.nih.gov/books/NBK92434/figure/immunometh.F1/ (accessed 2024-03-13).

(6) Cornett, J. K.; Kirn, T. J. Laboratory Diagnosis of HIV in Adults: A Review of Current Methods. *Clin. Infect. Dis.* **2013**, *57* (5), 712–718. https://doi.org/10.1093/cid/cit281.

(7) Branson, B. M.; Stekler, J. D. Detection of Acute HIV Infection: We Can't Close the Window. *J. Infect. Dis.* **2012**, *205* (4), 521–524. https://doi.org/10/fx624v.

(8) Wen, J.; Shresta, S. Antigenic Cross-Reactivity between Zika and Dengue Viruses: Is It Time to Develop a Universal Vaccine? *Curr. Opin. Immunol.* **2019**, *59*, 1–8. https://doi.org/10.1016/j.coi.2019.02.001.

(9) Moreno, M. D. L.; Cebolla, Á.; Muñoz-Suano, A.; Carrillo-Carrion, C.; Comino, I.; Pizarro, Á.; León, F.; Rodríguez-Herrera, A.; Sousa, C. Detection of Gluten Immunogenic Peptides in the Urine of Patients with Coeliac Disease Reveals Transgressions in the Gluten-Free Diet and Incomplete Mucosal Healing. *Gut* **2017**, *66* (2), 250–257. https://doi.org/10.1136/gutjnl-2015-310148.

(10) Carrio, A.; Sampedro, C.; Sanchez-Lopez, J. L.; Pimienta, M.; Campoy, P. Automated Low-Cost Smartphone-Based Lateral Flow Saliva Test Reader for Drugs-of-Abuse Detection. *Sensors* **2015**, *15* (11), 29569–29593. https://doi.org/10.3390/s151129569.

(11) Pacifici, R.; Farré, M.; Pichini, S.; Ortuño, J.; Roset, P. N.; Zuccaro, P.; Segura, J.; de la Torre, R. Sweat Testing of MDMA with the Drugwipe® Analytical Device: A Controlled Study with Two Volunteers*. *J. Anal. Toxicol.* **2001**, *25* (2), 144–146. https://doi.org/10.1093/jat/25.2.144.

(12) De Giovanni, N.; Fucci, N. The Current Status of Sweat Testing For Drugs of Abuse: A Review. *Curr. Med. Chem.* **2013**, *20* (4), 545–561. https://doi.org/10.2174/092986713804910139.

(13) Magambo, K. A.; Kalluvya, S. E.; Kapoor, S. W.; Seni, J.; Chofle, A. A.; Fitzgerald, D. W.; Downs, J. A. Utility of Urine and Serum Lateral Flow Assays to Determine the Prevalence and Predictors of Cryptococcal Antigenemia in HIV-Positive Outpatients Beginning Antiretroviral Therapy in Mwanza, Tanzania. *J. Int. AIDS Soc.* **2014**, *17* (1), 19040. https://doi.org/10.7448/IAS.17.1.19040.

(14) Schramm, E. C.; Staten, N. R.; Zhang, Z.; Bruce, S. S.; Kellner, C.; Atkinson, J. P.; Kyttaris, V. C.; Tsokos, G. C.; Petri, M.; Sander Connolly, E.; Olson, P. K. A Quantitative Lateral Flow Assay to Detect Complement Activation in Blood. *Anal. Biochem.* **2015**, *477*, 78–85. https://doi.org/10.1016/j.ab.2015.01.024.

(15) Ang, S. H.; Rambeli, M.; Thevarajah, T. M.; Alias, Y. B.; Khor, S. M. Quantitative, Single-Step Dual Measurement of Hemoglobin A1c and Total Hemoglobin in Human Whole Blood Using a Gold Sandwich Immunochromatographic Assay for Personalized Medicine. *Biosens. Bioelectron.* **2016**, *78*, 187–193. https://doi.org/10.1016/j.bios.2015.11.045.

(16) Ngom, B.; Guo, Y.; Wang, X.; Bi, D. Development and Application of Lateral Flow Test Strip Technology for Detection of Infectious Agents and Chemical Contaminants: A Review. *Anal. Bioanal. Chem.* **2010**, *397* (3), 1113–1135. https://doi.org/10.1007/s00216-010-3661-4.
(17) Lee, S.; Bi, L.; Chen, H.; Lin, D.; Mei, R.; Wu, Y.; Chen, L.; Joo, S.-W.; Choo, J. Recent Advances in Point-of-Care Testing of COVID-19. *Chem. Soc. Rev.* **2023**, *52* (24), 8500–8530. https://doi.org/10.1039/D3CS00709J.
(18) Srivastav, S.; Dankov, A.; Adanalic, M.; Grzeschik, R.; Tran, V.; Pagel-Wieder, S.; Gessler, F.; Spreitzer, I.; Scholz, T.; Schnierle, B.; Anastasiou, O. E.; Dittmer, U.; Schlücker, S. Rapid and Sensitive SERS-Based Lateral Flow Test for SARS-CoV2-Specific IgM/IgG Antibodies. *Anal. Chem.* **2021**, *93* (36), 12391–12399. https://doi.org/10.1021/acs.analchem.1c02305.
(19) Thapa, D.; Samadi, N.; Tabatabaei, N. Handheld Thermo-Photonic Device for Rapid, Low-Cost, and On-Site Detection and Quantification of Anti-SARS-CoV-2 Antibody. *IEEE Sens. J.* **2021**, *21* (17), 18504–18511. https://doi.org/10.1109/JSEN.2021.3089016.
(20) Moghadam, B. Y.; Connelly, K. T.; Posner, J. D. Two Orders of Magnitude Improvement in Detection Limit of Lateral Flow Assays Using Isotachophoresis. *Anal. Chem.* **2015**, *87* (2). https://doi.org/10.1021/ac504552r.
(21) Li, J.; Baird, M. A.; Davis, M. A.; Tai, W.; Zweifel, L. S.; Waldorf, K. M. A.; Gale Jr, M.; Rajagopal, L.; Pierce, R. H.; Gao, X. Dramatic Enhancement of the Detection Limits of Bioassays via Ultrafast Deposition of Polydopamine. *Nat. Biomed. Eng.* **2017**, *1* (6), 1–12. https://doi.org/10.1038/s41551-017-0082.
(22) Bloomfield, M. G.; Balm, M. N. D.; Blackmore, T. K. Molecular Testing for Viral and Bacterial Enteric Pathogens: Gold Standard for Viruses, but Don't Let Culture Go Just Yet? *Pathology (Phila.)* **2015**, *47* (3), 227–233. https://doi.org/10.1097/PAT.0000000000000233.
(23) Forootan, A.; Sjöback, R.; Björkman, J.; Sjögreen, B.; Linz, L.; Kubista, M. Methods to Determine Limit of Detection and Limit of Quantification in Quantitative Real-Time PCR (qPCR). *Biomol. Detect. Quantif.* **2017**, *12*, 1–6. https://doi.org/10.1016/j.bdq.2017.04.001.
(24) Corman, V. M.; Eckerle, I.; Bleicker, T.; Zaki, A.; Landt, O.; Eschbach-Bludau, M.; Boheemen, S. van; Gopal, R.; Ballhause, M.; Bestebroer, T. M.; Muth, D.; Müller, M. A.; Drexler, J. F.; Zambon, M.; Osterhaus, A. D.; Fouchier, R. M.; Drosten, C. Detection of a Novel Human Coronavirus by Real-Time Reverse-Transcription Polymerase Chain Reaction. *Eurosurveillance* **2012**, *17* (39), 20285. https://doi.org/10.2807/ese.17.39.20285-en.
(25) Emery, S. L.; Erdman, D. D.; Bowen, M. D.; Newton, B. R.; Winchell, J. M.; Meyer, R. F.; Tong, S.; Cook, B. T.; Holloway, B. P.; McCaustland, K. A.; Rota, P. A.; Bankamp, B.; Lowe, L. E.; Ksiazek, T. G.; Bellini, W. J.; Anderson, L. J. Real-Time Reverse Transcription–Polymerase Chain Reaction Assay for SARS-Associated Coronavirus. *Emerg. Infect. Dis.* **2004**, *10* (2), 311–316. https://doi.org/10.3201/eid1002.030759.
(26) Enzoklop. Polymerase Chain Reaction. *Wikipedia*; 2024.
(27) Heid, C. A.; Stevens, J.; Livak, K. J.; Williams, P. M. Real Time Quantitative PCR. *Genome Res.* **1996**, *6* (10), 986–994. https://doi.org/10/cnzzwv.
(28) Singanayagam, A.; Patel, M.; Charlett, A.; Lopez Bernal, J.; Saliba, V.; Ellis, J.; Ladhani, S.; Zambon, M.; Gopal, R. Duration of Infectiousness and Correlation with RT-PCR Cycle Threshold Values in Cases of COVID-19, England, January to May 2020. *Eurosurveillance* **2020**, *25* (32). https://doi.org/10/gg9jt7.
(29) Jaafar, R.; Aherfi, S.; Wurtz, N.; Grimaldier, C.; Van Hoang, T.; Colson, P.; Raoult, D.; La Scola, B. Correlation Between 3790 Quantitative Polymerase Chain Reaction–Positives Samples and Positive Cell Cultures, Including 1941 Severe Acute Respiratory Syndrome Coronavirus 2 Isolates. *Clin. Infect. Dis.* **2020**, No. ciaa1491. https://doi.org/10/gjq7f2.
(30) Hsu, C.-S.; Liu, C.-J.; Liu, C.-H.; Wang, C.-C.; Chen, C.-L.; Lai, M.-Y.; Chen, P.-J.; Kao, J.-H.; Chen, D.-S. High Hepatitis C Viral Load Is Associated with Insulin Resistance in Patients with Chronic Hepatitis C. *Liver Int.* **2008**, *28* (2), 271–277. https://doi.org/10.1111/j.1478-3231.2007.01626.x.

(31) Iloeje, U. H.; Yang, H.-I.; Su, J.; Jen, C.-L.; You, S.-L.; Chen, C.-J.; Risk Evaluation of Viral Load Elevation and Associated Liver Disease/Cancer-In HBV (the REVEAL-HBV) Study Group. Predicting Cirrhosis Risk Based on the Level of Circulating Hepatitis B Viral Load. *Gastroenterology* **2006**, *130* (3), 678–686. https://doi.org/10.1053/j.gastro.2005.11.016.

(32) Hindson, B. J.; Ness, K. D.; Masquelier, D. A.; Belgrader, P.; Heredia, N. J.; Makarewicz, A. J.; Bright, I. J.; Lucero, M. Y.; Hiddessen, A. L.; Legler, T. C.; Kitano, T. K.; Hodel, M. R.; Petersen, J. F.; Wyatt, P. W.; Steenblock, E. R.; Shah, P. H.; Bousse, L. J.; Troup, C. B.; Mellen, J. C.; Wittmann, D. K.; Erndt, N. G.; Cauley, T. H.; Koehler, R. T.; So, A. P.; Dube, S.; Rose, K. A.; Montesclaros, L.; Wang, S.; Stumbo, D. P.; Hodges, S. P.; Romine, S.; Milanovich, F. P.; White, H. E.; Regan, J. F.; Karlin-Neumann, G. A.; Hindson, C. M.; Saxonov, S.; Colston, B. W. High-Throughput Droplet Digital PCR System for Absolute Quantitation of DNA Copy Number. *Anal. Chem.* **2011**, *83* (22), 8604–8610. https://doi.org/10/dp5rh9.

(33) Vogelstein, B.; Kinzler, K. W. Digital PCR. *Proc. Natl. Acad. Sci.* **1999**, *96* (16), 9236–9241. https://doi.org/10/bsmd3m.

(34) Kojabad, A. A.; Farzanehpour, M.; Galeh, H. E. G.; Dorostkar, R.; Jafarpour, A.; Bolandian, M.; Nodooshan, M. M. Droplet Digital PCR of Viral DNA/RNA, Current Progress, Challenges, and Future Perspectives. *J. Med. Virol.* **2021**, *93* (7), 4182–4197. https://doi.org/10.1002/jmv.26846.

(35) Heiniger, E. K.; Buser, J. R.; Mireles, L.; Zhang, X.; Ladd, P. D.; Lutz, B. R.; Yager, P. Comparison of Point-of-Care-Compatible Lysis Methods for Bacteria and Viruses. *J. Microbiol. Methods* **2016**, *128*, 80–87. https://doi.org/10.1016/j.mimet.2016.07.007.

(36) de Lange, N.; Tran, T. M.; Abate, A. R. Electrical Lysis of Cells for Detergent-Free Droplet Assays. *Biomicrofluidics* **2016**, *10* (2). https://doi.org/10.1063/1.4944742.

(37) Gill, C.; Wijgert, J. H. H. M. van de; Blow, F.; Darby, A. C. Evaluation of Lysis Methods for the Extraction of Bacterial DNA for Analysis of the Vaginal Microbiota. *PLOS ONE* **2016**, *11* (9), e0163148. https://doi.org/10.1371/journal.pone.0163148.

(38) Boom, R.; Sol, C. J.; Salimans, M. M.; Jansen, C. L.; Wertheim-van Dillen, P. M.; van der Noordaa, J. Rapid and Simple Method for Purification of Nucleic Acids. *J. Clin. Microbiol.* **1990**, *28* (3), 495–503.

(39) Katevatis, C.; Fan, A.; Klapperich, C. M. Low Concentration DNA Extraction and Recovery Using a Silica Solid Phase. *PLOS ONE* **2017**, *12* (5), e0176848. https://doi.org/10.1371/journal.pone.0176848.

(40) Bender, A. T.; Sullivan, B. P.; Lillis, L.; Posner, J. D. Enzymatic and Chemical-Based Methods to Inactivate Endogenous Blood Ribonucleases for Nucleic Acid Diagnostics. *J. Mol. Diagn.* **2020**, *22* (8), 1030–1040. https://doi.org/10/gg892k.

(41) Sambrook, J.; Russell, D. W. Purification of Nucleic Acids by Extraction with Phenol:Chloroform. *Cold Spring Harb. Protoc.* **2006**, *2006* (1), pdb.prot4455. https://doi.org/10.1101/pdb.prot4455.

(42) *RNeasy Kits*. https://www.qiagen.com/us/products/discovery-and-translational-research/dna-rna-purification/rna-purification/total-rna/rneasy-kits/ (accessed 2021-11-16).

(43) Mullis, K. B.; Erlich, H. A.; Arnheim, N.; Horn, G. T.; Saiki, R. K.; Scharf, S. J. Process for Amplifying, Detecting, and/or-Cloning Nucleic Acid Sequences. US4683195A, July 28, 1987. https://patents.google.com/patent/US4683195/en (accessed 2019-10-08).

(44) Forootan, A.; Sjöback, R.; Björkman, J.; Sjögreen, B.; Linz, L.; Kubista, M. Methods to Determine Limit of Detection and Limit of Quantification in Quantitative Real-Time PCR (qPCR). *Biomol. Detect. Quantif.* **2017**, *12*, 1–6. https://doi.org/10.1016/j.bdq.2017.04.001.

(45) Corman, V. M.; Eckerle, I.; Bleicker, T.; Zaki, A.; Landt, O.; Eschbach-Bludau, M.; van Boheemen, S.; Gopal, R.; Ballhause, M.; Bestebroer, T. M.; Muth, D.; Müller, M. A.; Drexler, J. F.; Zambon, M.; Osterhaus, A. D.; Fouchier, R. M.; Drosten, C. Detection of a Novel Human Coronavirus by Real-Time Reverse-Transcription Polymerase Chain Reaction. *Euro Surveill. Bull. Eur. Sur Mal. Transm. Eur. Commun. Dis. Bull.* **2012**, *17* (39), 20285. https://doi.org/10.2807/ese.17.39.20285-en.

(46) Emery, S. L.; Erdman, D. D.; Bowen, M. D.; Newton, B. R.; Winchell, J. M.; Meyer, R. F.; Tong, S.; Cook, B. T.; Holloway, B. P.; McCaustland, K. A.; Rota, P. A.; Bankamp, B.; Lowe, L. E.; Ksiazek, T. G.; Bellini, W. J.; Anderson, L. J. Real-Time Reverse Transcription-Polymerase Chain Reaction Assay for SARS-Associated Coronavirus. *Emerg. Infect. Dis.* **2004**, *10* (2), 311–316. https://doi.org/10.3201/eid1002.030759.

(47) Gudnason, H.; Dufva, M.; Bang, D. D.; Wolff, A. Comparison of Multiple DNA Dyes for Real-Time PCR: Effects of Dye Concentration and Sequence Composition on DNA Amplification and Melting Temperature. *Nucleic Acids Res.* **2007**, *35* (19), e127. https://doi.org/10.1093/nar/gkm671.

(48) Drummond, T. G.; Hill, M. G.; Barton, J. K. Electrochemical DNA Sensors. *Nat. Biotechnol.* **2003**, *21* (10), 1192–1199. https://doi.org/10.1038/nbt873.

(49) Tomita, N.; Mori, Y.; Kanda, H.; Notomi, T. Loop-Mediated Isothermal Amplification (LAMP) of Gene Sequences and Simple Visual Detection of Products. *Nat. Protoc.* **2008**, *3* (5), 877–882. https://doi.org/10.1038/nprot.2008.57.

(50) Chang, J.; Omuomo, K.; Anyango, E.; Kingwara, L.; Basiye, F.; Morwabe, A.; Shanmugam, V.; Nguyen, S.; Sabatier, J.; Zeh, C.; Ellenberger, D. Field Evaluation of Abbott Real Time HIV-1 Qualitative Test for Early Infant Diagnosis Using Dried Blood Spots Samples in Comparison to Roche COBAS Ampliprep/COBAS TaqMan HIV-1 Qual Test in Kenya. *J. Virol. Methods* **2014**, *204*, 25–30. https://doi.org/10.1016/j.jviromet.2014.03.010.

(51) Oliveira, B. B.; Veigas, B.; Baptista, P. V. Isothermal Amplification of Nucleic Acids: The Race for the Next "Gold Standard." *Front. Sens.* **2021**, *2*. https://doi.org/10.3389/fsens.2021.752600.

(52) Mori, Y.; Nagamine, K.; Tomita, N.; Notomi, T. Detection of Loop-Mediated Isothermal Amplification Reaction by Turbidity Derived from Magnesium Pyrophosphate Formation. *Biochem. Biophys. Res. Commun.* **2001**, *289* (1), 150–154. https://doi.org/10.1006/bbrc.2001.5921.

(53) Landaverde, L.; Wong, W.; Hernandez, G.; Fan, A.; Klapperich, C. Method for the Elucidation of LAMP Products Captured on Lateral Flow Strips in a Point of Care Test for HPV 16. *Anal. Bioanal. Chem.* **2020**, *412* (24), 6199–6209. https://doi.org/10.1007/s00216-020-02702-9.

(54) Curtis, K. A.; Rudolph, D. L.; Owen, S. M. Sequence-Specific Detection Method for Reverse Transcription, Loop-Mediated Isothermal Amplification of HIV-1. *J. Med. Virol.* **2009**, *81* (6), 966–972. https://doi.org/10.1002/jmv.21490.

(55) Dao Thi, V. L.; Herbst, K.; Boerner, K.; Meurer, M.; Kremer, L. P.; Kirrmaier, D.; Freistaedter, A.; Papagiannidis, D.; Galmozzi, C.; Stanifer, M. L.; Boulant, S.; Klein, S.; Chlanda, P.; Khalid, D.; Barreto Miranda, I.; Schnitzler, P.; Kräusslich, H.-G.; Knop, M.; Anders, S. A Colorimetric RT-LAMP Assay and LAMP-Sequencing for Detecting SARS-CoV-2 RNA in Clinical Samples. *Sci. Transl. Med.* **2020**, *12* (556), eabc7075. https://doi.org/10.1126/scitranslmed.abc7075.

(56) Kargar, M.; Askari, A.; Doosti, A.; Ghorbani-Dalini, S. Loop-Mediated Isothermal Amplification Assay for Rapid Detection of Hepatitis C Virus. *Indian J. Virol.* **2012**, *23* (1), 18–23. https://doi.org/10/gm3w99.

(57) Cai, T.; Lou, G.; Yang, J.; Xu, D.; Meng, Z. Development and Evaluation of Real-Time Loop-Mediated Isothermal Amplification for Hepatitis B Virus DNA Quantification: A New Tool for HBV Management. *J. Clin. Virol. Off. Publ. Pan Am. Soc. Clin. Virol.* **2008**, *41* (4), 270–276. https://doi.org/10.1016/j.jcv.2007.11.025.

(58) Becherer, L.; Borst, N.; Bakheit, M.; Frischmann, S.; Zengerle, R.; Stetten, F. von. Loop-Mediated Isothermal Amplification (LAMP) – Review and Classification of Methods for Sequence-Specific Detection. *Anal. Methods* **2020**, *12* (6), 717–746. https://doi.org/10.1039/C9AY02246E.

(59) Euler, M.; Wang, Y.; Nentwich, O.; Piepenburg, O.; Hufert, F. T.; Weidmann, M. Recombinase Polymerase Amplification Assay for Rapid Detection of Rift Valley Fever Virus. *J. Clin. Virol.* **2012**, *54* (4), 308–312. https://doi.org/10.1016/j.jcv.2012.05.006.

(60) Lillis, L.; Lehman, D.; Singhal, M. C.; Cantera, J.; Singleton, J.; Labarre, P.; Toyama, A.; Piepenburg, O.; Parker, M.; Wood, R.; Overbaugh, J.; Boyle, D. S. Non-Instrumented Incubation of a Recombinase Polymerase Amplification Assay for the Rapid and Sensitive Detection of

Proviral HIV-1 DNA. *PLOS ONE* **2014**, *9* (9), e108189. https://doi.org/10.1371/journal.pone.0108189.
(61) Boyle, D. S.; Lehman, D. A.; Lillis, L.; Peterson, D.; Singhal, M.; Armes, N.; Parker, M.; Piepenburg, O.; Overbaugh, J. Rapid Detection of HIV-1 Proviral DNA for Early Infant Diagnosis Using Recombinase Polymerase Amplification. *mBio* **2013**, *4* (2), e00135-13. https://doi.org/10.1128/mBio.00135-13.
(62) Lobato, I. M.; O'Sullivan, C. K. Recombinase Polymerase Amplification: Basics, Applications and Recent Advances. *TrAC Trends Anal. Chem.* **2018**, *98*, 19–35. https://doi.org/10.1016/j.trac.2017.10.015.
(63) Niemz, A.; Ferguson, T. M.; Boyle, D. S. Point-of-Care Nucleic Acid Testing for Infectious Diseases. *Trends Biotechnol.* **2011**, *29* (5), 240–250. https://doi.org/10.1016/j.tibtech.2011.01.007.
(64) Euler, M.; Wang, Y.; Nentwich, O.; Piepenburg, O.; Hufert, F. T.; Weidmann, M. Recombinase Polymerase Amplification Assay for Rapid Detection of Rift Valley Fever Virus. *J. Clin. Virol.* **2012**, *54* (4), 308–312. https://doi.org/10.1016/j.jcv.2012.05.006.
(65) Crannell, Z. A.; Rohrman, B.; Richards-Kortum, R. Development of a Quantitative Recombinase Polymerase Amplification Assay with an Internal Positive Control. *J. Vis. Exp. JoVE* **2015**, No. 97. https://doi.org/10.3791/52620.
(66) Sullivan, B. P.; Chou, Y.-S.; Bender, A. T.; Martin, C. D.; Kaputa, Z. G.; March, H.; Song, M.; Posner, J. D. Quantitative Isothermal Amplification on Paper Membranes Using Amplification Nucleation Site Analysis. *Lab. Chip* **2022**, *22* (12), 2352–2363. https://doi.org/10/gqmxgs.
(67) Bender, A. T.; Borysiak, M. D.; Levenson, A. M.; Lillis, L.; Boyle, D. S.; Posner, J. D. Semi-Quantitative Nucleic Acid Test with Simultaneous Isotachophoretic Extraction and Amplification. *Anal. Chem.* **2018**, *90* (12), 7221–7229. https://doi.org/10/gdstm8.
(68) Li, J.; Macdonald, J.; von Stetten, F. Review: A Comprehensive Summary of a Decade Development of the Recombinase Polymerase Amplification. *The Analyst* **2018**, *144* (1), 31–67. https://doi.org/10.1039/c8an01621f.
(69) Wahed, A. A. E.; Patel, P.; Faye, O.; Thaloengsok, S.; Heidenreich, D.; Matangkasombut, P.; Manopwisedjaroen, K.; Sakuntabhai, A.; Sall, A. A.; Hufert, F. T.; Weidmann, M. Recombinase Polymerase Amplification Assay for Rapid Diagnostics of Dengue Infection. *PLOS ONE* **2015**, *10* (6), e0129682. https://doi.org/10/gg5pbt.
(70) Abd El Wahed, A.; Patel, P.; Heidenreich, D.; Hufert, F. T.; Weidmann, M. Reverse Transcription Recombinase Polymerase Amplification Assay for the Detection of Middle East Respiratory Syndrome Coronavirus. *PLoS Curr.* **2013**, *5*. https://doi.org/10/gk7k2p.
(71) Lillis, L.; Lehman, D. A.; Siverson, J. B.; Weis, J.; Cantera, J.; Parker, M.; Piepenburg, O.; Overbaugh, J.; Boyle, D. S. Cross-Subtype Detection of HIV-1 Using Reverse Transcription and Recombinase Polymerase Amplification. *J. Virol. Methods* **2016**, *230*, 28–35. https://doi.org/10.1016/j.jviromet.2016.01.010.
(72) Mazutis, L.; Araghi, A. F.; Miller, O. J.; Baret, J.-C.; Frenz, L.; Janoshazi, A.; Taly, V.; Miller, B. J.; Hutchison, J. B.; Link, D.; Griffiths, A. D.; Ryckelynck, M. Droplet-Based Microfluidic Systems for High-Throughput Single DNA Molecule Isothermal Amplification and Analysis. *Anal. Chem.* **2009**, *81* (12), 4813–4821. https://doi.org/10/crdzgd.
(73) Schuler, F.; Siber, C.; Hin, S.; Wadle, S.; Paust, N.; Zengerle, R.; Stetten, F. von. Digital Droplet LAMP as a Microfluidic App on Standard Laboratory Devices. *Anal. Methods* **2016**, *8* (13), 2750–2755. https://doi.org/10.1039/C6AY00600K.
(74) Rane, T. D.; Chen, L.; Zec, H. C.; Wang, T.-H. Microfluidic Continuous Flow Digital Loop-Mediated Isothermal Amplification (LAMP). *Lab. Chip* **2015**, *15* (3), 776–782. https://doi.org/10.1039/C4LC01158A.
(75) Zhu, Q.; Gao, Y.; Yu, B.; Ren, H.; Qiu, L.; Han, S.; Jin, W.; Jin, Q.; Mu, Y. Self-Priming Compartmentalization Digital LAMP for Point-of-Care. *Lab. Chip* **2012**, *12* (22), 4755–4763. https://doi.org/10.1039/C2LC40774D.

(76) Gansen, A.; Herrick, A. M.; Dimov, I. K.; Lee, L. P.; Chiu, D. T. Digital LAMP in a Sample Self-Digitization (SD) Chip. *Lab. Chip* **2012**, *12* (12), 2247–2254. https://doi.org/10/gmfjb5.
(77) Du, W.; Li, L.; Nichols, K. P.; Ismagilov, R. F. SlipChip. *Lab. Chip* **2009**, *9* (16), 2286–2292. https://doi.org/10.1039/B908978K.
(78) Shen, F.; Du, W.; Kreutz, J. E.; Fok, A.; Ismagilov, R. F. Digital PCR on a SlipChip. *Lab. Chip* **2010**, *10* (20), 2666–2672. https://doi.org/10/dq4jvp.
(79) Zhu, Y.; Wu, X.; Gu, A.; Dobelle, L.; Cid, C. A.; Li, J.; Hoffmann, M. R. Membrane-Based In-Gel Loop-Mediated Isothermal Amplification (mgLAMP) System for SARS-CoV-2 Quantification in Environmental Waters. *Environ. Sci. Technol.* **2021**, acs.est.1c04623. https://doi.org/10/gnzkms.
(80) Huang, X.; Lin, X.; Urmann, K.; Li, L.; Xie, X.; Jiang, S.; Hoffmann, M. R. Smartphone-Based in-Gel Loop-Mediated Isothermal Amplification (gLAMP) System Enables Rapid Coliphage MS2 Quantification in Environmental Waters. *Environ. Sci. Technol.* **2018**, *52* (11), 6399–6407. https://doi.org/10/gdqtcs.
(81) Liu, M.; Zhao, Y.; Monshat, H.; Tang, Z.; Wu, Z.; Zhang, Q.; Lu, M. An IoT-Enabled Paper Sensor Platform for Real-Time Analysis of Isothermal Nucleic Acid Amplification Tests. *Biosens. Bioelectron.* **2020**, *169*, 112651. https://doi.org/10/gmfjb3.
(82) Lin, X.; Huang, X.; Urmann, K.; Xie, X.; Hoffmann, M. R. Digital Loop-Mediated Isothermal Amplification on a Commercial Membrane. *ACS Sens.* **2019**, *4* (1), 242–249. https://doi.org/10/gmfjb4.
(83) Shah, K. G.; Kumar, S.; Yager, P. Near-Digital Amplification in Paper Improves Sensitivity and Speed in Biplexed Reactions. *Sci. Rep.* **2022**, *12* (1), 14618. https://doi.org/10.1038/s41598-022-18937-8.
(84) Valloly, P.; Roy, R. Nucleic Acid Quantification with Amplicon Yield in Recombinase Polymerase Amplification. *Anal. Chem.* **2022**, *94* (40), 13897–13905. https://doi.org/10.1021/acs.analchem.2c02810.
(85) Puhach, O.; Meyer, B.; Eckerle, I. SARS-CoV-2 Viral Load and Shedding Kinetics. *Nat. Rev. Microbiol.* **2022**. https://doi.org/10.1038/s41579-022-00822-w.
(86) Brihn, A.; Chang, J.; OYong, K.; Balter, S.; Terashita, D.; Rubin, Z.; Yeganeh, N. Diagnostic Performance of an Antigen Test with RT-PCR for the Detection of SARS-CoV-2 in a Hospital Setting — Los Angeles County, California, June–August 2020. *MMWR Morb. Mortal. Wkly. Rep.* **2021**, *70* (19), 702–706. https://doi.org/10.15585/mmwr.mm7019a3.
(87) Drain, P. K. Rapid Diagnostic Testing for SARS-CoV-2. *N. Engl. J. Med.* **2022**, *386* (3), 264–272. https://doi.org/10.1056/NEJMcp2117115.
(88) Chu, V. T.; Schwartz, N. G.; Donnelly, M. A. P.; Chuey, M. R.; Soto, R.; Yousaf, A. R.; Schmitt-Matzen, E. N.; Sleweon, S.; Ruffin, J.; Thornburg, N.; Harcourt, J. L.; Tamin, A.; Kim, G.; Folster, J. M.; Hughes, L. J.; Tong, S.; Stringer, G.; Albanese, B. A.; Totten, S. E.; Hudziec, M. M.; Matzinger, S. R.; Dietrich, E. A.; Sheldon, S. W.; Stous, S.; McDonald, E. C.; Austin, B.; Beatty, M. E.; Staples, J. E.; Killerby, M. E.; Hsu, C. H.; Tate, J. E.; Kirking, H. L.; Matanock, A.; COVID-19 Household Transmission Team. Comparison of Home Antigen Testing With RT-PCR and Viral Culture During the Course of SARS-CoV-2 Infection. *JAMA Intern. Med.* **2022**, *182* (7), 701–709. https://doi.org/10.1001/jamainternmed.2022.1827.
(89) CDC. *COVID-19 and Your Health*. Centers for Disease Control and Prevention. https://www.cdc.gov/coronavirus/2019-ncov/symptoms-testing/testing.html (accessed 2024-02-09).
(90) Perchetti, G. A.; Huang, M.-L.; Mills, M. G.; Jerome, K. R.; Greninger, A. L. Analytical Sensitivity of the Abbott BinaxNOW COVID-19 Ag Card. *J. Clin. Microbiol.* **2021**, *59* (3), e02880-20. https://doi.org/10.1128/JCM.02880-20.
(91) Kahn, M.; Schuierer, L.; Bartenschlager, C.; Zellmer, S.; Frey, R.; Freitag, M.; Dhillon, C.; Heier, M.; Ebigbo, A.; Denzel, C.; Temizel, S.; Messmann, H.; Wehler, M.; Hoffmann, R.; Kling, E.; Römmele, C. Performance of Antigen Testing for Diagnosis of COVID-19: A Direct Comparison

of a Lateral Flow Device to Nucleic Acid Amplification Based Tests. *BMC Infect. Dis.* **2021**, *21* (1), 798. https://doi.org/10.1186/s12879-021-06524-7.
(92) Brümmer, L. E.; Katzenschlager, S.; McGrath, S.; Schmitz, S.; Gaeddert, M.; Erdmann, C.; Bota, M.; Grilli, M.; Larmann, J.; Weigand, M. A.; Pollock, N. R.; Macé, A.; Erkosar, B.; Carmona, S.; Sacks, J. A.; Ongarello, S.; Denkinger, C. M. Accuracy of Rapid Point-of-Care Antigen-Based Diagnostics for SARS-CoV-2: An Updated Systematic Review and Meta-Analysis with Meta-Regression Analyzing Influencing Factors. *PLOS Med.* **2022**, *19* (5), e1004011. https://doi.org/10.1371/journal.pmed.1004011.
(93) Ashagre, W.; Atnafu, A.; Wassie, L.; Tschopp, R.; Fentahun, D.; Assefa, G.; Wegayehu, T.; Wondale, B.; Mulu, A.; Miheret, A.; Bobosha, K. Evaluation of the Diagnostic Performance of PanbioTM Abbott SARS-CoV-2 Rapid Antigen Test for the Detection of COVID-19 from Suspects Attending ALERT Center. *PLOS ONE* **2022**, *17* (11), e0277779. https://doi.org/10.1371/journal.pone.0277779.
(94) Y. Zhang, J.; T. Bender, A.; S. Boyle, D.; K. Drain, P.; D. Posner, J. Current State of Commercial Point-of-Care Nucleic Acid Tests for Infectious Diseases. *Analyst* **2021**, *146* (8), 2449–2462. https://doi.org/10.1039/D0AN01988G.
(95) I. Wilner, O.; Yesodi, D.; Weizmann, Y. Point-of-Care Nucleic Acid Tests: Assays and Devices. *Nanoscale* **2023**, *15* (3), 942–952. https://doi.org/10.1039/D2NR05385C.
(96) Islam, M. M.; Koirala, D. Toward a Next-Generation Diagnostic Tool: A Review on Emerging Isothermal Nucleic Acid Amplification Techniques for the Detection of SARS-CoV-2 and Other Infectious Viruses. *Anal. Chim. Acta* **2022**, *1209*, 339338. https://doi.org/10.1016/j.aca.2021.339338.
(97) Kang, T.; Lu, J.; Yu, T.; Long, Y.; Liu, G. Advances in Nucleic Acid Amplification Techniques (NAATs): COVID-19 Point-of-Care Diagnostics as an Example. *Biosens. Bioelectron.* **2022**, *206*, 114109. https://doi.org/10.1016/j.bios.2022.114109.
(98) Mardian, Y.; Kosasih, H.; Karyana, M.; Neal, A.; Lau, C.-Y. Review of Current COVID-19 Diagnostics and Opportunities for Further Development. *Front. Med.* **2021**, *8*.
(99) Peeling, R. W.; Heymann, D. L.; Teo, Y.-Y.; Garcia, P. J. Diagnostics for COVID-19: Moving from Pandemic Response to Control. *The Lancet* **2022**, *399* (10326), 757–768. https://doi.org/10.1016/S0140-6736(21)02346-1.
(100) *Cue Health to provide COVID-19 testing for 2021-22 NBA season*. NBA.com. https://www.nba.com/news/cue-health-to-provide-covid-19-testing-for-2021-22-nba-season (accessed 2024-03-11).
(101) *First-of-its-kind Cue Health Partnership with Air Canada Provides U.S.-based Customers with Special Access to the Most Accurate COVID-19 Self-Test | Cue*. https://cuehealth.com/about/press/first-of-its-kind-cue-health-partnership-with-air-canada-provides-u.s.-based (accessed 2024-03-11).
(102) Hymes, K.; Greene, J.; Marcus, A.; William, D.; Cheung, T.; Prose, N.; Ballard, H.; Laubenstein, L. KAPOSI'S SARCOMA IN HOMOSEXUAL MEN—A REPORT OF EIGHT CASES. *The Lancet* **1981**, *318* (8247), 598–600. https://doi.org/10.1016/S0140-6736(81)92740-9.
(103) *Global HIV & AIDS statistics — Fact sheet*. https://www.unaids.org/en/resources/fact-sheet (accessed 2024-01-24).
(104) *HIV*. https://www.who.int/data/gho/data/themes/hiv-aids (accessed 2024-01-24).
(105) del Rio, C. The Global HIV Epidemic: What the Pathologist Needs to Know. *Semin. Diagn. Pathol.* **2017**, *34* (4), 314–317. https://doi.org/10.1053/j.semdp.2017.05.001.
(106) Becerra, J. C.; Bildstein, L. S.; Gach, J. S. Recent Insights into the HIV/AIDS Pandemic. *Microb. Cell 3* (9), 451–475. https://doi.org/10.15698/mic2016.09.529.
(107) Hutchinson, J. F. THE BIOLOGY AND EVOLUTION OF HIV. *Annu. Rev. Anthropol.* **2001**, *Volume 30*, 85–108. https://doi-org.offcampus.lib.washington.edu/10.1146/annurev.anthro.30.1.85.
(108) Okoye, A. A.; Picker, L. J. CD4+ T Cell Depletion in HIV Infection: Mechanisms of Immunological Failure. *Immunol. Rev.* **2013**, *254* (1), 54–64. https://doi.org/10.1111/imr.12066.

(109) Hernandez-Vargas, E. A.; Middleton, R. H. Modeling the Three Stages in HIV Infection. *J. Theor. Biol.* **2013**, *320*, 33–40. https://doi.org/10.1016/j.jtbi.2012.11.028.
(110) Bbosa, N.; Kaleebu, P.; Ssemwanga, D. HIV Subtype Diversity Worldwide. *Curr. Opin. HIV AIDS* **2019**, *14* (3), 153–160. https://doi.org/10.1097/COH.0000000000000534.
(111) Robertson, D. L.; Anderson, J. P.; Bradac, J. A.; Carr, J. K.; Foley, B.; Funkhouser, R. K.; Gao, F.; Hahn, B. H.; Kalish, M. L.; Kuiken, C.; others. HIV-1 Nomenclature Proposal. *Science* **2000**, *288* (5463), 55–55.
(112) Hemelaar, J.; Elangovan, R.; Yun, J.; Dickson-Tetteh, L.; Fleminger, I.; Kirtley, S.; Williams, B.; Gouws-Williams, E.; Ghys, P. D.; Abimiku, A. G.; Agwale, S.; Archibald, C.; Avidor, B.; Barbás, M. G.; Barre-Sinoussi, F.; Barugahare, B.; Belabbes, E. H.; Bertagnolio, S.; Birx, D.; Bobkov, A. F.; Brandful, J.; Bredell, H.; Brennan, C. A.; Brooks, J.; Bruckova, M.; Buonaguro, L.; Buonaguro, F.; Buttò, S.; Buve, A.; Campbell, M.; Carr, J.; Carrera, A.; Carrillo, M. G.; Celum, C.; Chaplin, B.; Charles, M.; Chatzidimitriou, D.; Chen, Z.; Chijiwa, K.; Cooper, D.; Cunningham, P.; Dagnra, A.; de Gascun, C. F.; Del Amo, J.; Delgado, E.; Dietrich, U.; Dwyer, D.; Ellenberger, D.; Ensoli, B.; Essex, M.; Gao, F.; Fleury, H.; Fonjungo, P. N.; Foulongne, V.; Gadkari, D. A.; García, F.; Garsia, R.; Gershy-Damet, G. M.; Glynn, J. R.; Goodall, R.; Grossman, Z.; Lindenmeyer-Guimarães, M.; Hahn, B.; Hamers, R. L.; Hamouda, O.; Handema, R.; He, X.; Herbeck, J.; Ho, D. D.; Holguin, A.; Hosseinipour, M.; Hunt, G.; Ito, M.; Bel Hadj Kacem, M. A.; Kahle, E.; Kaleebu, P. K.; Kalish, M.; Kamarulzaman, A.; Kang, C.; Kanki, P.; Karamov, E.; Karasi, J.-C.; Kayitenkore, K.; Kelleher, T.; Kitayaporn, D.; Kostrikis, L. G.; Kucherer, C.; Lara, C.; Leitner, T.; Liitsola, K.; Lingappa, J.; Linka, M.; Lorenzana de Rivera, I.; Lukashov, V.; Maayan, S.; Mayr, L.; McCutchan, F.; Meda, N.; Menu, E.; Mhalu, F.; Mloka, D.; Mokili, J. L.; Montes, B.; Mor, O.; Morgado, M.; Mosha, F.; Moussi, A.; Mullins, J.; Najera, R.; Nasr, M.; Ndembi, N.; Neilson, J. R.; Nerurkar, V. R.; Neuhann, F.; Nolte, C.; Novitsky, V.; Nyambi, P.; Ofner, M.; Paladin, F. J.; Papa, A.; Pape, J.; Parkin, N.; Parry, C.; Peeters, M.; Pelletier, A.; Pérez-Álvarez, L.; Pillay, D.; Pinto, A.; Quang, T. D.; Rademeyer, C.; Raikanikoda, F.; Rayfield, M. A.; Reynes, J.-M.; Rinke de Wit, T.; Robbins, K. E.; Rolland, M.; Rousseau, C.; Salazar-Gonzales, J.; Salem, H.; Salminen, M.; Salomon, H.; Sandstrom, P.; Santiago, M. L.; Sarr, A. D.; Schroeder, B.; Segondy, M.; Selhorst, P.; Sempala, S.; Servais, J.; Shaik, A.; Shao, Y.; Slim, A.; Soares, M. A.; Songok, E.; Stewart, D.; Stokes, J.; Subbarao, S.; Sutthent, R.; Takehisa, J.; Tanuri, A.; Tee, K. K.; Thapa, K.; Thomson, M.; Tran, T.; Urassa, W.; Ushijima, H.; van de Perre, P.; van der Groen, G.; van Laethem, K.; van Oosterhout, J.; van Sighem, A.; van Wijngaerden, E.; Vandamme, A.-M.; Vercauteren, J.; Vidal, N.; Wallace, L.; Williamson, C.; Wolday, D.; Xu, J.; Yang, C.; Zhang, L.; Zhang, R. Global and Regional Molecular Epidemiology of HIV-1, 1990–2015: A Systematic Review, Global Survey, and Trend Analysis. *Lancet Infect. Dis.* **2019**, *19* (2), 143–155. https://doi.org/10/gjhwk8.
(113) Gallant, J.; Lazzarin, A.; Mills, A.; Orkin, C.; Podzamczer, D.; Tebas, P.; Girard, P.-M.; Brar, I.; Daar, E. S.; Wohl, D.; Rockstroh, J.; Wei, X.; Custodio, J.; White, K.; Martin, H.; Cheng, A.; Quirk, E. Bictegravir, Emtricitabine, and Tenofovir Alafenamide versus Dolutegravir, Abacavir, and Lamivudine for Initial Treatment of HIV-1 Infection (GS-US-380-1489): A Double-Blind, Multicentre, Phase 3, Randomised Controlled Non-Inferiority Trial. *The Lancet* **2017**, *390* (10107), 2063–2072. https://doi.org/10/gcjx6s.
(114) *Updated recommendations on first-line and second-line antiretroviral regimens and post-exposure prophylaxis and recommendations on early infant diagnosis of HIV*. https://www.who.int/publications-detail-redirect/WHO-CDS-HIV-18.51 (accessed 2021-11-12).
(115) UNAIDS. UNAIDS Data; 2019; pp 1–476.
(116) Rodger, A.; Bruun, T.; Cambiano, V.; Vernazza, P.; Estrada, V.; Lunzen, J. V.; Collins, S.; Geretti, A. M.; Phillips, A. 153LB HIV Transmission Risk Through Condomless Sex If HIV+ Partner On Suppressive ART: PARTNER Study. 1.
(117) Antiretroviral Therapy Cohort Collaboration. Survival of HIV-Positive Patients Starting Antiretroviral Therapy between 1996 and 2013: A Collaborative Analysis of Cohort Studies. *Lancet HIV* **2017**, *4* (8), e349–e356. https://doi.org/10/gkcp48.

(118) Baeten, J. M.; Donnell, D.; Ndase, P. Antiretroviral Prophylaxis for HIV Prevention in Heterosexual Men and Women. *N. Engl. J. Med.* **2012**, *367* (5). https://doi.org/10.1056/NEJMoa1108524.
(119) Donnell, D.; Baeten, J. M.; Bumpus, N. N.; Brantley, J.; Bangsberg, D. R.; Haberer, J. E.; Mujugira, A.; Mugo, N.; Ndase, P.; Hendrix, C.; Celum, C. HIV Protective Efficacy and Correlates of Tenofovir Blood Concentrations in a Clinical Trial of PrEP for HIV Prevention. *J. Acquir. Immune Defic. Syndr. 1999* **2014**, *66* (3), 340–348. https://doi.org/10.1097/QAI.0000000000000172.
(120) Eisinger, R. W.; Dieffenbach, C. W.; Fauci, A. S. HIV Viral Load and Transmissibility of HIV Infection: Undetectable Equals Untransmittable. *JAMA* **2019**, *321* (5), 451–452. https://doi.org/10/gjps4t.
(121) Shroufi, A.; Van Cutsem, G.; Cambiano, V.; Bansi-Matharu, L.; Duncan, K.; Murphy, R. A.; Maman, D.; Phillips, A. Simplifying Switch to Second-Line Antiretroviral Therapy in Sub Saharan Africa: Predicted Effect of Using a Single Viral Load to Define Efavirenz-Based First-Line Failure. *AIDS Lond. Engl.* **2019**, *33* (10), 1635–1644. https://doi.org/10/gg9djg.
(122) Usdin, M.; Guillerm, M.; Calmy, A. Patient Needs and Point-of-Care Requirements for HIV Load Testing in Resource-Limited Settings. *J. Infect. Dis.* **2010**, *201* (Supplement_1), S73–S77. https://doi.org/10.1086/650384.
(123) Fiebig, E. W.; Wright, D. J.; Rawal, B. D.; Garrett, P. E.; Schumacher, R. T.; Peddada, L.; Heldebrant, C.; Smith, R.; Conrad, A.; Kleinman, S. H.; Busch, M. P. Dynamics of HIV Viremia and Antibody Seroconversion in Plasma Donors: Implications for Diagnosis and Staging of Primary HIV Infection. *AIDS* **2003**, *17* (13), 1871–1879. https://doi.org/10/crxkbc.
(124) World Health Organization. *HIV Molecular Diagnostics Toolkit to Improve Access to Viral Load Testing and Infant Diagnosis*, 3rd ed.; World Health Organization: Geneva, 2020.
(125) Chin, C. D.; Laksanasopin, T.; Cheung, Y. K.; Steinmiller, D.; Linder, V.; Parsa, H.; Wang, J.; Moore, H.; Rouse, R.; Umviligihozo, G.; Karita, E.; Mwambarangwe, L.; Braunstein, S. L.; van de Wijgert, J.; Sahabo, R.; Justman, J. E.; El-Sadr, W.; Sia, S. K. Microfluidics-Based Diagnostics of Infectious Diseases in the Developing World. *Nat. Med.* **2011**, *17* (8), 1015–1019. https://doi.org/10.1038/nm.2408.
(126) Pavie, J.; Rachline, A.; Loze, B.; Niedbalski, L.; Delaugerre, C.; Laforgerie, E.; Plantier, J.-C.; Rozenbaum, W.; Chevret, S.; Molina, J.-M.; Simon, F. Sensitivity of Five Rapid HIV Tests on Oral Fluid or Finger-Stick Whole Blood: A Real-Time Comparison in a Healthcare Setting. *PLoS ONE* **2010**, *5* (7), e11581. https://doi.org/10.1371/journal.pone.0011581.
(127) Kran, A.-M. B.; Jonassen, T. Ø.; Sannes, M.; Jakobsen, K.; Lind, A.; Mæland, A.; Holberg-Petersen, M. Overestimation of Human Immunodeficiency Virus Type 1 Load Caused by the Presence of Cells in Plasma from Plasma Preparation Tubes. *J. Clin. Microbiol.* **2009**, *47* (7), 2170–2174. https://doi.org/10.1128/JCM.00519-09.
(128) Monleau, M.; Montavon, C.; Laurent, C.; Segondy, M.; Montes, B.; Delaporte, E.; Boillot, F.; Peeters, M. Evaluation of Different RNA Extraction Methods and Storage Conditions of Dried Plasma or Blood Spots for Human Immunodeficiency Virus Type 1 RNA Quantification and PCR Amplification for Drug Resistance Testing. *J. Clin. Microbiol.* **2009**, *47* (4), 1107–1118. https://doi.org/10.1128/JCM.02255-08.
(129) Bender, A. T.; Borysiak, M. D.; Levenson, A. M.; Lillis, L.; Boyle, D. S.; Posner, J. D. Semiquantitative Nucleic Acid Test with Simultaneous Isotachophoretic Extraction and Amplification. *Anal. Chem.* **2018**, *90* (12), 7221–7229. https://doi.org/10/gdstm8.
(130) Liu, C.; Mauk, M.; Gross, R.; Bushman, F. D.; Edelstein, P. H.; Collman, R. G.; Bau, H. H. Membrane-Based, Sedimentation-Assisted Plasma Separator for Point-of-Care Applications. *Anal. Chem.* **2013**, *85* (21), 10463–10470. https://doi.org/10.1021/ac402459h.
(131) Hin, S.; Loskyll, M.; Klein, V.; Keller, M.; Strohmeier, O.; von Stetten, F.; Zengerle, R.; Mitsakakis, K. Membrane-Based Sample Inlet for Centrifugal Microfluidic Cartridges. *Microelectron. Eng.* **2018**, *187–188*, 78–83. https://doi.org/10.1016/j.mee.2017.12.006.

(132) Drain, P. K.; Dorward, J.; Bender, A.; Lillis, L.; Marinucci, F.; Sacks, J.; Bershteyn, A.; Boyle, D. S.; Posner, J. D.; Garrett, N. Point-of-Care HIV Viral Load Testing: An Essential Tool for a Sustainable Global HIV/AIDS Response. *Clin. Microbiol. Rev.* **2019**, *32* (3), e00097-18. https://doi.org/10.1128/CMR.00097-18.
(133) Singh, R. P. A Solvent-Free, Rapid and Simple Virus RNA-Release Method for Potato Leafroll Virus Detection in Aphids and Plants by Reverse Transcription Polymerase Chain Reaction. *J. Virol. Methods* **1999**, *83* (1–2), 27–33.
(134) Singh, R. P.; Dilworth, A. D.; Singh, M.; McLaren, D. L. Evaluation of a Simple Membrane-Based Nucleic Acid Preparation Protocol for RT-PCR Detection of Potato Viruses from Aphid and Plant Tissues. *J. Virol. Methods* **2004**, *121* (2), 163–170. https://doi.org/10.1016/j.jviromet.2004.06.012.
(135) Puren, A.; Gerlach, J. L.; Weigl, B. H.; Kelso, D. M.; Domingo, G. J. Laboratory Operations, Specimen Processing, and Handling for Viral Load Testing and Surveillance. *J. Infect. Dis.* **2010**, *201* (Supplement_1), S27–S36. https://doi.org/10.1086/650390.
(136) Byrnes, S. A.; Bishop, J. D.; Lafleur, L.; Buser, J. R.; Lutz, B.; Yager, P. One-Step Purification and Concentration of DNA in Porous Membranes for Point-of-Care Applications. *Lab Chip* **2015**, *15* (12), 2647–2659. https://doi.org/10.1039/C5LC00317B.
(137) Persat, A.; Marshall, L. A.; Santiago, J. G. Purification of Nucleic Acids from Whole Blood Using Isotachophoresis. *Anal. Chem.* **2009**, *81* (22), 9507–9511. https://doi.org/10.1021/ac901965v.
(138) Casavant, B. P.; Guckenberger, D. J.; Beebe, D. J.; Berry, S. M. Efficient Sample Preparation from Complex Biological Samples Using a Sliding Lid for Immobilized Droplet Extractions. *Anal. Chem.* **2014**, *86* (13), 6355–6362. https://doi.org/10.1021/ac500574t.
(139) Luft, L. M.; Gill, M. J.; Church, D. L. HIV-1 Viral Diversity and Its Implications for Viral Load Testing: Review of Current Platforms. *Int. J. Infect. Dis.* **2011**, *15* (10), e661–e670. https://doi.org/10.1016/j.ijid.2011.05.013.
(140) Curtis, K. A.; Rudolph, D. L.; Nejad, I.; Singleton, J.; Beddoe, A.; Weigl, B.; LaBarre, P.; Owen, S. M. Isothermal Amplification Using a Chemical Heating Device for Point-of-Care Detection of HIV-1. *PLoS ONE* **2012**, *7* (2), e31432. https://doi.org/10.1371/journal.pone.0031432.
(141) Ocwieja, K. E.; Sherrill-Mix, S.; Liu, C.; Song, J.; Bau, H.; Bushman, F. D. A Reverse Transcription Loop-Mediated Isothermal Amplification Assay Optimized to Detect Multiple HIV Subtypes. *PLOS ONE* **2015**, *10* (2), e0117852. https://doi.org/10.1371/journal.pone.0117852.
(142) Tang, W.; Chow, W. H. A.; Li, Y.; Kong, H.; Tang, Y.; Lemieux, B. Nucleic Acid Assay System for Tier II Laboratories and Moderately Complex Clinics to Detect HIV in Low-Resource Settings. *J. Infect. Dis.* **2010**, *201* (s1), S46–S51. https://doi.org/10.1086/650388.
(143) Gous, N.; Scott, L.; Berrie, L.; Stevens, W. Options to Expand HIV Viral Load Testing in South Africa: Evaluation of the GeneXpert® HIV-1 Viral Load Assay. *PloS One* **2016**, *11* (12), e0168244. https://doi.org/10.1371/journal.pone.0168244.
(144) Ndlovu, Z.; Fajardo, E.; Mbofana, E.; Maparo, T.; Garone, D.; Metcalf, C.; Bygrave, H.; Kao, K.; Zinyowera, S. Multidisease Testing for HIV and TB Using the GeneXpert Platform: A Feasibility Study in Rural Zimbabwe. *PLOS ONE* **2018**, *13* (3), e0193577. https://doi.org/10.1371/journal.pone.0193577.
(145) Meggi, B.; Bollinger, T.; Zitha, A.; Mudenyanga, C.; Vubil, A.; Mutsaka, D.; Nhachigule, C.; Mabunda, N.; Loquiha, O.; Kroidl, A.; Jani, I. V. Performance of a True Point-of-Care Assay for HIV-1/2 Viral Load Measurement at Antenatal and Postpartum Services. *JAIDS J. Acquir. Immune Defic. Syndr.* **2021**, *87* (1), 693. https://doi.org/10.1097/QAI.0000000000002621.
(146) Mukherjee, S.; Cohn, J.; Ciaranello, A. L.; Sacks, E.; Adetunji, O.; Chadambuka, A.; Mafaune, H.; Makayi, M.; McCann, N.; Turunga, E. Estimating the Cost of Point-of-Care Early Infant Diagnosis in a Program Setting: A Case Study Using Abbott m-PIMA and Cepheid GeneXpert IV in Zimbabwe. *JAIDS J. Acquir. Immune Defic. Syndr.* **2020**, *84*, S63. https://doi.org/10.1097/QAI.0000000000002371.
(147) Phillips, N. The Coronavirus Is Here to Stay — Here's What That Means. *Nature* **2021**, *590* (7846), 382–384. https://doi.org/10.1038/d41586-021-00396-2.

(148) Behrmann, O.; Bachmann, I.; Spiegel, M.; Schramm, M.; Abd El Wahed, A.; Dobler, G.; Dame, G.; Hufert, F. T. Rapid Detection of SARS-CoV-2 by Low Volume Real-Time Single Tube Reverse Transcription Recombinase Polymerase Amplification Using an Exo Probe with an Internally Linked Quencher (Exo-IQ). *Clin. Chem.* **2020**, *66* (8), 1047–1054. https://doi.org/10/ggv2cw.
(149) Lau, Y. L.; Ismail, I. binti; Mustapa, N. I. binti; Lai, M. Y.; Soh, T. S. T.; Hassan, A. H.; Peariasamy, K. M.; Lee, Y. L.; Kahar, M. K. B. A.; Chong, J.; Goh, P. P. Development of a Reverse Transcription Recombinase Polymerase Amplification Assay for Rapid and Direct Visual Detection of Severe Acute Respiratory Syndrome Coronavirus 2 (SARS-CoV-2). *PLOS ONE* **2021**, *16* (1), e0245164. https://doi.org/10.1371/journal.pone.0245164.
(150) Qian, J.; Boswell, S. A.; Chidley, C.; Lu, Z.; Pettit, M. E.; Gaudio, B. L.; Fajnzylber, J. M.; Ingram, R. T.; Ward, R. H.; Li, J. Z.; Springer, M. *An Enhanced Isothermal Amplification Assay for Viral Detection*; preprint; Molecular Biology, 2020. https://doi.org/10.1101/2020.05.28.118059.
(151) Liu, D.; Shen, H.; Zhang, Y.; Shen, D.; Zhu, M.; Song, Y.; Zhu, Z.; Yang, C. A Microfluidic-Integrated Lateral Flow Recombinase Polymerase Amplification (MI-IF-RPA) Assay for Rapid COVID-19 Detection. *Lab. Chip* **2021**, *21* (10), 2019–2026. https://doi.org/10.1039/D0LC01222J.
(152) Xue, G.; Li, S.; Zhang, W.; Du, B.; Cui, J.; Yan, C.; Huang, L.; Chen, L.; Zhao, L.; Sun, Y.; Li, N.; Zhao, H.; Feng, Y.; Wang, Z.; Liu, S.; Zhang, Q.; Xie, X.; Liu, D.; Yao, H.; Yuan, J. Reverse-Transcription Recombinase-Aided Amplification Assay for Rapid Detection of the 2019 Novel Coronavirus (SARS-CoV-2). *Anal. Chem.* **2020**, *92* (14), 9699–9705. https://doi.org/10.1021/acs.analchem.0c01032.
(153) Farrera-Soler, L.; Gonse, A.; Kim, K. T.; Barluenga, S.; Winssinger, N. Combining Recombinase Polymerase Amplification and DNA-Templated Reaction for SARS-CoV-2 Sensing with Dual Fluorescence and Lateral Flow Assay Output. *Biopolymers* **2022**, *113* (4), e23485. https://doi.org/10.1002/bip.23485.
(154) Meng, X.; Zou, S.; Li, D.; He, J.; Fang, L.; Wang, H.; Yan, X.; Duan, D.; Gao, L. Nanozyme-Strip for Rapid and Ultrasensitive Nucleic Acid Detection of SARS-CoV-2. *Biosens. Bioelectron.* **2022**, *217*, 114739. https://doi.org/10.1016/j.bios.2022.114739.
(155) Cherkaoui, D.; Huang, D.; Miller, B. S.; Turbé, V.; McKendry, R. A. Harnessing Recombinase Polymerase Amplification for Rapid Multi-Gene Detection of SARS-CoV-2 in Resource-Limited Settings. *Biosens. Bioelectron.* **2021**, *189*, 113328. https://doi.org/10/gmfjb6.
(156) Shelite, T. R.; Uscanga-Palomeque, A. C.; Castellanos-Gonzalez, A.; Melby, P. C.; Travi, B. L. Isothermal Recombinase Polymerase Amplification-Lateral Flow Detection of SARS-CoV-2, the Etiological Agent of COVID-19. *J. Virol. Methods* **2021**, *296*, 114227. https://doi.org/10.1016/j.jviromet.2021.114227.
(157) Xiong, E.; Jiang, L.; Tian, T.; Hu, M.; Yue, H.; Huang, M.; Lin, W.; Jiang, Y.; Zhu, D.; Zhou, X. Simultaneous Dual-Gene Diagnosis of SARS-CoV-2 Based on CRISPR/Cas9-Mediated Lateral Flow Assay. *Angew. Chem. Int. Ed.* **2021**, *60* (10), 5307–5315. https://doi.org/10.1002/anie.202014506.
(158) Su, G.; Zhu, M.; Li, D.; Xu, M.; Zhu, Y.; Zhang, Y.; Zhu, H.; Li, F.; Yu, Y. Multiplexed Lateral Flow Assay Integrated with Orthogonal CRISPR-Cas System for SARS-CoV-2 Detection. *Sens. Actuators B Chem.* **2022**, *371*, 132537. https://doi.org/10.1016/j.snb.2022.132537.
(159) Sun, Y.; Qin, P.; He, J.; Li, W.; Shi, Y.; Xu, J.; Wu, Q.; Chen, Q.; Li, W.; Wang, X.; Liu, G.; Chen, W. Rapid and Simultaneous Visual Screening of SARS-CoV-2 and Influenza Virufses with Customized Isothermal Amplification Integrated Lateral Flow Strip. *Biosens. Bioelectron.* **2022**, *197*, 113771. https://doi.org/10.1016/j.bios.2021.113771.
(160) Dreier, J.; Störmer, M.; Kleesiek, K. Use of Bacteriophage MS2 as an Internal Control in Viral Reverse Transcription-PCR Assays. *J. Clin. Microbiol.* **2005**, *43* (9), 4551–4557. https://doi.org/10.1128/JCM.43.9.4551-4557.2005.
(161) Higgins, M.; Ravenhall, M.; Ward, D.; Phelan, J.; Ibrahim, A.; Forrest, M. S.; Clark, T. G.; Campino, S. PrimedRPA: Primer Design for Recombinase Polymerase Amplification Assays. *Bioinformatics* **2019**, *35* (4), 682–684. https://doi.org/10.1093/bioinformatics/bty701.

(162) Bender, A. T.; Sullivan, B. P.; Zhang, J. Y.; Juergens, D. C.; Lillis, L.; Boyle, D. S.; Posner, J. D. HIV Detection from Human Serum with Paper-Based Isotachophoretic RNA Extraction and Reverse Transcription Recombinase Polymerase Amplification. *The Analyst* **2021**, 10.1039.D0AN02483J. https://doi.org/10/gjvv5z.
(163) Piepenburg, O.; Williams, C. H.; Stemple, D. L.; Armes, N. A. DNA Detection Using Recombination Proteins. *PLOS Biol.* **2006**, *4* (7), e204. https://doi.org/10.1371/journal.pbio.0040204.
(164) Rohrman, B. A.; Richards-Kortum, R. R. A Paper and Plastic Device for Performing Recombinase Polymerase Amplification of HIV DNA. *Lab. Chip* **2012**, *12* (17), 3082. https://doi.org/10.1039/c2lc40423k.
(165) Cordray, M. S.; Richards-Kortum, R. R. A Paper and Plastic Device for the Combined Isothermal Amplification and Lateral Flow Detection of Plasmodium DNA. *Malar. J.* **2015**, *14* (1), 472. https://doi.org/10.1186/s12936-015-0995-6.
(166) Myhrvold, C.; Freije, C. A.; Gootenberg, J. S.; Abudayyeh, O. O.; Metsky, H. C.; Durbin, A. F.; Kellner, M. J.; Tan, A. L.; Paul, L. M.; Parham, L. A.; Garcia, K. F.; Barnes, K. G.; Chak, B.; Mondini, A.; Nogueira, M. L.; Isern, S.; Michael, S. F.; Lorenzana, I.; Yozwiak, N. L.; MacInnis, B. L.; Bosch, I.; Gehrke, L.; Zhang, F.; Sabeti, P. C. Field-Deployable Viral Diagnostics Using CRISPR-Cas13. *Science* **2018**, *360* (6387), 444–448. https://doi.org/10.1126/science.aas8836.
(167) Ruano, G.; Pagliaro, E. M.; Schwartz, T. R.; Lamy, K.; Messina, D.; Gaensslen, R. E.; Lee, H. C. Heat-Soaked PCR: An Efficient Method for DNA Amplification with Applications to Forensic Analysis. *BioTechniques* **1992**, *13* (2), 266–274.
(168) Wang, R.; Zhang, F.; Wang, L.; Qian, W.; Qian, C.; Wu, J.; Ying, Y. Instant, Visual, and Instrument-Free Method for On-Site Screening of GTS 40-3-2 Soybean Based on Body-Heat Triggered Recombinase Polymerase Amplification. *Anal. Chem.* **2017**, *89* (8), 4413–4418. https://doi.org/10.1021/acs.analchem.7b00964.
(169) Crannell, Z. A.; Rohrman, B.; Richards-Kortum, R. Equipment-Free Incubation of Recombinase Polymerase Amplification Reactions Using Body Heat. *PLOS ONE* **2014**, *9* (11), e112146. https://doi.org/10.1371/journal.pone.0112146.
(170) *COVID-19 Target product profiles for priority diagnostics to support response to the COVID-19 pandemic v.1.0*. https://www.who.int/publications/m/item/covid-19-target-product-profiles-for-priority-diagnostics-to-support-response-to-the-covid-19-pandemic-v.0.1 (accessed 2023-02-28).
(171) Lillis, L.; Siverson, J.; Lee, A.; Cantera, J.; Parker, M.; Piepenburg, O.; Lehman, D. A.; Boyle, D. S. Factors Influencing Recombinase Polymerase Amplification (RPA) Assay Outcomes at Point of Care. *Mol. Cell. Probes* **2016**, *30* (2), 74–78. https://doi.org/10.1016/j.mcp.2016.01.009.
(172) UNAIDS. *IN DANGER: UNAIDS Global AIDS Update 2022.*; Geneva: Joint United Nations Programme on HIV/AIDS, 2022.
(173) Saag, M. S.; Benson, C. A.; Gandhi, R. T. Antiretroviral Drugs for Treatment and Prevention of HIV Infection in Adults: 2018 Recommendations of the International Antiviral Society–USA Panel. *JAMA* **2018**, *320* (4). https://doi.org/10.1001/jama.2018.8431.
(174) Saag, M. S.; Holodniy, M.; Kuritzkes, D. R.; O'Brien, W. A.; Coombs, R.; Poscher, M. E.; Jacobsen, D. M.; Shaw, G. M.; Richman, D. D.; Volberding, P. A. HIV Viral Load Markers in Clinical Practice. *Nat. Med.* **1996**, *2* (6), 625–629. https://doi.org/10.1038/nm0696-625.
(175) Drain, P. K.; Dorward, J.; Violette, L. R. Point-of-Care HIV Viral Load Testing Combined with Task Shifting to Improve Treatment Outcomes (STREAM): Findings from an Open-Label, Non-Inferiority, Randomised Controlled Trial. *Lancet HIV* **2020**, *7* (4). https://doi.org/10.1016/S2352-3018(19)30402-3.
(176) World Health Organization. Guidelines: Updated Recommendations on HIV Prevention, Infant Diagnosis, Antiretroviral Initiation and Monitoring. **2021**.
(177) Ryom, L.; De Miguel, R.; Cotter, A. G.; Podlekareva, D.; Beguelin, C.; Waalewijn, H.; Arribas, J. R.; Mallon, P. W. G.; Marzolini, C.; Kirk, O.; Bamford, A.; Rauch, A.; Molina, J. M.; Kowalska, J. D.; Guaraldi, G.; Winston, A.; Boesecke, C.; Cinque, P.; Welch, S.; Collins, S.; Behrens, G. M. N.;

the EACS Governing Board. Major Revision Version 11.0 of the European AIDS Clinical Society Guidelines 2021. *HIV Med.* **2022**, *23* (8), 849–858. https://doi.org/10.1111/hiv.13268.
(178) Panel on Antiretroviral Guidelines for Adults and Adolescents. *Guidelines for the Use of Antiretroviral Agents in Adults and Adolescents with HIV*; Department of Health and Human Services.
(179) Mellors, J. W.; Rinaldo, C. R.; Gupta, P.; White, R. M.; Todd, J. A.; Kingsley, L. A. Prognosis in HIV-1 Infection Predicted by the Quantity of Virus in Plasma. *Science* **1996**, *272* (5265), 1167–1170. https://doi.org/10.1126/science.272.5265.1167.
(180) *Statistics Overview | Statistics Center | HIV/AIDS | CDC*. https://www.cdc.gov/hiv/statistics/overview/index.html (accessed 2019-10-23).
(181) Attia, S.; Egger, M.; Müller, M.; Zwahlen, M.; Low, N. Sexual Transmission of HIV According to Viral Load and Antiretroviral Therapy: Systematic Review and Meta-Analysis: *AIDS* **2009**, *23* (11), 1397–1404. https://doi.org/10.1097/QAD.0b013e32832b7dca.
(182) LeMessurier, J.; Traversy, G.; Varsaneux, O.; Weekes, M.; Avey, M. T.; Niragira, O.; Gervais, R.; Guyatt, G.; Rodin, R. Risk of Sexual Transmission of Human Immunodeficiency Virus with Antiretroviral Therapy, Suppressed Viral Load and Condom Use: A Systematic Review. *CMAJ Can. Med. Assoc. J. J. Assoc. Medicale Can.* **2018**, *190* (46), E1350–E1360. https://doi.org/10/gfrpmv.
(183) Antiretroviral Therapy Cohort Collaboration. Survival of HIV-Positive Patients Starting Antiretroviral Therapy between 1996 and 2013: A Collaborative Analysis of Cohort Studies. *Lancet HIV* **2017**, *4* (8), e349–e356. https://doi.org/10.1016/S2352-3018(17)30066-8.
(184) Hubbard, R. A. Human Papillomavirus Testing Methods. *Arch. Pathol. Lab. Med.* **2003**, *127* (8), 940–945. https://doi.org/10.5858/2003-127-940-HPTM.
(185) McHugh, M. P.; Wu, A. H. B.; Chevaliez, S.; Pawlotsky, J. M.; Hallin, M.; Templeton, K. E. Multicenter Evaluation of the Cepheid Xpert Hepatitis C Virus Viral Load Assay. *J. Clin. Microbiol.* **2017**, *55* (5), 1550–1556. https://doi.org/10.1128/jcm.02460-16.
(186) Walt, S. van der; Schönberger, J. L.; Nunez-Iglesias, J.; Boulogne, F.; Warner, J. D.; Yager, N.; Gouillart, E.; Yu, T. Scikit-Image: Image Processing in Python. *PeerJ* **2014**, *2*, e453. https://doi.org/10.7717/peerj.453.
(187) Piepenburg, O.; Armes, N. A. Recombinase Polymerase Amplification Reagents and Kits. WO2010141940A1, December 9, 2010. https://patents.google.com/patent/WO2010141940A1/en (accessed 2025-03-25).
(188) Culbertson, C. T.; Jacobson, S. C.; Michael Ramsey, J. Diffusion Coefficient Measurements in Microfluidic Devices. *Talanta* **2002**, *56* (2), 365–373. https://doi.org/10.1016/S0039-9140(01)00602-6.
(189) Bechekh, K.; and Ghaouar, N. Rheological Properties of Polyethylene Glycol (PEG 35000): An Interpretation of a Negative Intrinsic Viscosity and a High Huggins Coefficient Value. *J. Macromol. Sci. Part B* **2014**, *53* (3), 391–397. https://doi.org/10.1080/00222348.2013.810105.
(190) Annunziata, O.; Asherie, N.; Lomakin, A.; Pande, J.; Ogun, O.; Benedek, G. B. Effect of Polyethylene Glycol on the Liquid–Liquid Phase Transition in Aqueous Protein Solutions. *Proc. Natl. Acad. Sci.* **2002**, *99* (22), 14165–14170. https://doi.org/10.1073/pnas.212507199.
(191) Fahie-Wilson, M.; Halsall, D. Polyethylene Glycol Precipitation: Proceed with Care. *Ann. Clin. Biochem.* **2008**, *45* (3), 233–235. https://doi.org/10.1258/acb.2008.007262.
(192) Haire, R. N.; Tisel, W. A.; White, J. G.; Rosenberg, A. On the Precipitation of Proteins by Polymers: The Hemoglobin—Polyethylene Glycol System. *Biopolymers* **1984**, *23* (12), 2761–2779. https://doi.org/10.1002/bip.360231206.
(193) Khavidaki, H. D.; Asadi, Z.; Salabat, A. Effect of Salt Mixtures on Aqueous Two-Phase System Composed of PEG 35000: Experiment and Correlation. *J. Solut. Chem.* **2024**, *53* (10), 1409–1418. https://doi.org/10.1007/s10953-024-01381-9.
(194) Li, Y.; Li, L.; Fan, X.; Zou, Y.; Zhang, Y.; Wang, Q.; Sun, C.; Pan, S.; Wu, X.; Wang, Z. Development of Real-Time Reverse Transcription Recombinase Polymerase Amplification (RPA)

for Rapid Detection of Peste Des Petits Ruminants Virus in Clinical Samples and Its Comparison with Real-Time PCR Test. *Sci. Rep.* **2018**, *8* (1), 17760. https://doi.org/10.1038/s41598-018-35636-5.

(195) Amer, H. M.; Abd El Wahed, A.; Shalaby, M. A.; Almajhdi, F. N.; Hufert, F. T.; Weidmann, M. A New Approach for Diagnosis of Bovine Coronavirus Using a Reverse Transcription Recombinase Polymerase Amplification Assay. *J. Virol. Methods* **2013**, *193* (2), 337–340. https://doi.org/10.1016/j.jviromet.2013.06.027.

(196) Chauhan, R.; Ghanshala, K. K.; Joshi, R. C. Convolutional Neural Network (CNN) for Image Detection and Recognition. In *2018 First International Conference on Secure Cyber Computing and Communication (ICSCCC)*; IEEE: Jalandhar, India, 2018; pp 278–282. https://doi.org/10.1109/ICSCCC.2018.8703316.

(197) Rutherford, J. W.; Larson, T. V.; Gould, T.; Seto, E.; Novosselov, I. V.; Posner, J. D. Source Apportionment of Environmental Combustion Sources Using Excitation Emission Matrix Fluorescence Spectroscopy and Machine Learning. *Atmos. Environ.* **2021**, *259*, 118501. https://doi.org/10/gmgbbw.

(198) Siegler, T. D.; Dunlap-Shohl, W. A.; Meng, Y.; Yang, Y.; Kau, W. F.; Sunkari, P. P.; Tsai, C. E.; Armstrong, Z. J.; Chen, Y.-C.; Beck, D. A. C.; Meilă, M.; Hillhouse, H. W. Water-Accelerated Photooxidation of $CH_3NH_3PbI_3$ Perovskite. *J. Am. Chem. Soc.* **2022**, *144* (12), 5552–5561. https://doi.org/10.1021/jacs.2c00391.

(199) Weng, W.; Zhu, X. INet: Convolutional Networks for Biomedical Image Segmentation. *IEEE Access* **2021**, *9*, 16591–16603. https://doi.org/10.1109/ACCESS.2021.3053408.

(200) Akiba, T.; Sano, S.; Yanase, T.; Ohta, T.; Koyama, M. Optuna: A Next-Generation Hyperparameter Optimization Framework. arXiv July 25, 2019. https://doi.org/10.48550/arXiv.1907.10902.

(201) Seok, Y.; Joung, H.-A.; Byun, J.-Y.; Jeon, H.-S.; Shin, S. J.; Kim, S.; Shin, Y.-B.; Han, H. S.; Kim, M.-G. A Paper-Based Device for Performing Loop-Mediated Isothermal Amplification with Real-Time Simultaneous Detection of Multiple DNA Targets. *Theranostics* **2017**, *7* (8), 2220–2230. https://doi.org/10.7150/thno.18675.

(202) Ahn, H.; Batule, B. S.; Seok, Y.; Kim, M.-G. Single-Step Recombinase Polymerase Amplification Assay Based on a Paper Chip for Simultaneous Detection of Multiple Foodborne Pathogens. *Anal. Chem.* **2018**, *90* (17), 10211–10216. https://doi.org/10/gd38fq.

(203) Linnes, J. C.; Rodriguez, N. M.; Liu, L.; Klapperich, C. M. Polyethersulfone Improves Isothermal Nucleic Acid Amplification Compared to Current Paper-Based Diagnostics. *Biomed. Microdevices* **2016**, *18* (2). https://doi.org/10.1007/s10544-016-0057-z.